

Development of the physical snowpack model SMAP:  
Application to seasonal snowpack in Japan and the Greenland ice sheet

(積雪変質モデル SMAP の開発 :  
日本の季節積雪とグリーンランド氷床への適用)

NIWANO, Masashi

(庭野 匡思)

A dissertation for the degree of  
Doctor of Science  
submitted to  
Graduate School of Environmental Studies,  
Nagoya University  
(名古屋大学大学院環境学研究科 博士 (理学))

2016

## Acknowledgements

First of all, I sincerely appreciate Prof. Kouichi Nishimura, Nagoya University for kindly giving me a chance to write and submit a doctor thesis. I also thank him for his continuous guidance as well as very helpful discussions and suggestions during my preparation of this thesis.

I would like to express my heartfelt thanks to Prof. Teruo Aoki, Okayama University (the former head of the 6<sup>th</sup> Research Laboratory, Climate Research Department, Meteorological Research Institute) for his continuous guidance, support, and encouragement. I have always been impressed by his outstanding enthusiasm to scientific activities. Also, I would like to thank him for giving me a chance to join field campaigns in the Greenland ice sheet for four times since 2012. These quite valuable experiences with him are my life treasure.

I extend my sincere gratitude to Dr. Koji Fujita and Prof. Tetsuya Hiyama for taking the time to evaluate this work. Thanks to a warm atmosphere, which they kindly created during my examination, I could relax the tension throughout my presentation.

Finally, I appreciate my colleagues: Mr. Katsuyuki Kuchiki (Meteorological Research Institute; MRI), Dr. Tomonori Tanikawa (MRI), Dr. Masahiro Hosaka (MRI), Dr. Yuji Kodama (National Institute of Polar Research; NIPR), Dr. Satoru Yamaguchi (Snow and Ice Research Center, National Research Institute for Earth Science and Disaster Prevention; NIED), Dr. Hiroki Motoyoshi (NIED), Dr. Yuki Yoshi Iwata (National Institute for Rural Engineering), Dr. Sumito Matoba (Institute of Low Temperature Science, Hokkaido University), Prof. Hideaki Motoyama (NIPR), Mr. Tetsuhide Yamasaki (polar explorer), Prof. Akihiro Hachikubo (Kitami Institute of Technology), Dr. Masahiro Hori (Japan Aerospace Exploration Agency), Dr. Akihiro Hashimoto (MRI), and Dr. Martin Schneebeli (WSL Institute for Snow and Avalanche Research SLF) for their kind support to my study.

## Abstract

In the present study, a multi-layered physical snowpack model called SMAP (Snow Metamorphism and Albedo Process) was developed, and applied to climate studies focusing on the snow-atmosphere interaction in Japan and polar region (Greenland). In Chapter 1 of this thesis, scientific background of this study is reviewed comprehensively.

In Chapter 2, basic version of the SMAP model is introduced. The SMAP model incorporates a state-of-the-art physically based snow albedo model, which calculates snow albedo and solar heating profile in snowpack considering effects of optically equivalent snow grain size and snow impurities explicitly, to simulate realistic physical states of snowpack. The performance of SMAP with meteorological and snow impurities (black carbon and dust) input data measured at Sapporo, Japan during two winters: 2007–2008 and 2008–2009 was evaluated, and it was found that SMAP successfully reproduced all observed variations of physical properties of snowpack for both winters. We have thus confirmed that SMAP is suitable for climate simulations. With the version of SMAP, the effects of snow impurities on snowmelt at Sapporo during the two winters were investigated. We found that snowpack durations at Sapporo were shortened by 19 days during the 2007–2008 winter and by 16 days during the 2008–2009 winter due to radiative forcings caused by snow impurities. The estimated radiative forcings due to snow impurities during the accumulation periods were  $3.7 \text{ W m}^{-2}$  (it corresponds to albedo reduction in 0.05) and  $3.2 \text{ W m}^{-2}$  (albedo reduction in 0.05) for the 2007–2008 and 2008–2009 winters, respectively. While during the ablation periods they were  $25.9 \text{ W m}^{-2}$  (albedo reduction in 0.18) and  $21.0 \text{ W m}^{-2}$  (albedo reduction in 0.17) for each winter, respectively.

In Chapter 3, the SMAP model was updated by incorporating a detailed water movement scheme, realistic snow settlement process and limitation for the Richardson number to ensure minimum turbulent exchanges even under highly stable atmospheric conditions. The evaluation of the updated

version of SMAP was first performed using the data obtained at Sapporo, Japan, during the 2007–2009 winters and the effectiveness of these updates was demonstrated in terms of snow depth and snow surface temperature. However, it was pointed out that the choice of maximum Richardson number should be further examined. To test the reliability of SMAP under different climate conditions, it was applied to Nagaoka, Japan, during the 2011–2012 winter. At Nagaoka, we performed snow-soil-coupled simulations, because ground heat flux was not available during the study period. For this purpose, a soil submodel for SMAP was developed. Consequently, we confirmed that the updated version performed better than the old version in terms of mass balance simulations at Nagaoka too. Although mass balance-related parameters of the snowpack simulated by the updated version agreed well with observations during the accumulation period, the model substantially overestimated snow depth, as well as column-integrated snow water equivalent during the ablation period. By discussing the reasons for these discrepancies, we highlighted that further investigation on snow-melt processes for thick seasonal snowpack is necessary.

In recent years, the terrestrial snow cover has been melt drastically, which results in a decreasing trend of snow cover duration in the cryosphere. In order to understand ongoing rapid changes in physical states of snowpack, we investigated factors controlling snow melt and subsequent runoff from snowpack at Sapporo, Japan during the 2005–2015 winters (December to March) from the standpoint of snow surface energy balance by employing the fully quality-controlled meteorological and snow data, as well as a physical snowpack model SMAP (Chapter 4). The SMAP model was evaluated in terms of column-integrated snow water equivalent, snow density profile, snow surface temperature, and snow temperature profile, and validation results revealed that the model simulated energy and mass balances of snowpack well. During ablation period (March), model-simulated daily-mean meltwater runoff rate was  $7 \text{ kg m}^{-2} \text{ w.e. day}^{-1}$ . The situation when calculated runoff rate was above average was characterized by higher net shortwave radiant flux, sensible heat flux, and

latent heat flux. This condition was caused by increased downward shortwave radiant flux, air temperature, and vapor pressure, as well as decreased albedo and cloud fraction. These suggest that sunny weather condition in the daytime was an ideal condition for enhanced ablation during the study period at Sapporo.

In Chapter 5, we attempted to apply the update version of the SMAP model in polar region. The SEB from 30 June to 14 July 2012 at site SIGMA (Snow Impurity and Glacial Microbe effects on abrupt warming in the Arctic)-A, (78°03'N, 67°38'W; 1490 m a.s.l.) on the northwest Greenland Ice Sheet (GrIS) was investigated by using in situ atmospheric and snow measurements as well as numerical modeling with the SMAP model. At SIGMA-A, remarkable near-surface snowmelt and continuous heavy rainfall (accumulated precipitation between 10 and 14 July was estimated to be 100 mm) were observed after 10 July 2012. Application of the SMAP model to the GrIS snowpack was evaluated based on the snow temperature profile, snow surface temperature, surface snow grain size, and shortwave albedo, all of which the model simulated reasonably well. Above all, the fact that the SMAP model successfully reproduced frequently observed rapid increases in snow albedo under cloudy conditions highlights the advantage of the physically based snow albedo model (PBSAM) incorporated in the SMAP model. Using such data and model, we estimated the SEB at SIGMA-A from 30 June to 14 July 2012. Radiation-related fluxes were obtained from in situ measurements, whereas other fluxes were calculated with the SMAP model. By examining the components of the SEB, we determined that low-level clouds accompanied by a significant temperature increase played an important role in the melt event observed at SIGMA-A. These conditions induced a remarkable surface heating via cloud radiative forcing in the polar region.

Finally, in Chapter 6, scientifically significant outcomes of the present study are summarized, and future outlook regarding studies employing the SMAP model is briefly discussed.

## Table of contents

Acknowledgements .....	i
Abstract.....	ii
1. Introduction .....	1
1.1. Physical characteristics of the snowpack.....	1
1.2. Effects of physical state changes in the terrestrial snowpack.....	3
1.3. Physical snowpack model.....	4
1.4. Objective of this thesis .....	6
2. Development of the physical snowpack model SMAP: Basic formulation, validation, and application to a study on the effects of snow impurities.....	8
2.1. Introduction .....	8
2.2. Model description.....	13
2.2.1. Energy balance of snowpack .....	15
2.2.2. Mass balance of snowpack .....	22
2.2.3. Snow settlement.....	23
2.2.4. Snow metamorphism .....	24
2.2.5. Numerical solution .....	27
2.3. Field measurements at Sapporo.....	28
2.3.1. Meteorological measurements.....	28
2.3.2. Snow pit observations.....	29
2.3.3. Meteorological and snow conditions at Sapporo.....	32
2.4. Model validation with data from Sapporo.....	32
2.4.1. Snow depth, SWE, and snow density .....	33
2.4.2. Snow grain shape.....	38
2.4.3. Snow surface temperature .....	39
2.4.4. Snow grain size.....	41
2.4.5. Broadband albedos .....	44
2.5. Effects of snow impurities on snowmelt at Sapporo .....	46
2.6. Summary and conclusions .....	48
Acknowledgements .....	51
3. Attempts of advanced numerical snow modeling .....	53
3.1. Introduction .....	53
3.2. Materials and methods.....	55
3.2.1. Field measurements .....	55

3.2.1.1.	2007–2009 Winters at Sapporo, Japan .....	55
3.2.1.2.	2011–2012 Winter at Nagaoka, Japan .....	56
3.2.2.	SMAP model overview .....	58
3.2.3.	Model updates .....	59
3.2.3.1.	Water movement in the snowpack .....	59
3.2.3.2.	Snow settlement .....	61
3.2.3.3.	Turbulent heat exchanges under very stable conditions .....	62
3.2.3.4.	Soil submodel .....	63
3.2.4.	Model simulations and evaluation .....	65
3.3.	Results and discussion .....	67
3.3.1.	Sapporo .....	67
3.3.1.1.	Meteorological and snow conditions .....	67
3.3.1.2.	Snow depth .....	68
3.3.1.3.	Snow surface temperature .....	71
3.3.2.	Nagaoka .....	72
3.3.2.1.	Meteorological and snow conditions .....	72
3.3.2.2.	Snow depth, snow water equivalent and snow density .....	74
3.3.2.3.	Soil temperature .....	77
3.3.2.4.	Volumetric water content in the snowpack .....	78
3.3.2.5.	Snow surface temperature .....	78
3.4.	Conclusions .....	80
	Acknowledgements .....	82
4.	Wintertime snow surface energy balance and ablation characteristics at Sapporo, Japan (2005–2015) .....	84
4.1.	Introduction .....	84
4.2.	Data and methods .....	89
4.2.1.	Meteorological measurements .....	89
4.2.2.	Cloud fraction observation .....	94
4.2.3.	Snow pit measurements .....	95
4.2.4.	Numerical simulation with the SMAP model .....	96
4.3.	Results and discussion .....	99
4.3.1.	Model evaluation .....	99
4.3.2.	Snow surface energy balance .....	103
4.3.3.	Modeled meltwater runoff rate .....	104
4.4.	Conclusions .....	107
	Acknowledgements .....	108

5.	Application of the SMAP model to the Greenland ice sheet.....	114
5.1.	Introduction .....	114
5.2.	Field measurements at the SIGMA-A site.....	118
5.2.1.	Meteorological observations .....	119
5.2.2.	Snow pit measurements .....	125
5.3.	Numerical simulation with the SMAP model.....	127
5.3.1.	SMAP model overview.....	127
5.3.2.	Adaption of the SMAP model to the Greenland snowpack.....	129
5.3.3.	Model configuration .....	130
5.4.	Model evaluation using the data at the SIGMA-A site.....	132
5.4.1.	Snow temperature profile .....	134
5.4.2.	Snow surface temperature .....	134
5.4.3.	Surface snow grain size .....	136
5.4.4.	Shortwave albedo .....	137
5.5.	SEB during the IOP at SIGMA-A .....	139
5.6.	Discussion.....	143
5.6.1.	Effects of model settings on the calculated SEB .....	143
5.6.2.	Uncertainties caused by the latent heat flux calculation method.....	144
5.7.	Conclusions .....	149
	Acknowledgements .....	151
6.	Summary and future outlook .....	153
	References .....	155
	Curriculum Vitae .....	178



# 1. Introduction

## 1.1. Physical characteristics of the snowpack

Snow cover forms a unique terrestrial land surface, characterized by a relatively high albedo, a low temperature, high thermal insulating properties, a relatively low surface roughness length, and the ability for phase changes. These characteristics are constantly being modified in response to changes in external forcings such as meteorological conditions.

Snow albedo typically ranges between 0.9 and 0.5 (*Armstrong and Brun, 2008*). Generally, a high albedo is measured for precipitation particles, and this has been shown to decrease with snow age (e.g., *Aoki et al., 2003; 2011*). The snow albedo is governed by both internal and external factors of the snowpack. Important snow internal physical properties that significantly affect the snow albedo are optically equivalent snow grain size and mass concentrations of snow impurities e.g., black carbon (BC) and dust (*Wiscombe and Warren, 1980; Warren and Wiscombe, 1980; Aoki et al., 1999, 2000, 2003*). The near-infrared albedo, in particular, is controlled by optically equivalent snow grain size (*Wiscombe and Warren, 1980*), while the visible albedo strongly depends on mass concentrations of snow impurities (*Warren and Wiscombe, 1980*). Here, the optically equivalent snow grain size is defined as the radius of a sphere that has the same optical hemispherical reflectance property as a real non-spherical snow grain, and its size is generally smaller than a traditional geometric grain (e.g., *Giddings and LaChapelle, 1961; Wiscombe and Warren, 1980; Grenfell and Warren, 1999; Aoki et al., 1999, 2000, 2003, 2007b; Fierz et al., 2009*). The optically equivalent snow grain size is developed through snow metamorphism: equi-temperature metamorphism, temperature gradient metamorphism, and wet snow metamorphism. External physical conditions that control the snow albedo are cloud cover, atmospheric constituents such as aerosols and absorptive gases, and solar illumination conditions (*Wiscombe and Warren, 1980; Aoki et al., 1999*).

As for the temperature of snow cover, it never exceeds 0 °C because snow consists of ice, water, and air. The snow surface temperature is physically governed by the surface energy balance (SEB), which is the sum of the net shortwave radiant flux, the net long-wave radiant flux, the sensible heat flux, the latent heat flux, the heat supply from rainfall, and the subsurface conductive heat flux. The temperature profile in the snowpack is controlled by vertical heat conduction, solar heating in the snowpack (also mainly controlled by profiles of optically equivalent snow grain size and mass concentrations of snow impurities), and latent heat release due to phase changes (positive for the case of refreezing and negative for the case of melting). Vertical heat conduction in the snowpack is controlled by the effective thermal conductivity of snow. According to *Sturm et al.* (1997), effective thermal conductivity of the seasonal snowpack ranges between 0.01 to 1 W m<sup>-1</sup> K<sup>-1</sup>. This relatively low value compared to those for other naturally existing substances (e.g., rocks, liquid water, soil, and ice) makes the snow an effective thermal insulator. The effective thermal conductivity of snow generally increases with snow density, which can reach the density of ice (917 kg m<sup>-3</sup>). This means that the thermal insulating properties are gradually lost as the snow age increases.

The roughness length for momentum over the snowpack typically has values of the order of 10<sup>-4</sup> to 10<sup>-3</sup> m (*Armstrong and Brun*, 2008; *Brock et al.*, 2006). Because of these small values, snow cover is considered as one of the smoothest land surface types on Earth. The roughness length for momentum affects the turbulent heat exchange between the snowpack and the atmosphere (sensible and latent heat fluxes, *Andreas*, 1987). In general, a smaller roughness length induces a smaller turbulent heat flux and a smaller resulting surface melting rate (*Armstrong and Brun*, 2008); however, the estimation of turbulent heat flux magnitudes is not straightforward because these fluxes also depend strongly on the near-surface atmospheric profile. The ability to change phases also affects the turbulent heat and resultant mass exchange. When the latent heat flux is directed towards

the atmosphere, sublimation can occur if the surface consists only of ice and air. On the other hand, the presence of water in the snow surface allows evaporation to the atmosphere.

## **1.2. Effects of physical state changes in the terrestrial snowpack**

Snow cover occupies a mean maximum areal extent of 47 million km<sup>2</sup>, about 98 % of which is located in the Northern Hemisphere, and it is the second largest component of the cryosphere in terms of spatial extent, after seasonally frozen ground (~65 million km<sup>2</sup>) (*Armstrong and Brun*, 2008). In recent years, significant attention has been paid to the physical conditions of the snowpack as a result of rapidly changing climate conditions. At present, there is a consensus that increased surface air temperature in response to increased concentrations of greenhouse gases will be amplified at high latitudes (polar amplification e.g., *Holland and Bitz*, 2003; *Serreze and Francis*, 2006). Because surface air temperature increases can induce a decline in snow cover, this regional warming is amplified dramatically through a mechanism known as snow-albedo feedback (e.g., *Budyko*, 1969; *Sellers*, 1969; *Hall*, 2004; *Qu and Hall*, 2007), wherein the albedo decrease from a snow covered surface to a snow free surface enhances warming. Such amplification is significantly more enhanced in the Northern Hemisphere (*Screen and Simmonds*, 2010) due to the large areal extent of land covered by snow or ice, and the greater amount of sea ice in the Northern Hemisphere compared to the Southern Hemisphere. According to *Brown and Robinson* (2011), the Northern Hemisphere spring snow cover extent has been significantly reduced over the past ~90 years and the rate of decrease has accelerated over the past 40 years as a consequence. These changes affect the ground thermal regime under the snow cover in cold regions (e.g., *Zhang*, 2005; *Iwata et al.*, 2010).

In the Greenland ice sheet (GrIS), the rate of ice loss has accelerated abruptly since 1992. The IPCC AR5 (Fifth Assessment Report of the Intergovernmental Panel on Climate Change, *Vaughan et al.*, 2013) reported that ice loss from the GrIS could be partitioned into approximately similar amounts between surface melt (of snow and ice) and glacier outlet dynamic discharge. However,

recently, several authors have pointed out a relative increase in the importance of surface processes for mass loss from the GrIS in the post-AR5 era. *Enderlin et al.* (2014) demonstrated that the relative contribution of ice discharge to total loss decreased from 58 % before 2005 to 32 % between 2009 and 2012. As such, 84 % of the increase in mass loss after 2009 was due to increased surface runoff. *Andersen et al.* (2015) found that mass loss from the GrIS (mean total mass balance of  $-262 \pm 21$  Gt  $\text{yr}^{-1}$ ) was dominated by the surface mass balance, which accounted for 61 % of the mass loss in basins where partitioning was possible.

### **1.3. Physical snowpack model**

In order to understand abrupt transitions in terrestrial snow physical conditions, performing in-situ measurements from various aspects is absolutely necessary. In addition, theoretical consideration of observed features is also inevitable. A numerical snowpack model can play a role in connecting and complementing observational and theoretical studies. For example, validity of a theory or model deduced from in-situ measurements can be demonstrated using numerical simulations by evaluating whether the calculations can reproduce reality with a sufficiently high accuracy. Once a physical-based accurate numerical snowpack model is developed, it could also be used for future predictions. In this thesis, by physical snowpack model we are referring to physically based numerical model that calculates the temporal evolution of the snowpack. In the following section, numerical models are indicated simply as “models” unless otherwise mentioned.

Many models have been developed that deal with snowpack (*Etchevers et al.*, 2004; *Armstrong and Brun*, 2008), of which nearly half were developed in the USA and the remainder come from more than 13 other countries (*Armstrong and Brun*, 2008). *Boone and Etchevers* (2001) proposed three categories for describing these models in terms of model complexity: (1) relatively simple so-called force-restore models in which the snow is modeled with only one layer, (2) (often multi-layered) physically based models that consider detailed internal snow physical processes (physical

snowpack models), and (3) intermediate-complexity models based on the above mentioned detailed models (category 2), in which some physical processes are simplified and the number of modeled snow layers are restricted, mainly to reduce computational costs. At present, two widely used and well-validated physical snowpack models exist: the Crocus model (*Brun et al.*, 1989, 1992) and the SNOWPACK model (*Bartelt and Lehning*, 2002; *Lehning et al.*, 2002a, 2002b). *Brun et al.* (1992)'s epoch-making modeling approach with the Crocus model succeeded in realistically simulating the temporal evolution of snow grain shape by introducing two parameters: dendricity and sphericity. Dendricity varies from 1 to 0 and describes the original crystal shapes, which remain in the snow layer. Sphericity varies between 0 and 1 and describes the ratio of rounded to angular shapes. The SNOWPACK model follows the same approach of the temporal evolution of snow grain shape using dendricity and sphericity (*Lehning et al.*, 2002a); however, it employs more sophisticated formulations, especially for dry snow metamorphism and the effective thermal conductivity of snow (*Lehning et al.*, 2002a). Furthermore, the SNOWPACK model was the first model that succeeded in simulating the bond and neck sizes of snow grains, which have a vital influence on the mechanical properties of snow (*Lehning et al.*, 2002a).

In Japan, both models have been applied from the beginning of the 2000's. *Hachikubo* (2001) employed the Crocus model to calculate the SEB in a mountainous area of northern Hokkaido from 1994 to 1996, and found that it agreed well with observations. *Yamaguchi et al.* (2004) applied the SNOWPACK model to a wet-snow area in Japan, and found that introducing the compressive viscosity obtained for wet snow in Japan improved the accuracy of model simulations. *Hirashima et al.* (2004) conducted simulations of snowpack evolution at Sapporo, Kitami, and Niseko with the revised version of the SNOWPACK model by *Yamaguchi et al.* (2004), and obtained good agreements regarding snow grain shape. *Nishimura et al.* (2005) studied avalanche warming in Niseko utilizing the SNOWPACK model, and demonstrated the model's significant promise.

*Hirashima et al.* (2008) performed avalanche forecasting with the SNOWPACK model at Tsunan, Niigata during the winter of 2005–2006, where the snow depth exceeded 4 m. They obtained reasonable agreement in terms of the snow internal profile; however, it was found that the equations for the stability index were unsuitable for the study area.

Even today, attempts to improve both models are continuously being made. A summary of the recent updates to the Crocus model can be found in *Vionnet et al.* (2012). Based on this version, *Jacobi et al.* (2010), *Morin et al.* (2003), and *Carmagnola et al.* (2014) developed schemes for calculating the temporal evolution of the specific surface area of snow (SSA), which is a useful variable for describing the physical and chemical properties of snow, as well as a quantitative link to snow metamorphism and the optical properties of snow. Although the Crocus model did not explicitly consider the effects of snow impurities on snow albedo until recently, *Jacobi et al.* (2015) tried to consider such effects by incorporating a description of the radiative transfer inside the snowpack. They performed snow simulations with the new model version in the upper Khumbu Valley, Nepal in the winters of 2009–2012 and demonstrated that it worked as expected; however, albedo and snow durations are still overestimated. As for the SNOWPACK model (which also does not consider effects of snow impurities), attempts to improve descriptions of vertical water movement in the snowpack by taking into account the Richards equation (*Richards*, 1931) (*Hirashima et al.*, 2010; *Wever et al.*, 2014, 2015) have been numerous. This approach would improve estimation of the mass balance of the snowpack, and consequently, the timing and magnitude of runoff from the snowpack.

#### **1.4. Objective of this thesis**

In this study, we develop a physical snowpack model known as the Snow Metamorphism and Albedo Process (SMAP), which explicitly considers the effects of snow impurities on snow albedo. This multi-layered model would fit into category (2) of the classification mentioned above. Using the

model, we investigate snow-atmosphere interactions from various aspects. In Chapter 2, basic formulations of the SMAP model are described, and validation results using the data obtained at Sapporo, Japan during the winters of 2007–2009 are explained. The accuracy of the SMAP model-simulated snow albedo is also highlighted. In addition, investigation of radiative forcing due to snow impurities at Sapporo during the study period is performed through a SMAP model sensitivity study. In Chapter 3, further attempts at state-of-the-art snow modeling are presented, where knowledge regarding snow-atmosphere energy exchange and snow densification, demonstrated by the latest version of the Crocus model (*Brun et al.*, 2011; *Vionnet et al.*, 2012), is taken into account. Furthermore, we try to incorporate the Richards equation (*Richards*, 1931), as performed by the SNOWPACK model (*Hirashima et al.*, 2010; *Wever et al.*, 2014, 2015). Model validations are performed at Sapporo and Nagaoka, Japan. At Sapporo, dry snow grain shapes are often measured during the accumulation period, while melt forms are mainly observed throughout the winter period at Nagaoka. The established version of the SMAP model is employed for analysis of the winter climate conditions at Sapporo from 2005 to 2015 in Chapter 4. Characteristics of the snow SEB and resultant ablation at Sapporo are presented. After careful model evaluation performed in Japan, the SMAP model is applied to the GrIS, where abrupt surface melting and the resulting mass loss are accelerating (Chapter 5). Effectiveness of the model in the GrIS is examined for the 2012 summer record surface melt event (*Nghiem et al.*, 2012; *Tedesco et al.*, 2013; *Hall et al.*, 2013; *Hanna et al.*, 2014; *Bennartz et al.*, 2013), and the dramatic surface melt observed during the same period at the SIGMA-A site (Snow Impurity and Glacial Microbe effects on abrupt warming in the Arctic)-A (*Aoki et al.*, 2014a), northwest GrIS, is also investigated. Finally, in Chapter 6, the main findings of this study are summarized and the future outlook regarding applications of the SMAP model is briefly discussed.

## **2. Development of the physical snowpack model SMAP:**

### **Basic formulation, validation, and application to a study on the effects of snow impurities**

Published in *Journal of Geophysical Research, Earth Surface*, **117**, F03008, doi:10.1029/2011JF002239, 2012, entitled as “**Snow Metamorphism and Albedo Process (SMAP) model for climate studies: Model validation using meteorological and snow impurity data measured at Sapporo, Japan**”.

**M. Niwano<sup>1</sup>, T. Aoki<sup>1</sup>, K. Kuchiki<sup>1</sup>, M. Hosaka<sup>1</sup>, Y. Kodama<sup>2, 3</sup>**

<sup>1</sup> Meteorological Research Institute, Japan Meteorological Agency

<sup>2</sup> Institute of Low Temperature Science, Hokkaido University

<sup>3</sup> Now at National Institute of Polar Research, Tachikawa

#### **2.1. Introduction**

Snow cover affects terrestrial climate system through its high albedo, thermal insulating properties (low thermal conductivity), and the ability to change phase (*Armstrong and Brun*, 2008). The retreat of snow cover induced by global warming causes a positive feedback known as snow albedo feedback (e.g., *Budyko*, 1969; *Sellers*, 1969; *Hall*, 2004; *Qu and Hall*, 2007), wherein the albedo decrease from snow covered surface to snow free surface enhances warming. The feedback process accelerates melting of snow and ice. The low thermal conductivity of snow obstructs energy exchanges between the ground and the atmosphere. The ability of snow to change its phases makes itself to play a role in retarding warming of both the ground and the atmosphere during ablation period because large amount of energy is required to melt ice.

Light-absorbing impurities such as black carbon (BC) and dust in snow and ice have recently been recognized as possible contributors to global warming because they generally reduce snow and ice albedos. *Hansen and Nazarenko* (2004) estimated that BC on snow and ice contributed about one-



quarter of observed global warming during 1880–2000. *Flanner et al.* (2007) showed that BC in snowpack can provoke a disproportionately large springtime climate response because the forcing tends to coincide with the onset of snowmelt and results in the triggering of more rapid snow melting and snow albedo feedback. *Painter et al.* (2007) demonstrated that snow cover duration in a seasonally snow-covered mountain range (San Juan Mountains, Colorado, USA) was shortened by 18 to 35 days during ablation periods in 2005 and 2006 as a result of surface shortwave radiative forcing caused by deposition of disturbed desert dust ( $17\text{--}37\text{ W m}^{-2}$  in 2005 and  $39\text{--}59\text{ W m}^{-2}$  in 2006) using the snow energy balance model SNOBAL (*Marks et al.*, 1998), which uses a two-layer snowmelt approach with an active 25 cm surface layer and the reminder of the snowpack as a second layer.

Essentially, both internal properties of snow cover and external factors affect snow albedo (*Aoki et al.*, 1999). The former properties include profiles of snow grain size and snow impurity concentrations (*Wiscombe and Warren*, 1980; *Warren and Wiscombe*, 1980; *Aoki et al.*, 2000, 2003). The latter include cloud amount, atmospheric constituents such as aerosol and absorptive gases, and solar zenith angle (*Wiscombe and Warren*, 1980; *Aoki et al.*, 1999). In general, the near-infrared albedo is strongly affected by snow grain size (*Wiscombe and Warren*, 1980), while the visible albedo depends on snow impurities (*Warren and Wiscombe*, 1980). However, land surface models (LSMs) that are incorporated into general circulation models (GCMs) developed for use in climate simulations calculate snow albedo with functions of only a few surrogate variables such as snow surface temperature or snow age (e.g., *US Army Corps of Engineers*, 1956; *Etchevers et al.*, 2004; *Pedersen and Winther*, 2005; *Qu and Hall*, 2007). Because there is little consensus regarding the formulation of snow albedo parameterizations (*Armstrong and Brun*, 2008), there exists a large inter-model range in the strength of snow albedo feedback (*Qu and Hall*, 2007). Moreover the lack of

sufficient reproducibility in such snow albedo parameterizations leads to uncertainties in GCM climate simulations.

Recently several authors have developed physically based snow albedo models for LSMs to improve the accuracy of GCM climate simulations (*Flanner and Zender, 2005; Gardner and Sharp, 2010; Yasunari et al., 2011; Aoki et al., 2011*). *Flanner and Zender (2005)* developed a two-stream, multi-layer, SNow, ICe, and Aerosol Radiation (SNICAR) model to calculate snow albedo and solar heating profile in snowpack. *Gardner and Sharp (2010)* developed a computationally simple, theoretically based parameterization for the broadband albedo of snow and ice. Their parameterization depends on the specific surface area (SSA) of snow or ice, BC concentration, solar zenith angle, cloud optical thickness, and snow depth. *Kuipers Munneke et al. (2011)* implemented this parameterization into a regional climate model for Antarctica and improved the model performance. *Yasunari et al. (2011)* developed a snow albedo model that was a function of snow impurity, solar zenith angle, and SSA. Incorporation of the model into their LSM led to an improvement of snow depth estimates. *Aoki et al. (2011)* developed a physically based snow albedo model (PBSAM) to calculate snow albedo and solar heating profile in snowpack. In PBSAM factors that affect snow albedo are explicitly taken into account by using a look-up table calculated with a spectrally detailed radiative transfer model for the atmosphere-snow system (*Aoki et al., 1999, 2000, 2003*). PBSAM takes into consideration the spectral distribution of the shortwave radiant flux in snowpack by dividing the broadband into several spectral sub-bands.

In general, these snow albedo models require optically equivalent snow grain size (hereafter “snow grain size”) (e.g., *Giddings and LaChapelle, 1961; Dobbins and Jizmagian, 1966; Pollack and Cuzzi, 1980; Wiscombe and Warren, 1980*) or SSA as an input parameter. The temporal evolution of snow microstructure, which affects temporal changes in snow grain size and SSA, is controlled by snow metamorphism processes. Some formulations that describe snow metamorphism

processes have been incorporated into detailed snowpack models like SNTHERM (*Jordan, 1991*), CROCUS (*Brun et al., 1989, 1992; Jacobi et al., 2010*), and SNOWPACK (*Bartelt and Lehning, 2002; Lehning et al., 2002a, 2002b*) or snow albedo models like SNICAR (*Flanner and Zender, 2006*). Since these formulations generally depend on snow temperature and water content profiles, LSMs should calculate internal physical states of snowpack accurately in order to utilize physically based snow albedo models and to realize their best potential in LSMs.

These considerations motivated us to develop a multilayered physical snowpack model for climate studies. The model, named Snow Metamorphism and Albedo Process (SMAP), incorporates PBSAM and is able to bring out PBSAM's potential accuracy in LSMs. In the SMAP model, PBSAM (*Aoki et al., 2011*) calculates snow albedo and solar heating profile in snowpack with profiles of snow grain size and snow water equivalent (SWE) calculated in SMAP, together with snow impurities externally given from in situ measurements or host GCMs. SMAP also introduces processes of energy and mass balance in snowpack, snow settlement, phase changes, water percolation, and snow metamorphism.

The purposes of this paper are to describe the processes that SMAP simulates, to validate the predictions of the model with observations, and to demonstrate the availability of SMAP for climate studies. The model validation utilizes in situ data from the two winters of 2007–2008 and 2008–2009 at Sapporo, Japan. The simulated parameters compared with observations are snow depth, column-integrated SWE, Column-average snow density, snow grain shape profiles, snow surface temperature, snow grain size in the top 2 cm, and broadband albedos. Because we employed the same data as *Aoki et al. (2011)*, we were able to determine whether SMAP could exploit PBSAM's potential by comparing the accuracy of simulated broadband albedos with their results. The comparison was informative because they calculated broadband albedos with measured (1) vertical profiles of snow grain size, (2) mass concentrations of snow impurities, and (3) SWE, whereas

**Table 2.1.** Input Parameters of SMAP.

Description	Notation	Units
Precipitation		mm
Air pressure		hPa
Wind speed	$u$	$\text{m s}^{-1}$
Air temperature		$^{\circ}\text{C}$
Relative humidity		%
Downward UV-visible and near-infrared radiant fluxes <sup>b</sup>		$\text{W m}^{-2}$
Diffuse components of UV-visible and near-infrared radiant fluxes <sup>b</sup>		$\text{W m}^{-2}$
Downward longwave radiant flux		$\text{W m}^{-2}$
Ground heat flux	$H_G$	$\text{W m}^{-2}$
Mass concentrations of snow impurities (BC <sup>a</sup> and dust)		ppmw

<sup>a</sup>Black carbon.

<sup>b</sup>Downward shortwave radiant flux is possible, alternatively.

SMAP simulates the first and third of these parameters. Finally, we demonstrated the application of SMAP to climate studies by investigating the effects of snow impurities on snowmelt at Sapporo by carrying out a simulated “pure snow experiment” wherein no snow impurities were assumed. We presented the effects in terms of changes in snowpack durations, radiative forcings, and albedo reductions due to snow impurities. In general, qualities and quantities of snow impurities differ from place to place. It in turn implies that their impacts on reducing broadband albedos also vary by location. Thus it is worth employing SMAP to assess snow impurity effects on snowmelt at Sapporo,

**Table 2.2.** Representative Output Parameters of SMAP.

Description	Notation	Units
Snow depth	$D$	m
UV-visible albedo		
Near-infrared albedo		
Shortwave albedo	$\alpha$	
Snow surface temperature	$T_{s0}$	°C
Net shortwave radiant flux	$S_{net}$	W m <sup>-2</sup>
Net longwave radiant flux	$L_{net}$	W m <sup>-2</sup>
Sensible heat flux	$H_S$	W m <sup>-2</sup>
Latent heat flux	$H_L$	W m <sup>-2</sup>
Energy exchange due to rainfall	$H_R$	W m <sup>-2</sup>
Conductive heat flux		W m <sup>-2</sup>
Snow temperature (in each layer)	$T_s$	°C
Snow density (in each layer)	$\rho_s$	kg m <sup>-3</sup>
Snow water equivalent (in each layer, and column-integrated)		kg m <sup>-2</sup>
Liquid water content (in each layer, and column-integrated)		kg m <sup>-2</sup>
Bottom runoff rate	$M_{out, r}$	kg m <sup>-2</sup> s <sup>-1</sup>
Snow grain size (in each layer)	$r_{opt}$	mm
Sphericity (in each layer)	$sp$	
Dendricity (in each layer)	$dd$	
Snow grain shape (in each layer)		

where climate conditions and snow impurity types are different from other places investigated by the previous works (e.g., *Painter et al.*, 2007).

## 2.2. Model description

SMAP is a one-dimensional multilayered snowpack model for calculating the temporal evolution of the physical characteristics of snow. SMAP models snowpack as an accumulation of snow layers composed of ice, water, and moist air. Some unique input parameters are required in addition to the

**Table 2.3.** Processes Implemented in SMAP.

Process	Method or references	Section
Energy balance of snowpack	Diffusion equation	2.2.1
Effective thermal conductivity of snow	<i>Devaux</i> (1933)	2.2.1
Solar heating profile in snowpack	PBSAM ( <i>Aoki et al.</i> , 2011)	2.2.1
Snow albedo	PBSAM ( <i>Aoki et al.</i> , 2011)	2.2.1
Obukhov length	<i>Kondo</i> (1994)	2.2.1
Roughness length for heat and moisture	<i>Andreas</i> (1987)	2.2.1
Profile function for stable condition	<i>Holtslag and De Bruin</i> (1988)	2.2.1
Profile function for unstable condition	<i>Paulson</i> (1970)	2.2.1
New snow:rain ratio	<i>Yamazaki</i> (1998, 2001)	2.2.2
Surface hoar	<i>Föhn</i> (2001)	2.2.2
New snow density	<i>Yamazaki</i> (1998)	2.2.2
Snowpack settlement	Densification equation	2.2.3
Viscosity coefficient of snow	<i>Bader and Weilenmann</i> (1992) and <i>Morris et al.</i> (1997)	2.2.3
Geometric model of ice particles	<i>Lehning et al.</i> (2002a)	2.2.4
New snow grain size	Parameterization compiled from <i>Motoyoshi et al.</i> (2005), <i>Aoki et al.</i> (2007a, 2007b), and <i>Taillandier et al.</i> (2007)	2.2.4
Equi-temperature metamorphism	<i>Lehning et al.</i> (2002a)	2.2.4
Temperature gradient metamorphism	<i>Lehning et al.</i> (2002a)	2.2.4
Wet snow metamorphism	<i>Lehning et al.</i> (2002a)	2.2.4
snow metamorphism under alternating temperature gradients	<i>Pinzer and Schneebeli</i> (2009)	2.2.4
Snow grain shape classification	<i>Lehning et al.</i> (2002a)	2.2.4
Conversion from geometric grain size to optical equivalent grain size	<i>Grenfell and Warren</i> (1999) <i>Neshyba et al.</i> (2003), <i>Grenfell et al.</i> (2005)	2.2.4
Numerical solution for diffusion equation	Crank-Nicolson finite difference implicit method	2.2.5
Boundary condition at the snow surface	Neumann boundary condition	2.2.5
Boundary condition at the bottom of snowpack	Neumann boundary condition	2.2.5
Water percolation	<i>Yamazaki</i> (1998, 2001)	2.2.5

meteorological parameters ordinarily required as input by other snowpack models (e.g., *Langlois et al.*, 2009) (Table 2.1). The unique parameters are the mass concentrations of snow impurities, the downward ultraviolet (UV)-visible (wavelength  $\lambda = 0.2\text{--}0.7\ \mu\text{m}$ ) and near-infrared ( $\lambda = 0.7\text{--}3.0\ \mu\text{m}$ ) radiant fluxes, and their diffuse fractions. These parameters are used in the PBSAM component of SMAP. When the downward UV-visible and near-infrared radiant fluxes, and their diffuse fractions are not available, SMAP calculates them from the downward shortwave ( $\lambda = 0.2\text{--}3.0\ \mu\text{m}$ ) radiant flux, which is necessary in this case, following a scheme by *Goudriaan* (1977) as functions of cloud fraction and solar zenith angle. In this option SMAP calculates cloud fraction following the approach by *van den Broeke et al.* (2004, 2006) as functions of internally calculated net longwave radiant fluxes at the snow surface and air temperature. The model calculates all snow physical parameters relevant to snow-atmosphere interactions such as broadband albedos, snow surface temperature, and energy fluxes at the snow surface (Table 2.2). SMAP calculates broadband albedos in the UV-visible, near-infrared, and shortwave spectra. SMAP also calculates internal physical parameters of snowpack such as snow temperature, snow density, snow grain size, and snow grain shape.

The following sections describe the physical processes and numerical solutions used in SMAP (Table 2.3). Further attempts will be needed to optimize SMAP for LSMs. For example, computational costs can be reduced by neglecting some processes that have little effect on snow-atmosphere interactions (*Loth and Graf*, 1998; *Armstrong and Brun*, 2008). However, such optimization is beyond the scope of this paper.

### **2.2.1. Energy balance of snowpack**

We assume that total heat and radiant energy are conserved within snowpack and are exchanged at both the snow surface and bottom of the snowpack. In snowpack the  $z$  coordinate is taken to be positive in a downward direction from the snow surface. SMAP formulates energy conservation in

snowpack by using a one-dimensional diffusion equation that takes solar heating in snowpack and melt-freeze cycles into account:

$$c_s \rho_s \frac{\partial T_s}{\partial t} = \frac{\partial}{\partial z} \left( k_{eff} \frac{\partial T_s}{\partial z} \right) - \frac{\partial S_{net}}{\partial z} - L_f R_{mr}, \quad (2.1)$$

where  $c_s$  is the specific heat capacity of snow at constant pressure,  $\rho_s$  is snow density,  $T_s$  is snow temperature,  $t$  is time,  $k_{eff}$  is the effective thermal conductivity of snow,  $S_{net}$  is the net shortwave radiant flux in snowpack,  $L_f$  is the latent heat of fusion, and  $R_{mr}$  is the difference between the melting and refreezing rates. Here  $\rho_s$  is defined as

$$\rho_s = \rho_i \theta_i + \rho_w \theta_w + \rho_a \theta_a, \quad (2.2)$$

where  $\rho_i$ ,  $\rho_w$  and  $\rho_a$  are the densities of ice, water, and air, respectively, and  $\theta_i$ ,  $\theta_w$ , and  $\theta_a$  are the volumetric fractions of ice, water, and air, respectively. Again  $c_s$  is defined as

$$c_s = \frac{c_i \rho_i \theta_i + c_w \rho_w \theta_w + c_a \rho_a \theta_a}{\rho_s}, \quad (2.3)$$

where  $c_i$ ,  $c_w$  and  $c_a$  are the specific heat capacities of ice, water, and air, respectively.

The integral of equations (2.1) determines the temporal evolution of  $T_s$  following specification of its initial value, which is the temperature for new snow or surface hoar. We assume the initial temperature to equal the ground wet bulb temperature  $T_w$  when snowfall occurred. In this numerical procedure (see Sect. 2.2.5), we prescribe Neumann boundary conditions both at the snow surface and the bottom of snowpack. At the snow surface the condition is written as



$$k_{eff} \frac{\partial T_s}{\partial z} = L_{net} + H_S + H_L + H_R, \quad (2.4)$$

where  $L_{net}$ ,  $H_S$ ,  $H_L$ , and  $H_R$  are the net longwave radiant flux, sensible heat flux, latent heat flux, and energy exchange due to rainfall, respectively, at the snow surface. At the bottom of snowpack the condition is

$$k_{eff} \frac{\partial T_s}{\partial z} = H_G, \quad (2.5)$$

where  $H_G$  is the ground heat flux. Energy fluxes such as  $S_{net}$ ,  $L_{net}$ ,  $H_S$ ,  $H_L$ ,  $H_P$ , and  $H_G$  are defined to be positive when they are directed downward. We calculate  $k_{eff}$  ( $\text{W m}^{-1} \text{K}^{-1}$ ) with a simple parameterization as a function of  $\rho_s$  ( $\text{kg m}^{-3}$ ) (Devaux, 1933):

$$k_{eff} = 0.029(1 + 10^{-4} \rho_s^2), \quad (2.6)$$

according to Yamazaki (1998, 2001).

We calculate the divergence of the net shortwave radiant flux  $\partial S_{net} (\partial z)^{-1}$  and snow albedo in the shortwave spectrum  $\alpha$  with PBSAM (Aoki *et al.*, 2011). The input snow parameters for PBSAM are vertical profiles of snow grain size, mass concentrations of snow impurities, and SWE. The input parameters needed to calculate solar illumination conditions for PBSAM are the solar zenith angle, downward radiant fluxes in the UV-visible and near-infrared bands, their diffuse fractions, and the underlying surface albedos. The relationship between  $\partial S_{net} (\partial z)^{-1}$  and the downward shortwave radiant flux  $S^\downarrow$  is written as follows:

$$-\int_0^D \frac{\partial S_{net}}{\partial z} dz = (1 - \alpha)S^\downarrow, \quad (2.7)$$

where  $D$  is snow depth, and  $S^\downarrow$  is taken directly from input data. According to *Aoki et al.* (2011), one UV-visible subband and three near-infrared subbands are necessary in PBSAM to obtain accurate estimates of broadband albedos. In addition, they showed that the accuracy of broadband albedos obtained with three or more subbands in both the UV-visible and near-infrared bands is almost the same when the number of model snow layers is fixed. They also demonstrated that more than three subbands in both the UV-visible and near-infrared bands were necessary to obtain a sufficiently accurate solar heating profile in snowpack. In the present paper we employed four UV-visible subbands ( $\lambda = 0.200\text{--}0.475$ ,  $0.475\text{--}0.550$ ,  $0.550\text{--}0.625$ , and  $0.625\text{--}0.700$   $\mu\text{m}$ ) and for near-infrared subbands ( $\lambda = 0.700\text{--}0.950$ ,  $0.950\text{--}1.125$ ,  $1.125\text{--}1.400$ , and  $1.400\text{--}3.000$   $\mu\text{m}$ ), respectively, as explained in Sect. 2.2.5.

SMAP equates the net longwave radiant flux  $L_{net}$  to the difference between the downward longwave radiant flux determined from input data and the upward longwave radiant flux calculated by using the Stefan-Boltzmann law with snow surface temperature  $T_{s0}$ , together with a snow surface emissivity of 0.98 (*Armstrong and Brun*, 2008).

SMAP calculates both the sensible heat flux  $H_s$  and latent heat flux  $H_L$  at the snow surface by the bulk method, which utilizes values of wind speed at a measurement height and differences in potential temperature and specific humidity between a measurement height and the snow surface. These two turbulent fluxes are expressed by

$$H_s = \frac{\rho_a c_p \kappa^2 u (\theta - \theta_{s0})}{\left[ \ln\left(\frac{z_{ref}}{z_0}\right) - \psi_M\left(\frac{z_{ref}}{L}\right) \right] \left[ \ln\left(\frac{z_{ref}}{z_H}\right) - \psi_H\left(\frac{z_{ref}}{L}\right) \right]}, \quad (2.8)$$

and

$$H_L = \frac{\rho_a L_v \kappa^2 u (q - q_{s0})}{\left[ \ln\left(\frac{z_{ref}}{z_0}\right) - \Psi_M\left(\frac{z_{ref}}{L}\right) \right] \left[ \ln\left(\frac{z_{ref}}{z_Q}\right) - \Psi_H\left(\frac{z_{ref}}{L}\right) \right]}, \quad (2.9)$$

where  $c_{pa}$  is the specific heat capacity of air at constant pressure,  $L_v$  is the latent heat of sublimation or evaporation,  $\kappa$  is von Kármán constant,  $u$  is ground wind speed,  $\Theta$  and  $\Theta_{s0}$  are potential temperature at the ground and the snow surface, respectively,  $q$  and  $q_{s0}$  are specific humidity at the ground and the snow surface, respectively,  $\Psi_M$  and  $\Psi_H$  are profile functions for momentum and heat, respectively,  $z_{ref}$  is a measurement height above the snow surface,  $z_0$ ,  $z_H$ , and  $z_Q$  are roughness lengths for momentum, heat, and moisture, respectively, and  $L$  is Obukhov length. SMAP calculates  $\Theta_{s0}$  and  $q_{s0}$  directly from  $T_{s0}$  by using the assumption that the snow surface is saturated.

To obtain these turbulent heat fluxes, SMAP first calculates the bulk Richardson number  $Ri$ , which is a measure of stability conditions in the atmospheric boundary layer, as follows:

$$Ri = \frac{g z_{ref}}{\Theta_v} \frac{\Theta_v - \Theta_{v,s0}}{u^2}, \quad (2.10)$$

where  $\Theta_v$  and  $\Theta_{v,s0}$  are virtual potential temperature at the ground and the snow surface, respectively. According to *Andreas* (2002) turbulence presumably ceases, and the flow becomes laminar when  $Ri$  exceeds a critical value (critical Richardson number) under stable conditions. Thus in SMAP we set  $H_S$  and  $H_L$  equal to 0 when  $Ri$  exceeds the critical Richardson number. Although there is no established value of the critical Richardson number (*Andreas*, 2002), we use a value of 0.25 following *Garratt* (1992). On the other hand, it has long been pointed out that turbulence can persist

even under very stable conditions (*Webb, 1970; Kondo et al., 1978; Holtslag and de Bruin, 1988; Beljaars and Holtslag, 1991; Mahrt et al., 1999, 2008; Cheng et al., 2005; Grachev et al., 2007; Galperin et al., 2007*), though a well-established formulation has not been developed yet. Effects on the model accuracy of the present modeling approach for very stable condition are discussed in Sect. 2.4.3. When  $Ri$  is less than the critical Richardson number,  $L$  is approximated and calculated with  $Ri$  following *Kondo (1994)*:

$$L = \begin{cases} \frac{z_{ref}}{R_i - 0.003} & \text{for } |R_i| < 0.05, \\ \frac{z_{ref}}{R_i} & \text{for } R_i < -0.05, \\ \frac{z_{ref}}{R_i} (1 + 6R_i) & \text{for } R_i > 0.05. \end{cases} \quad (2.11)$$

SMAP calculates roughness lengths for heat and moisture ( $z_H$  and  $z_Q$ ) according to *Andreas (1987)*:

$$\ln\left(\frac{z_H}{z_0}\right) = \begin{cases} 1.25 & \text{for } R_* \leq 0.135, \\ 0.149 - 0.550 \ln R_* & \text{for } 0.135 < R_* < 2.5, \\ 0.317 - 0.565 \ln R_* - 0.180 (\ln R_*)^2 & \text{for } 2.5 \leq R_* \leq 1000. \end{cases} \quad (2.12)$$

$$\ln\left(\frac{z_Q}{z_0}\right) = \begin{cases} 1.61 & \text{for } R_* \leq 0.135, \\ 0.351 - 0.628 \ln R_* & \text{for } 0.135 < R_* < 2.5, \\ 0.396 - 0.512 \ln R_* - 0.180 (\ln R_*)^2 & \text{for } 2.5 \leq R_* \leq 1000. \end{cases} \quad (2.13)$$

where  $R_*$  is the roughness Reynolds number. The choice of profile functions ( $\Psi_M, \Psi_H$ ) depends on stability conditions in the atmospheric boundary layer. When the atmosphere is stable, SMAP assumes that  $\Psi_M = \Psi_H$  and calculates the profile functions according to *Holtslag and De Bruin (1988)*:

$$\Psi_M = \Psi_H = -0.7 \frac{z_{ref}}{L} - 0.75 \left( \frac{z_{ref}}{L} - 14.286 \right) \exp \left( -0.35 \frac{z_{ref}}{L} \right) - 10.714. \quad (2.14)$$

When the atmosphere is unstable, SMAP carries out the calculations with functions determined by *Paulson* (1970):

$$\Psi_M = 2 \ln \left( \frac{1+x}{2} \right) + \left( \frac{1+x^2}{2} \right) - 2 \tan^{-1} x + \frac{\pi}{2}, \quad (2.15)$$

$$\Psi_H = 2 \ln \left( \frac{1+x^2}{2} \right), \quad (2.16)$$

where  $x$  is defined as

$$x = \left( 1 - 16 \frac{z_{ref}}{L} \right)^{1/4}. \quad (2.17)$$

In general,  $z_0$  for the snow surface is of the order of  $10^{-4}$  to  $10^{-3}$  m depending on the condition of the snow surface. In this study, we treat  $z_0$  as a constant parameter equal to  $2.3 \times 10^{-4}$  m, which is the value obtained by *Kondo and Yamazawa* (1986) for seasonal snow.

Finally,  $H_R$  is written as

$$H_R = \rho_w c_{pw} R_r (T_w - T_{s0}), \quad (2.18)$$

where  $c_{pw}$  is the specific heat capacity of water at constant pressure,  $R_r$  is rainfall rate, and we assume that the rain temperature equals  $T_w$  (*Loth et al.*, 1993).

### 2.2.2. Mass balance of snowpack

SMAP expresses the mass of the snowpack in terms of water equivalent. Snowfall, rainfall, and surface hoar add to the mass of the snowpack. Surface sublimation and liquid water runoff at the bottom of the snowpack decrease the mass of the snowpack. The mass balance is formulated as follows:

$$M_{in,p} + M_{in,sh} = \frac{d}{dt} \left( \int_0^D \rho_s dZ \right) + M_{out,r} + M_{out,ss}, \quad (2.19)$$

where  $M_{in,p}$  is the precipitation (snowfall and rainfall) rate,  $M_{in,sh}$  is the surface hoar rate,  $M_{out,r}$  is the runoff rate at the bottom of the snowpack, and  $M_{out,ss}$  is the surface sublimation rate. SMAP calculates the change in mass during a simulation period, which can be arbitrary, and Eq. 2.19 is always valid during the period.

SMAP partitions the precipitation rate, which is taken directly from the input data, into snow and rain rates by using the algorithm to calculate snow:rain ratios as a function of  $T_w$  parameterized by *Yamazaki* (1998, 2001). Surface hoar is created when SMAP determines that  $H_L$  is positive and ground wind speed is less than  $3 \text{ m s}^{-1}$  (*Föhn*, 2001). This constrains SMAP not to create much surface hoar because SMAP sets  $H_L$  equal to 0 when  $Ri$  exceeds the critical Richardson number as explained in Sect. 2.2.1. In order to confirm whether the above mentioned modeling procedure is robust or not, it is necessary to perform detailed snow pit observations together with micrometeorological measurements and modeling work in the future. In contrast, surface sublimation occurs when SMAP determines  $H_L$  to be negative.  $|H_L/L_v|$  is equivalent to surface hoar rate or surface sublimation rate.

Snow settlement, melting and refreezing, and water percolation affect  $\rho_s$  and  $M_{out,r}$  and thus the mass balance of the snowpack. We describe snow settlement in Sect. 2.2.3 and the other processes in Sect. 2.2.5.

### 2.2.3. Snow settlement

Snow settlement increases  $\rho_s$ , and is given by a densification equation:

$$\frac{1}{\rho_s} \frac{\partial \rho_s}{\partial t} = \frac{\sigma}{\eta}, \quad (2.20)$$

where  $\sigma$  is overburden pressure, and  $\eta$  is the viscosity coefficient of snow. We parameterize  $\eta$  according to *Bader and Weilenmann* (1992) and *Morris et al.* (1997):

$$\eta = 0.18 \times 10^{-5} \exp \left[ 0.02 \rho_s + \frac{8110}{(T_s + 273.15)} \right], \quad (2.21)$$

This equation performs well for seasonal snow, though it tends to underestimate  $\eta$  for polar snow (*Morris et al.*, 1997). To initialize  $\rho_s$  for new snow or surface hoar, we have to calculate new snow density. Unfortunately, a parameterization of new snow density that can be applicable globally has not been developed yet. For example, when *Yamaguchi et al.* (2004) applied SNOWPACK (*Bartelt and Lehning*, 2002; *Lehning et al.*, 2002a, 2002b) to the wet-snow region in Japan, they employed an empirical parameterization as functions of air temperature and wind speed obtained from data gathered in the northern part of Honshu Island, Japan instead of the original function of SNOWPACK (*Lehning et al.*, 2002b). Although SMAP is equipped with the functions by *Yamaguchi et al.* (2004) and *Lehning et al.* (2002b), we employ a parameterization for new snow density  $\rho_{s,new}$  (kg m<sup>-3</sup>) as a function of wind speed  $u$  (m s<sup>-1</sup>) introduced by *Yamazaki* (1998, 2001):

$$\rho_{s,new} = 67 + 13u, \quad (2.22)$$

because it was developed and well validated under the climate condition at Sapporo. When SMAP is applied to global climate simulations, the parameterization can be inadequate. In this case it should be changed.

#### 2.2.4. Snow metamorphism

Snow metamorphism processes control temporal changes in optically equivalent snow grain radius  $r_{opt}$  (in this paper, we refer to “snow grain size”). To simulate the processes, we employ the model geometry for a snow grain developed by the SNOWPACK model (*Lehning et al.*, 2002a), where a neck connects two spherical ice particles and the related prognostic parameters are calculated (Fig. 2.1). The parameters are the geometric snow grain radius  $r_g$ , bond size  $r_b$ , dendricity  $dd$ , and sphericity  $sp$ , where  $r_g$  is the radius of each ice particle,  $r_b$  is the minimum constriction in a neck (*Lehning et al.*, 2002a),  $dd$  describes the part of the original snow grain shape that is still remaining in a snow layer, and  $sp$  describes the ratio of rounded versus angular snow grain shapes (*Brun et al.*, 1992). Both  $dd$  and  $sp$  range between 0 and 1. The assumption for new snow is that  $dd = 1$  and  $sp = 0.5$ . Combinations of these four parameters and water content determine snow grain shape (*Lehning et al.*, 2002a). The model geometry of the two connected ice particles considered here is a geometrically nonspherical particle. A geometrically nonspherical particle is optically represented by a collection of independent spheres that have the same volume-to-surface-area (V/A) ratio as the nonspherical particle (*Grenfell and Warren*, 1999; *Neshyba et al.*, 2003; *Grenfell et al.*, 2005). SMAP therefore calculates  $r_{opt}$  with the following equation (*Grenfell and Warren*, 1999):

$$r_{opt} = \frac{3}{SSA_v}, \quad (2.23)$$



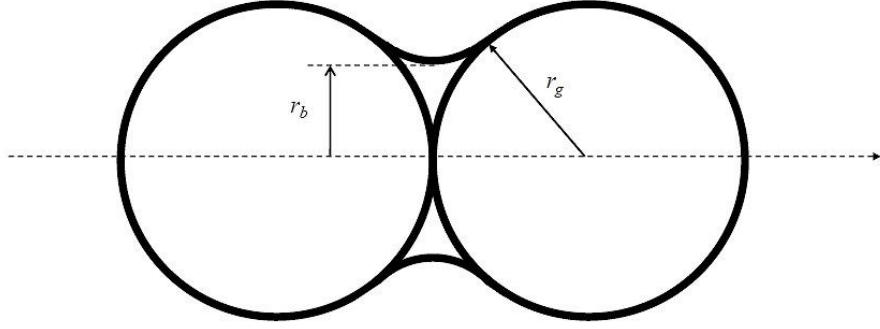


**Figure 2.1.** Model geometry of a snow grain as employed in SMAP. Two spherical ice particles with geometric snow grain radius  $r_g$  and bond size  $r_b$  are connected by a neck (*Lehning et al.*, 2002a).

where  $SSA_v$  is SSA per unit volume, and  $SSA_v$  is written as a function of the model geometry's volume  $V_g$  and surface area  $A_g$  as

$$SSA_v = \frac{A_g}{V_g}. \quad (2.24)$$

From the model geometry (Fig. 2.1),  $V_g$  and  $A_g$  are calculated as

$$V_g = \frac{4}{3}\pi r_g^3 + \frac{4}{3}\pi(r_g^2 - r_b^2)^{\frac{3}{2}} + 2\pi r_b^2 r_g, \quad (2.25)$$

$$A_g = 4\pi r_g \left( r_g + \sqrt{r_g^2 - r_b^2} \right) + 4\pi r_b \left( r_g + \sqrt{r_g^2 - r_b^2} \right). \quad (2.26)$$

SMAP employs the same prognostic equations, which describe temporal changes in  $r_g$ ,  $r_b$ ,  $dd$ , and  $sp$ , as those used in SNOWPACK (*Lehning et al.*, 2002a), in which three types of snow metamorphism processes are considered: (1) equi-temperature metamorphism, (2) temperature gradient metamorphism, and (3) wet snow metamorphism. Equi-temperature metamorphism occurs when snow is dry and the absolute snow temperature gradient is small (less than  $5 \text{ K m}^{-1}$ ). This process forms decomposing and fragmented precipitation particles as well as rounded grains. Temperature gradient metamorphism occurs when snow is dry and the absolute snow temperature gradient is large (more than  $5 \text{ K m}^{-1}$ ). Faceted crystals and depth hoar are formed through this process. Wet snow metamorphism occurs when snow contains liquid water. Melt forms are created in this case. However, recently *Pinzer and Schneebeli* (2009) demonstrated that small rounded grains can be formed even when the temperature gradient is large if the sign of the temperature gradient changes with a 24-h cycle. We implicitly consider this kind of snow metamorphism under an alternating temperature gradient regime by forcing the temperature gradient metamorphism not to occur in the top 20 cm of the snowpack. We discuss the validity of this procedure in Sect. 2.4.4.

To calculate the temporal evolution of  $r_{opt}$  it is necessary to initialize  $r_{opt}$  for both new snow and surface hoar. For this purpose, we use  $r_{opt0}$  ( $\mu\text{m}$ ), which is the initial value of  $r_{opt}$ , and the following empirical equation as a function of air temperature  $T_a$  ( $^{\circ}\text{C}$ ):

$$r_{opt0} = \begin{cases} 20 & \text{for } T_a \leq -30, \\ 10^{\left[\frac{1}{20}(\log_{10} 40 - \log_{10} 20)(T_a + 10) + \log_{10} 40\right]} & \text{for } -30 < T_a \leq -10, \\ 10^{\left[\frac{1}{10}(\log_{10} 65 - \log_{10} 40)T_a + \log_{10} 65\right]} & \text{for } -10 < T_a \leq 0, \\ 65 & \text{for } T_a > 0. \end{cases} \quad (2.27)$$

These equations are based on the snow pit measurements at Kitami, Hokkaido (*Aoki et al.*, 2003), Shinjyo, Yamagata, (*Motoyoshi et al.*, 2005), and Sapporo, Hokkaido (*Aoki et al.*, 2007a, 2007b)

Japan in areas of seasonal snow cover. We describe the measurement technique for  $r_{opt}$  briefly in Sect. 2.3.2. The maximum  $r_{opt0}$  of 65  $\mu\text{m}$  in Eq. 2.27 is determined from the results of *Taillandier et al.* (2007) for wet snow. The initial values of  $r_g$  and  $r_b$  can be calculated from Eqs. 2.23, 2.24, 2.25, and 2.26 by assuming  $r_b = r_g/4$  for new snow (*Lehning et al.*, 2002a).

### 2.2.5. Numerical solution

SMAP assumes each snow layer to have a thickness  $d$  that is allowed to range between  $d_{min}$  and  $d_{max}$ . When  $d$  exceeds  $d_{max}$ , SMAP divides the layer into two layers that have the same snow physical parameters. On the other hand, when  $d$  becomes less than  $d_{min}$ , SMAP adds this thin layer to the adjacent lower layer. When new snow falls or surface hoar forms, SMAP adds a new snow layer to the top of the snowpack. A grid point retaining the values of simulated snow physical parameters is located at the center of each snow layer. Using forcing provided by input data SMAP approximates and solves the energy balance equation (Eq. 2.1) with the Crank-Nicolson finite difference implicit method where Neumann boundary conditions, which is prescribed in terms of snow temperature gradients at both the snow surface and the bottom of the snowpack (Eqs 2.4 and 2.5), are imposed. In this numerical procedure, we have to pay attention to the values of the time step  $\Delta t$ ,  $d$ , and  $k_{eff}$  to avoid possible numerical instabilities. We discuss the values chosen for these parameters in Sect. 2.4.

SMAP diagnoses snow melting and refreezing at every time step with  $T_s$  predicted by the energy balance equation. When  $T_s$  is positive, melting occurs. In contrast, when  $T_s$  is negative and liquid water exists, refreezing occurs. In both cases SMAP expresses the change in  $\theta_w$  during one time step,  $\Delta\theta_w$ , by

$$\Delta\theta_w = \frac{c_s \rho_s T_s}{L_f \rho_w}. \quad (2.28)$$

In cases where  $T_s$  is positive, SMAP sets  $T_s$  to 0 °C after this calculation.

## 2.3. Field measurements at Sapporo

### 2.3.1. Meteorological measurements

During 2007–2009 we carried out meteorological measurements at an automated weather station (AWS) installed at the Institute of Low Temperature Science, Hokkaido University (43°04'56"N, 141°20' 30"E, 15 m a.s.l), which is located in an urban area of Sapporo city, Hokkaido, Japan (*Aoki et al.*, 2006) We used data averaged every 30 min or integrated over every 30 min (precipitation only) as input and validation values for SMAP.

For input data, we corrected measured precipitation for catch efficiencies for snow and rain as functions of gauge type and wind speed with algorithms developed by *Yokoyama et al.* (2003). The downward UV-visible radiant flux ( $\lambda = 0.305\text{--}0.708\ \mu\text{m}$ ) was not measured directly but instead was calculated by subtracting the measured downward near-infrared radiant flux ( $\lambda = 0.708\text{--}2.8\ \mu\text{m}$ ) from the measured downward shortwave radiant flux ( $\lambda = 0.305\text{--}2.8\ \mu\text{m}$ ). The diffuse/direct ratios of the downward radiant fluxes in both the UV-visible and the near-infrared regions were also not measured directly. They were obtained by assuming these ratios to be the same as the corresponding ratio for downward shortwave radiant flux, though this approximation can cause a small error in calculated broadband snow albedo (*Aoki et al.*, 2011). We also corrected the ground heat flux measured during the ablation period (March and April) because diurnal variations in this flux are enhanced when the ground is exposed. If simulated melting is delayed compared to observed one, large variations in the ground heat flux have a proportionate effect on the model simulations. To minimize this effect, we assumed constant ground heat fluxes during the ablation period while the observed snow depth was less than 0.2 m. These values were  $-2.35\ \text{W m}^{-2}$  in the winter of 2007–2008 and  $-1.95\ \text{W m}^{-2}$  in the winter of 2008–2009. We obtained these values when the measured snow depth was 0.2 m. They are very similar to the value of  $-2\ \text{W m}^{-2}$  employed in CROCUS when

the snow temperature at the bottom of the snowpack was 0 °C (*Brun et al.*, 1989, 1992; *Essery et al.*, 1999).

For model validation we used the measured snow depth, snow surface temperature, and broadband albedos. Broadband albedos were calculated by the downward and upward radiant fluxes for UV-visible, near-infrared, and shortwave spectra, where the unmeasured upward UV-visible radiant flux was obtained in a similar way with the downward UV-visible radiant flux.

Model validation of broadband albedos requires close attention to the observed data (*Yamanouchi*, 1983; *Aoki et al.*, 2011, *Brandt et al.*, 2011) because accurate knowledge of the instrument's shadowing correction would be needed. In the present study we corrected the observed broadband albedo data that we used in this study considering the effect of a pyranometer mounting frame, which blocked 3.56 % of the upward flux in the case of isotropic upward radiation (*Aoki et al.*, 2011). The value was comparable with that obtained by *Yamanouchi* (1983) (3 – 5 %) at Mizuho station in east Antarctica.

### **2.3.2. Snow pit observations**

During the winters of 2007–2008 and 2008–2009, we carried out snow pit observations twice a week at about 1100 local time near the AWS. Observed parameters were snow depth, the snow grain shape profile, snow grain size, and Column-average snow density. We used the snow depth and Column-average snow density to calculate the column-integrated SWE. Snow grain size was observed for the top 2 cm and top 10 cm depths because we focused near-surface snow grain size, which strongly affects the broadband albedos. *Aoki et al.* (2000, 2003) defined snow grain size measured manually as one-half the branch width of dendrites or as one-half the width of the narrower portion of broken crystals “r<sub>2</sub>”. On the other hand snow grain shape was observed in the entire snowpack as we intended to confirm whether SMAP could reproduce detailed layer structure of snowpack or not. We

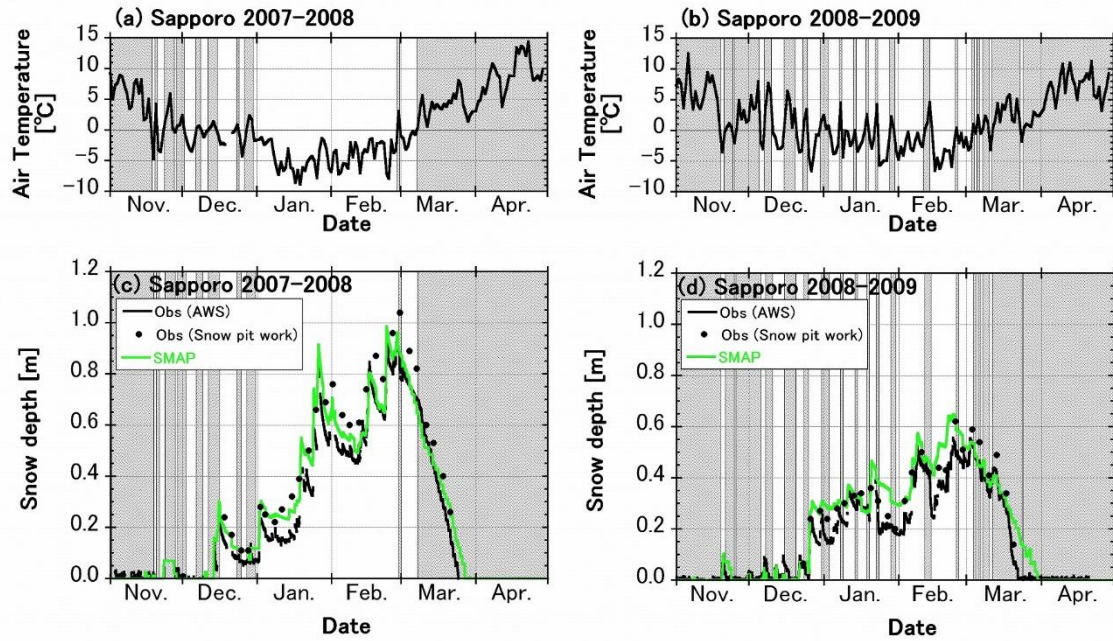


**Figure 2.2.** (a, b) Daily mean air temperature and (c, d) half-hourly snow depth observed during the 2007–2008 and 2008–2009 winters at Sapporo, Japan. Background shade indicate the periods when daily mean air temperature were above 0 °C. The shade is also indicated in the following figures that depict time series. Snow depths were measured by the AWS (black solid curve) and with snow pit observations (black filled circles). Half-hourly snow depth simulated by SMAP is also shown (green solid curve).

simultaneously collected snow samples for the top 2 cm and top 10 cm of the snowpack to measure the mass concentrations of dust and elemental carbon (EC) (*Kuchiki et al.*, 2009; *Aoki et al.*, 2011). In this study we assumed EC to be equivalent to BC following *Aoki et al.* (2011). *Aoki et al.* (2011) showed that snow impurities at Sapporo are characterized by high BC concentrations (an average during the two winters of 0.215 ppmw for the top 2 cm of the snowpack), which is much higher than those in Arctic snow.

**Table 2.4.** Comparison of SMAP Simulation Results with Measurements.

Parameters	Period <sup>a</sup>	$r^b$	$RMSE^c$	$ME^d$
Snow depth (m)	2007–2008	0.986	0.064	0.045
	2008–2009	0.959	0.075	0.044
SWE (mm)	2007–2008	0.950	41	–25
	2008–2009	0.932	42	–34
Snow density (kg m <sup>-3</sup> )	2007–2008	0.936	53	–42
	2008–2009	0.861	118	–108
Snow surface temperature (°C)	2007–2008	0.914	2.446	–0.301
	2008–2009	0.913	2.028	–0.666
Snow grain size (mm)	2007–2008	0.763	0.31	–0.04
	2008–2009	0.840	0.15	–0.02
UV-visible albedo	2007–2008	0.913	0.053	–0.010
	2008–2009	0.694	0.096	–0.003
Near-infrared albedo	2007–2008	0.854	0.064	–0.002
	2008–2009	0.792	0.085	0.023
Shortwave albedo	2007–2008	0.898	0.051	–0.007
	2008–2009	0.753	0.084	0.010

<sup>a</sup>Periods are November to April for both 2007–2008 and 2008–2009 winters.

<sup>b</sup>Correlation coefficient.

<sup>c</sup>Root mean square error.

<sup>d</sup>Mean error (the average of the difference between simulated values and observed values).

We used the measured mass concentrations of BC and dust for input data in this study. We equated the values in the top 2 cm model layers of the snowpack to the corresponding observed values. For the lower model layers of the snowpack, we gave the observed values for the top 10 cm of the snowpack equally. Data gaps existed for the days between snow pit observations. We estimated the missing data by using the values measured at the nearest points in time. For model validation we used vertical profiles of snow grain shape, the grain size of the snow in the top 2 cm of the snowpack, column-integrated SWE, and Column-average snow density.

### **2.3.3. Meteorological and snow conditions at Sapporo**

Sapporo is located in the southwest part of Hokkaido, Japan. It faces the Sea of Japan and is exposed to the cold winter northwesterly monsoon, which brings frequent snowfalls. The record of daily mean air temperature and half-hourly snow depth measured at Sapporo during the winters of 2007–2008 and 2008–2009 (Fig. 2.2) shows that the first winter was colder than the second. During the second winter air temperature often rose above 0 °C (Fig. 2.2b). Average daily mean air temperatures during the period from December to March were –1.58 °C for the first winter and –0.34 °C for the second. Snow depth after late January was greater during the first winter than during the second. In this paper we refer to November, December, January, and February as the “accumulation period” and March and April as the “ablation period”.

### **2.4. Model validation with data from Sapporo**

We evaluated SMAP with the data obtained during the winters of 2007–2008 and 2008–2009 at Sapporo. We compared the snow depth, column-integrated SWE, Column-average snow density, snow grain shape profile, snow surface temperature, snow grain size in the top 2 cm of the snowpack, and broadband albedos simulated by SMAP with in situ measurements. To assess the performance of the model we used the correlation coefficient ( $r$ ), root mean square error ( $RMSE$ ), and mean error ( $ME$ ; the average of the difference between simulated values and observed values)



obtained from a comparison of measured and simulated data during the period from November to April for both winters (Table 2.4).

SMAP requires as input the values of some model parameters, including the number of subbands used in PBSAM,  $\Delta t$ ,  $d_{min}$ ,  $d_{max}$ , and the maximum value of  $k_{eff}$ . Except for the number of subbands, SMAP requires these parameters to solve the energy balance equations with the Crank-Nicolson finite difference implicit method (Sect. 2.2.5). To demonstrate the expected maximum potential of SMAP, we chose somewhat computationally demanding values for the number of subbands,  $\Delta t$ ,  $d_{min}$ , and  $d_{max}$ . We employed four subbands for both the UV-visible and near-infrared bands. We solved the energy balance equations with  $\Delta t = 50$  s and forced  $d$  to range between  $d_{min} = 0.005$  m and  $d_{max} = 0.03$  m. In addition we restricted  $k_{eff}$  not to exceed  $1.0 \text{ W m}^{-1}\text{K}^{-1}$  in the present study.

#### **2.4.1. Snow depth, SWE, and snow density**

In general it is possible for snowpack models to reproduce column-integrated SWE if energy and mass balance considerations are imposed precisely. To reproduce snow depth, snowpack models are required to simulate multifarious physical processes, namely snow settlement, phase changes, water percolation, and snow metamorphism accurately in addition. Thus in this section we validated snow depth, column-integrated SWE, and Column-average snow density to assess the overall performance of SMAP. Before the validation we investigated the sensitivities of three parameterizations for new snow density mentioned in Sect. 2.2.3 (*Yamaguchi et al. (2004)*, *Lehning et al. (2002b)*, and *Yamazaki (1998, 2001)*) in terms of half-hourly snow depth in order to verify the availability of the function by *Yamazaki (1998, 2001)* at Sapporo. SMAP with the function by *Yamaguchi et al. (2004)* obtained *RMSE* of 0.073 m and 0.089 m for 2007–2008 winter and 2008–2009 winter, respectively. When we employed the function by *Lehning et al. (2002b)* we obtained *RMSE* of 0.075 m and 0.080 m for 2007–2008 winter and 2008–2009 winter, respectively. Finally, we acquired *RMSE* of 0.064 m and 0.075 m for 2007–2008 winter and 2008–2009 winter, respectively if we chose the

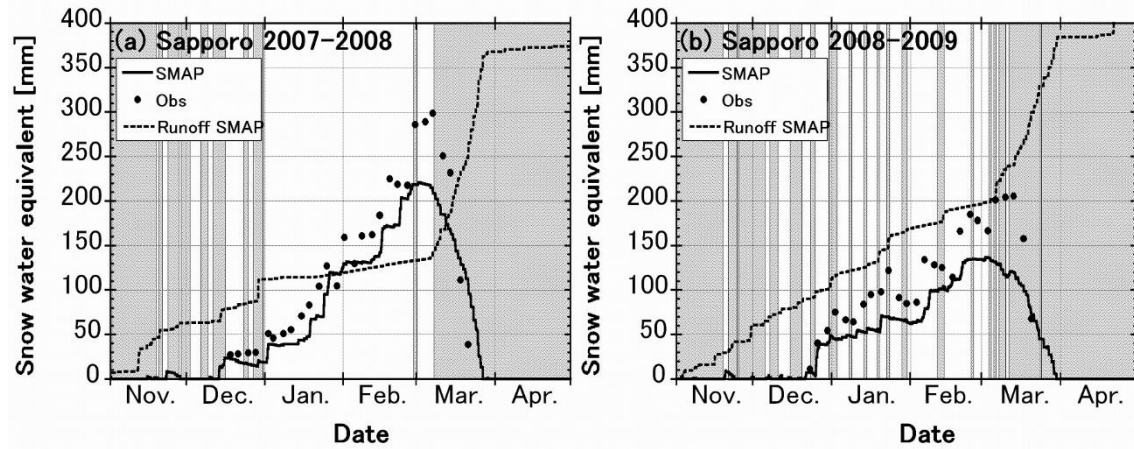


**Figure 2.3.** Column-integrated snow water equivalent (SWE) from snow pit observations (filled circles) and simulated by SMAP for every half-hour (solid curve), together with accumulated runoff at the bottom of the snowpack as simulated by SMAP (dotted curve) at Sapporo during two winters: (a) 2007–2008 and (b) 2008–2009.

parameterization by Yamazaki (1998, 2001). From these results we confirmed the usefulness of the function by Yamazaki (1998, 2001) at least in Sapporo. However, when we apply SMAP to global climate simulations, we have to investigate sensitivities and performances of these parameterizations again. Furthermore, it is necessary to develop a physically based function to calculate new snow density in the future.

We began our model validation with a comparison of half-hourly snow depths observed by AWS and simulated by SMAP. SMAP reproduced very well the seasonal variations in snow depth during both winters (Figs. 2.2c and 2.2d, Table 2.4). A comparison of *RMSE* values and *ME* values (Table 2.4) indicates that SMAP modeled snow depth with comparable accuracy during both winters and tended to somewhat overestimate observed depths. To more carefully explore the accuracy of the simulated snow depths we examined the accuracy of the modeled column-integrated SWE and Column-average snow density.

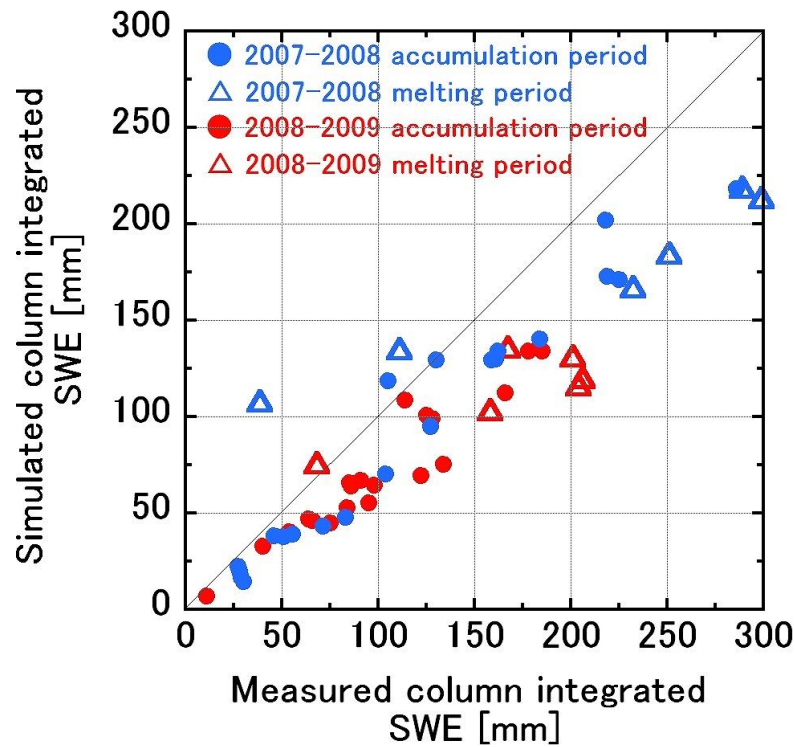


**Figure 2.4.** Comparison between column-integrated snow water equivalent (SWE) from snow pit observations and simulated by SMAP for every half-hour. Blue dots and triangles denote accumulation period and ablation period during 2007–2008 winter, respectively. Red dots and triangles denote accumulation period and ablation period during 2008–2009 winter, respectively.

A comparison of column-integrated SWE and bottom runoff simulated by SMAP with the column-integrated SWE from snow pit observations revealed that SMAP successfully reproduced seasonal variations of column-integrated SWE (Fig. 2.3), however, SMAP tended to underestimate column-integrated SWE in all periods for both winters (Fig 2.4), with the bias being more pronounced during the winter of 2008–2009 than 2007–2008 (Table 2.4). During January to February 2009, a large amount of SWE (about 100 mm) drained off from the snowpack as air temperature frequently rose above 0 °C (Fig. 2.3). However, at the end of the ablation period, the

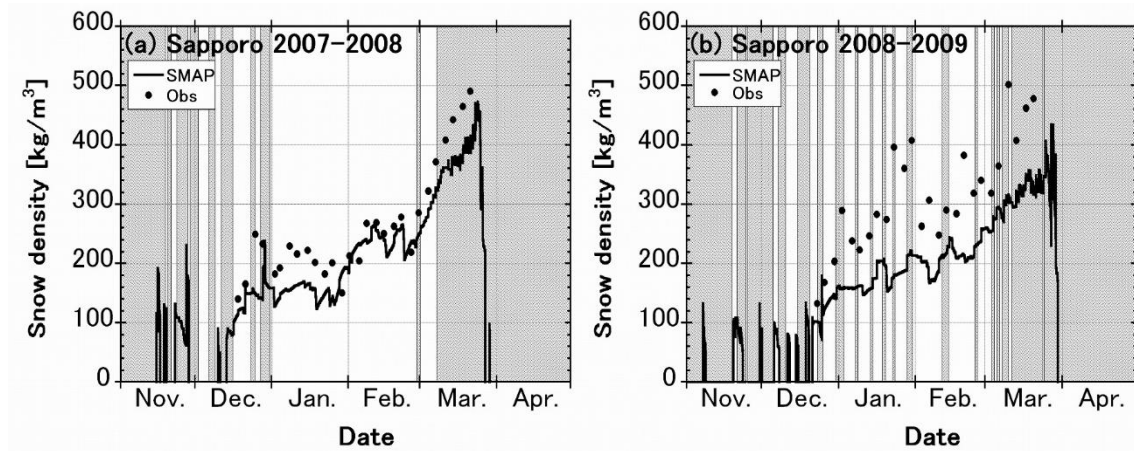


**Figure 2.5.** Column-average snow density from snow pit observations (filled circles) and simulated by SMAP for every 30 minutes (solid curve) at Sapporo during two winters: (a) 2007–2008 and (b) 2008–2009.

calculated and observed column-integrated SWEs were similar in both winters. This result suggests that modeled water movement in snowpack especially during the accumulation period can be sometimes unrealistic and inadequate. In some cases the maximum water content can be higher than the simple present setting described in Sect. 2.2.5. In order to eliminate the uncertainty in the water movement process, it will be necessary to treat the maximum water content as a function of snow microstructure as pointed out by *Bartelt and Lehning* (2002).

Since snow density is increased by overburden pressure, underestimates of SWE can result in underestimates of snow density. We checked the accuracy of the simulated Column-average snow density by comparing them with the snow pit observations (Fig. 2.5). Although SMAP reproduced seasonal variations of Column-average snow density for both winters, SMAP underestimated Column-average snow density (Fig. 2.6) and this tendency was more pronounced during warm 2008–2009 winter when air temperature were often above 0 °C even during accumulation period (Figs. 2.5, 2.6, and Table 2.4).

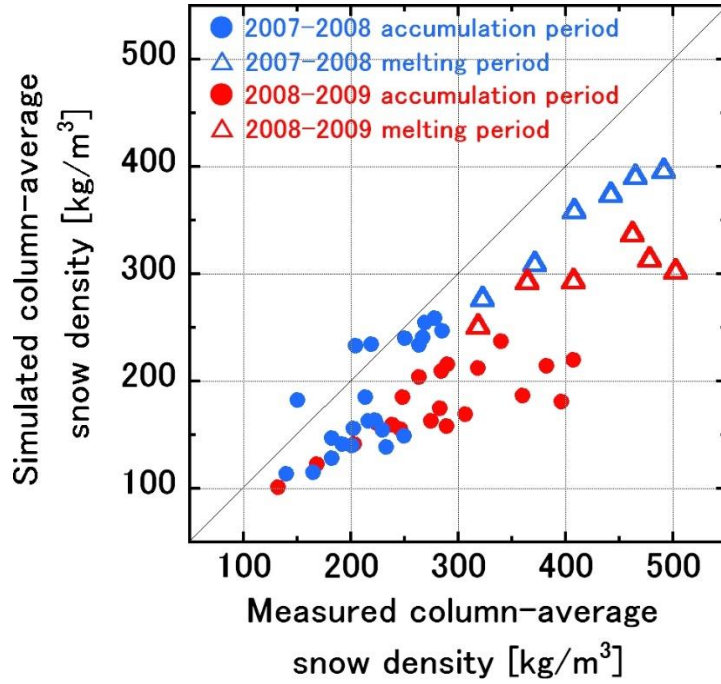


**Figure 2.6.** Comparison between Column-average snow density from snow pit observations and simulated by SMAP for every 30 minutes. Blue dots and triangles denote accumulation period and ablation period during 2007–2008 winter, respectively. Red dots and triangles denote accumulation period and ablation period during 2008–2009 winter, respectively.

Overall the simulated mass balance during the winter of 2008–2009 was not as accurate as during the winter of 2007–2008, though the accuracy of simulated snow depth was comparable during both winters. The result that larger amount of SWE drained off from the snowpack during January to February in relatively warm 2009 winter compared to 2008 winter suggest that inadequacies of the water movement simulation during accumulation period appear to be primarily responsible for the inaccuracy of the model simulations. If more SWE remains in the snowpack, snow compaction can proceed more rapidly. To improve the accuracy of the mass balance during the 2008–2009 winter, it is needed to consider realistic water percolation and retention processes.

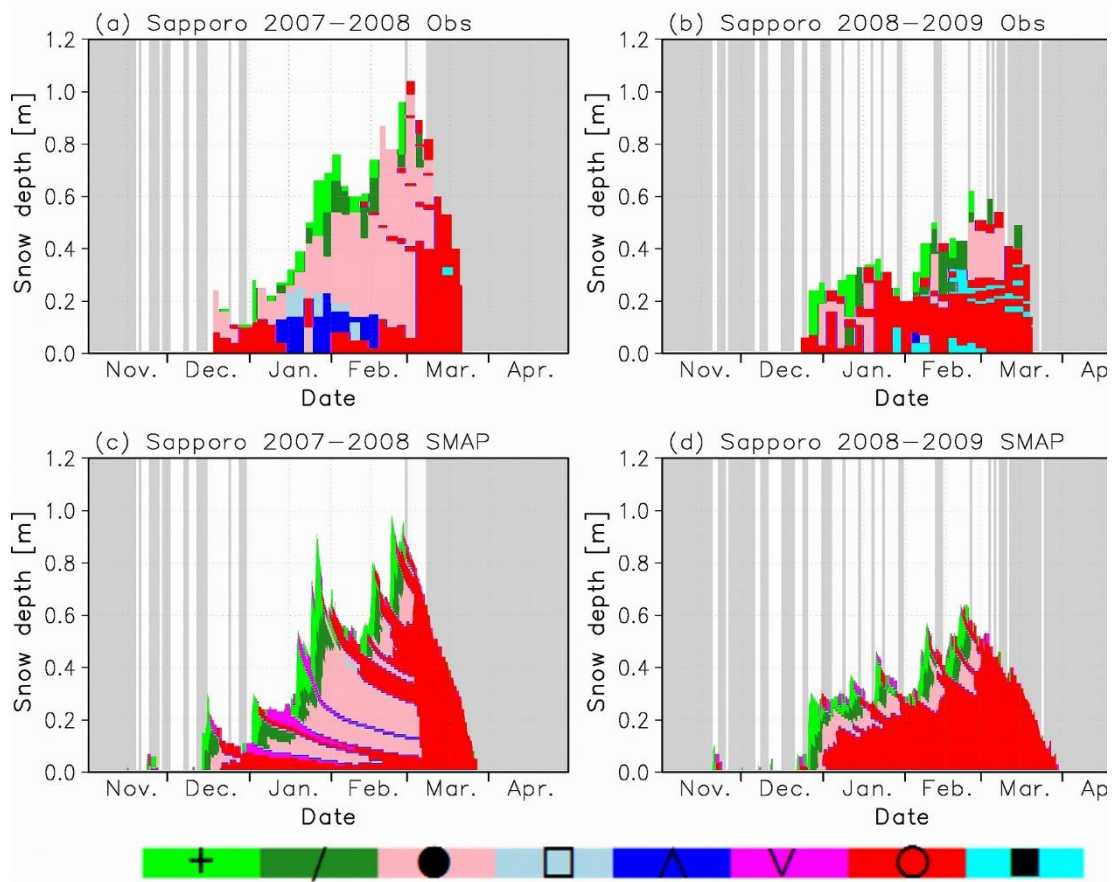


**Figure 2.7.** (a, b) Time evolution of the vertical profile of major snow grain shapes from snow pit observations and (c, d) simulated by SMAP at Sapporo during two winters: (a, c) 2007–2008 and (b, d) 2008–2009. Characters and colors indicating snow grain shapes follow the definitions by *Fierz et al.* (2009). In sequence from the left the characters and colors denote precipitation particles, decomposing and fragmented precipitation particles, rounded grains, faceted crystals, depth hoar, surface hoar, melt forms, and ice formations. Observed snow grain shapes are shown for only the days when snow pit observations were performed.

#### 2.4.2. Snow grain shape

Since air temperatures at Sapporo were often greater than 0 °C during the accumulation period (Fig. 2.2), melt forms were often observed in the snow pits. A comparison of the temporal evolution of the

vertical profiles of snow grain shape observed in the snow pits and those simulated by SMAP (Fig. 2.7) shows that SMAP successfully reproduced the overall stratigraphy for both winters. SMAP reproduced well, in particular, the temporal evolution of precipitation particles, decomposing and fragmented precipitation particles, and rounded grains. However, the fact that SMAP did not simulate depth hoar and faceted crystals observed in the lower layers during January–February 2008 indicates a need for improvement in the simulated process of temperature gradient metamorphism, which generally develops depth hoar and faceted crystals. SMAP also sometimes simulated melt forms in surplus. For example, SMAP simulated excessive melt forms in the upper layers in early February 2008. The likely cause is underestimation of snow albedo, which is discussed in section 2.4.5. Finally, SMAP could not reproduce the ice formations that we frequently observed during the warm winter of 2008–2009. To reproduce ice formations it will be necessary to improve water retention and percolation processes during accumulation period questioned in the previous section.

### **2.4.3. Snow surface temperature**

It is possible for us to assess whether energy exchanges at the snow surface were modeled adequately or not in terms of snow surface temperature. A comparison of temporal sequences of half-hourly snow surface temperature for snow-covered periods observed with AWS and those simulated by SMAP (Fig. 2.8) indicates that SMAP reproduced diurnal variations of snow surface temperature fairly well for both winters ( $r = 0.914$  for the 2007–2008 winter and  $0.913$  for the 2008–2009 winter). There were no obvious biases for either winter ( $ME = -0.301$  °C for 2007–2008 winter and  $ME = -0.666$  °C for 2008–2009 winter). However, SMAP occasionally underestimated snow surface temperatures at night when surface cooling was enhanced, for example during 7–9 March 2008. During these days the sky conditions at Sapporo were clear, and the winds were calm. The conditions at night were therefore quite stable. A possible cause of the underestimation in this case is the treatment of turbulent heat fluxes under very stable conditions when  $Ri$  exceeds the critical



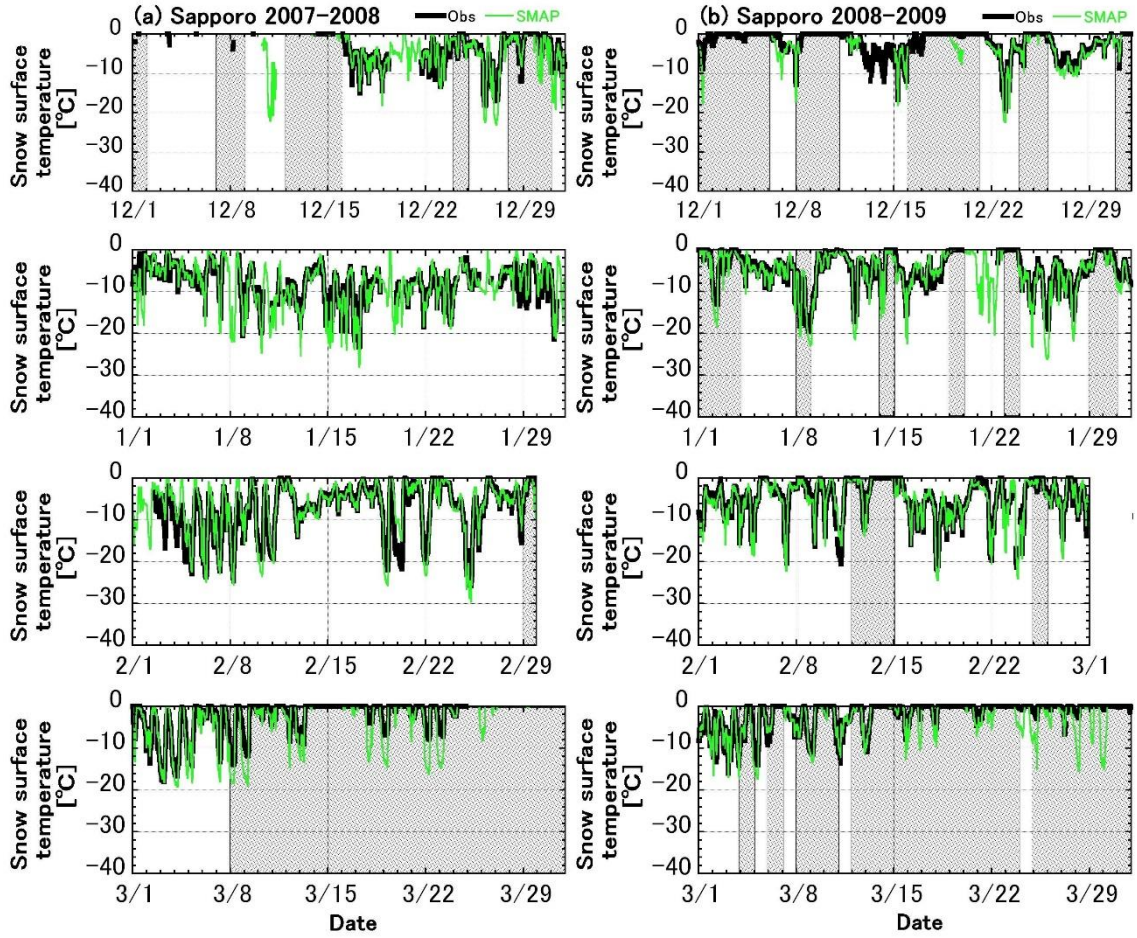


**Figure 2.8.** Half-hourly snow surface temperature observed with AWS (black solid curve) and simulated by SMAP (green solid curve) at Sapporo for December through March: (a) 2007–2008 and (b) 2008–2009.

Richardson number explained in Sect. 2.2.1. Under these conditions SMAP assumes that turbulence ceases. To improve the model performance it can be effective to introduce a windless transfer coefficient employed in SNTHERM (*Jordan, 1991; Jordan et al., 1999; Andreas et al., 2004; Helgason and Pomeroy, 2011*), or a modification formulation for bulk transfer coefficients implemented in CROCUS by *Martin and Lejeune (1998)* to ensure minimum heat exchanges even under very stable conditions. However, since they are quite empirical, they should be validated



carefully through detailed micrometeorological observations such as turbulence measurements with the eddy covariance technique before introducing them to SMAP.

Another possible cause of the underestimation of snow surface temperatures at night is an uncertainty of the effective thermal conductivity of snow. In the present formulation (see Sect. 2.2.1), the low density of snow near the surface obstructs heat transfer between the lower layers and near-surface layers. Since the effective thermal conductivity of snow depends qualitatively on the morphological state of the snowpack (Sturm et al., 1997; Schneebeli and Sokratov, 2004; Kaempfer et al., 2005), simple parameterizations of the effective thermal conductivity of snow as a function of snow density are inadequate.

#### **2.4.4. Snow grain size**

As explained in section 2.2.1, SMAP employs PBSAM, which calculates snow albedo and solar heating profiles in snowpack, with vertical profiles of snow grain size, SWE, snow impurities, and solar illumination conditions as input. In situ measurements or host GCMs provide profiles of snow impurities as external inputs, whereas SMAP calculates profiles of snow grain size and SWE internally. The snow grain size profile is one of the most important prognostic outputs of SMAP.

We first examined the effect of the implicit consideration of snow metamorphism under alternating temperature gradients described in Sect. 2.2.4 by comparing the simulated snow grain size in the top 2 cm of the snowpack with the snow grain size observed in the snow pits (Fig. 2.9). The implicit consideration remarkably improved the accuracy of the snow grain size simulations in January of both winters (Figs. 2.9a and 2.9b). By employing the implicit consideration, SMAP kept the simulated snow grain sizes during these periods to less than 0.05 mm, and the simulated values

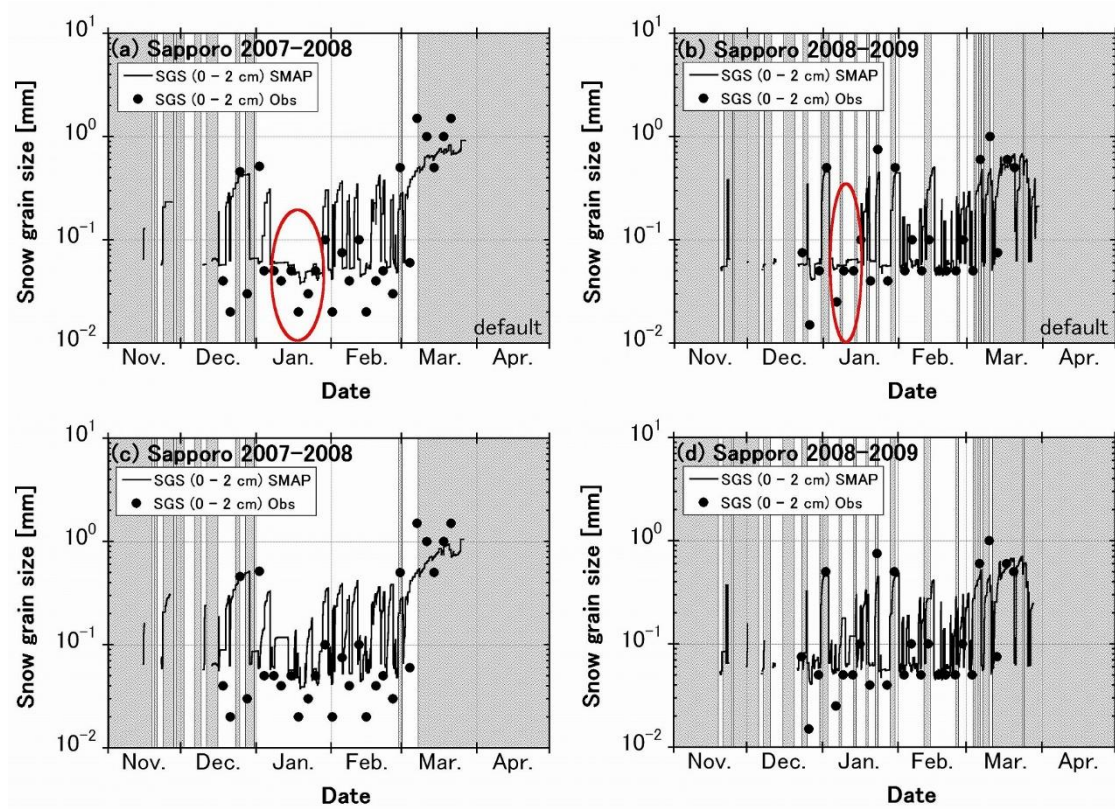


**Figure 2.9.** Snow grain size (SGS) in the top 2 cm of the snowpack from snow pit observations (filled circles) and simulated by SMAP (solid curve) at Sapporo during two winters: (a, c) 2007–2008 and (b, d) 2008–2009. Model simulations were performed (a, b) with implicit consideration of snow metamorphism under alternating temperature gradients, which forces the temperature gradient metamorphism not to occur in the top 20 cm of the snowpack, and (c, d) without the implicit consideration, which allows the temperature gradient metamorphism throughout the snowpack. The former was the default setting in the present study. Red ellipses in (a) and (b) indicate the periods when the accuracy of simulated SGS is remarkably improved by the implicit consideration.

closely approached the observed snow grain sizes. We therefore employed the implicit consideration as the default setting of SMAP. Although the implicit consideration accomplished to some degree in

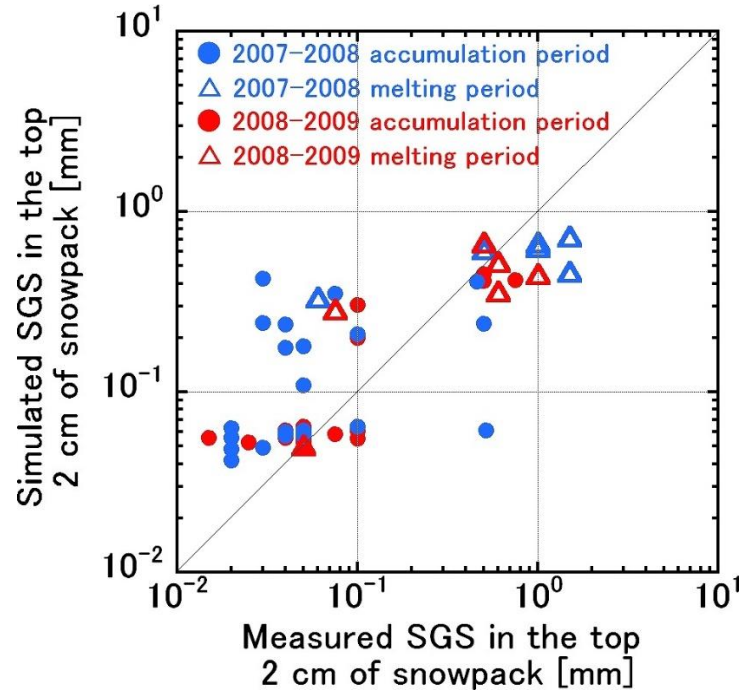


**Figure 2.10.** Comparison between Snow grain size in the top 2 cm of the snowpack from snow pit observations and simulated by SMAP with the default setting (see Fig. 2.9) at Sapporo during two winters. Blue dots and triangles denote accumulation period and ablation period during 2007–2008 winter, respectively. Red dots and triangles denote accumulation period and ablation period during 2008–2009 winter, respectively.

the present study, it goes without saying that the explicit formulations of snow metamorphism under alternating temperature gradients should be developed in the future because the implicit consideration cannot reproduce observed high mass turnover (*Pinzer and Schneebeli, 2009*) accurately.

The results with the implicit consideration (Figs. 2.9a, 2.9b) and the correlation coefficients (0.763 and 0.840 for the 2007–2008 and 2008–2009 winters, respectively) indicate that SMAP approximately reproduces the characteristics of the seasonal variation of snow grain size, i.e., small

during the accumulation period and rapidly growing during the ablation period. However, SMAP tends to overestimate observed snow grain sizes less than about 0.1 mm and to underestimate snow grain sizes during the ablation period (Fig. 2.10). A possible cause of the overestimates is errors in new snow grain size calculated by Eq. 2.27. There is a possibility that Eq. 2.27 slightly overestimates new snow grain size especially when the air temperature is negative. New snow grain size could be affected by not only air temperature but also the shape of new snow, wind speed, and relative humidity. A physically based parameterization of new snow grain size that explicitly considers those effects should be developed in the future. Finally, the underestimates during the ablation period could be related to wet snow metamorphism. The grain growth rate under wet snow metamorphism can be higher than the present formulation.

#### **2.4.5. Broadband albedos**

Snow albedo plays an important role in controlling energy exchanges between the snow surface and the atmosphere. We therefore sought to determine whether SMAP could bring out PBSAM's potential accuracy by comparing the accuracy of simulated broadband albedos estimated with SMAP to those calculated by *Aoki et al.* (2011).

We conducted the validation of broadband albedos in the same manner as *Aoki et al.* (2011) by employing only the daily half-hourly broadband albedos measured from 1130 to 1200 local time around local noon. A comparison of broadband albedos observed with AWS and simulated by SMAP (Fig. 2.11) shows that albedo variations for the three spectra were well reproduced for both winters, although some discrepancies are apparent. Broadband albedos were underestimated in early February 2008. During that period SMAP simulated excessive melt forms in the upper layers (Fig. 2.7a) and overestimated snow surface temperature (Fig. 2.8). In general, reduced shortwave albedo can induce snowmelt in the upper layers and cause snow surface temperature to approach 0°C. This cycle triggers wet snow metamorphism and in turn accelerates snow grain growth. Furthermore,

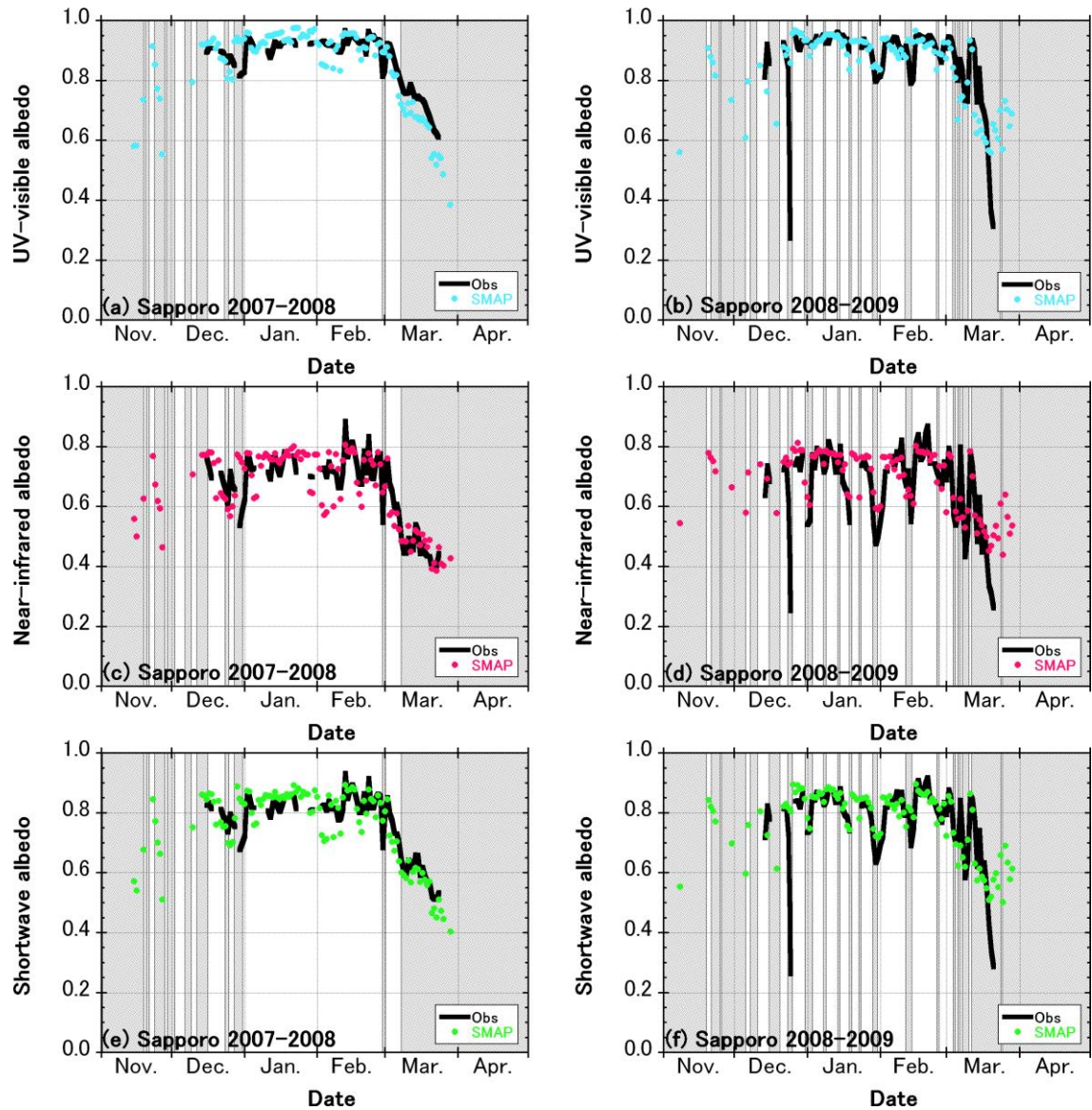


**Figure 2.11.** Daily half-hourly broadband albedos from 1130 to 1200 local time observed with AWS and those simulated by SMAP in the (a, b) UV-visible, (c, d) near-infrared, and (e, f) shortwave spectra during two winters: (a, c, e) 2007–2008 and (b, d, f) 2008–2009.

snow grain growth affects broadband albedos by reducing especially near-infrared albedo. We thus confirmed the repeated occurrence during the study period of the positive feedback between the increase in snow temperature and snow grain growth (*Colbeck, 1975; Wiscombe and Warren, 1980*).

During the 2008–2009 winter, observed broadband albedos (especially near-infrared albedos) often fluctuated rapidly in the short term. This behavior was not reproduced well by SMAP. For example, SMAP did not simulate the rapid albedo reduction observed during late December 2008. A likely cause is the failure of SMAP to simulate very shallow snow depths. In late March 2009, SMAP simulated unrealistic increases in albedo. We attribute this error to failure of the algorithm that calculates the snow:rain ratio for new snow (see Sect. 2.2.2). In contrast, we attribute the poor reproducibility of the large fluctuations that we measured from January to early March 2009 to errors in the simulation water movement processes (questioned in Sect. 2.4.1) because the processes affect profiles of water content and snow grain size. If more SWE remains in snowpack, snow grain size develops more rapidly in proportion to higher water content (*Brun et al.*, 1992; *Lehning et al.*, 2002a) and reduced the albedo can be reproduced.

*RMSE* values of the shortwave albedo obtained by SMAP were 0.051 and 0.084 for the winters of 2007–2008 and 2008–2009, respectively. We attribute the relatively large *RMSE* value for the 2008–2009 winter mainly to errors that we found during late December 2008 when SMAP failed to simulate rapid complete melting and during late March 2009 when SMAP simulated unrealistic increases in albedo. In fact the *RMSE* value of the shortwave albedo simulated by SMAP was 0.048 from 1 January 2009 to 15 March 2009. *RMSE* values of the shortwave albedo obtained by PBSAM were 0.052 and 0.042 for the winters of 2007–2008 and 2008–2009, respectively (*Aoki et al.*, 2011). These results confirm that SMAP can exploit PBSAM’s potential accuracy.

## **2.5. Effects of snow impurities on snowmelt at Sapporo**

We investigated the effects of snow impurities on snowmelt by using the data collected during the 2007–2008 and 2008–2009 winters at Sapporo. For this purpose, we carried out a “pure snow experiment” with SMAP by assuming that there were no snow impurities. A comparison of simulated snow depths for snow containing impurities (“CTL” simulation: same as Figs. 2.2c and



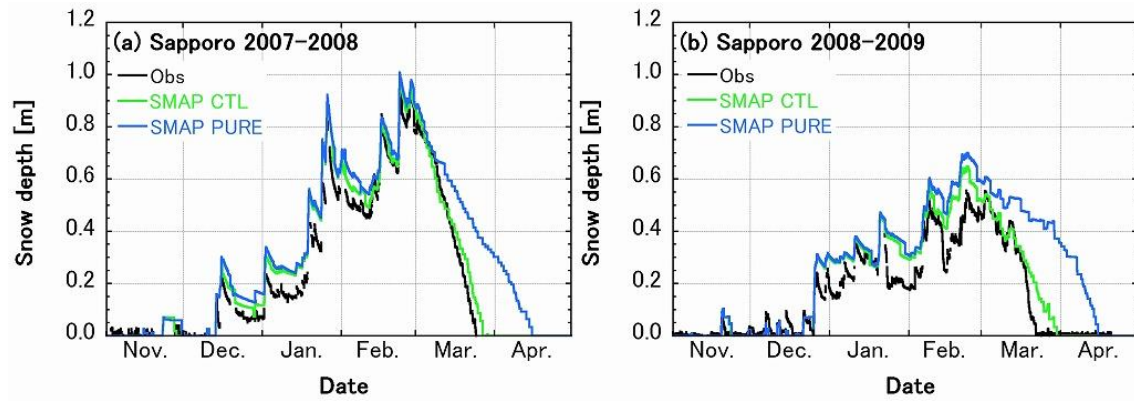


**Figure 2.12.** Simulations of half-hourly snow depths by SMAP with default settings (CTL scenario: light green solid curve) and with pure (i.e., no impurities) snow conditions (PURE scenario: blue solid curve), and the observed snow depths (black solid curve) during two winters: (a) 2007–2008 and (b) 2008–2009. Background shade indicated in other figures, which depict time series, is not shown here.

2.2d), and for snow without impurities (“PURE” simulation) (Figs. 2.12a and 2.12b, respectively) revealed a remarkable effect of snow impurities on the ablation period for both winters. The presence of impurities caused the duration of the snowpack to be shortened by 19 days and 16 days in the first and second winters, respectively.

To qualitatively assess the effects of snow impurities we estimated the surface radiative forcing (Hansen and Nazarenko, 2004) of snow impurities by calculating the difference between the PURE and CTL simulated shortwave radiant fluxes absorbed by the snowpack. Averaged over the entire period of snow cover, the simulated radiative forcings due to snow impurities were  $9.0 \text{ W m}^{-2}$  and  $8.1 \text{ W m}^{-2}$  for the 2007–2008 and 2008–2009 winters, respectively. The contrast of the simulated radiative forcing between accumulation periods and ablation periods was remarkable. The estimated radiative forcings of snow impurities averaged during only the accumulation periods were  $3.7 \text{ W m}^{-2}$  and  $3.2 \text{ W m}^{-2}$  for the 2007–2008 and 2008–2009 winters, respectively. These values correspond to

0.05 reductions in shortwave albedo due to snow impurities for both the 2007–2008 and 2008–2009 winters. In contrast, the estimated radiative forcings of snow impurities averaged during only the ablation periods were  $25.9 \text{ W m}^{-2}$  and  $21.0 \text{ W m}^{-2}$  for the 2007–2008 and 2008–2009 winters, respectively. These values correspond to 0.18 and 0.17 reductions in shortwave albedo due to snow impurities for the 2007–2008 and 2008–2009 winters, respectively. *Aoki et al.* (2011) indicated seasonal variations of mass concentrations of snow impurities at Sapporo during two winters: 2007–2008 and 2008–2009, which are also used in this study as input parameters for SMAP. The variations show that mass concentrations of snow impurities during accumulation period are not significantly low compared to those during ablation period. Therefore, the contrast of the simulated radiative forcing between accumulation periods and ablation periods can be attributed to (1) the contrast of downward shortwave radiant flux; and (2) the difference in snow grain size. As for (1) downward shortwave radiant flux is much higher during spring ablations periods compared to winter accumulation periods. Regarding (2) snow grain size during ablation periods develops rapidly through wet snow metamorphism, while it is relatively low during accumulation periods as demonstrated in Figs 2.9a and 2.9b. In general, radiation penetrates deeper in more coarsely grained snow and encounters more absorbing materials before it can reemerge from the snowpack (e.g., *Warren and Wiscombe*, 1980; *Aoki et al.*, 2011), and these result in lower broadband albedo and enhanced solar heating in snowpack.

## 2.6. Summary and conclusions

Snow albedo plays an important role in terrestrial climate systems. Recently, several authors have developed physically based snow albedo models for GCMs to improve the accuracy of climate simulations (*Flanner and Zender*, 2005; *Flanner et al.*, 2007; *Gardner and Sharp*, 2010; *Yasunari et al.*, 2011; *Aoki et al.*, 2011). As these models require either snow grain size or SSA as an input parameter, GCMs should calculate these parameters accurately. In general, temporal changes in



snow grain size or SSA depend on snow metamorphism processes, which are controlled by physical states of snowpack such as snow temperature and water content. Hence an optimum snowpack model for LSMs, which reproduces realistic physical states of snowpack, is necessary to utilize these snow albedo models and to bring out their potential accuracy in climate simulations.

In the present study we developed a multilayered physical snowpack model named SMAP, which incorporates PBSAM (Aoki *et al.*, 2011) and is able to bring out PBSAM's potential accuracy with respect to snow albedo simulation. SMAP takes energy balance, mass balance, snow settlement, phase changes, water percolation, and snow metamorphism into account. The PBSAM component of SMAP calculates snow albedo and solar heating profiles by using profiles of snow grain size and SWE calculated by SMAP, together with mass concentrations of snow impurities externally provided by in situ measurements or host GCMs. Snow grain size is calculated with the use of a model geometry that envisions two spherical ice particles connected by a neck (Lehning *et al.*, 2002a). SMAP obtains snow grain sizes by calculating SSA per unit volume with the nonspherical model geometry. SMAP calculates the temporal evolution of snow grain size with the same formulations as SNOWPACK (Lehning *et al.*, 2002a), which take into consideration equi-temperature metamorphism, temperature gradient metamorphism, and wet snow metamorphism. SMAP also implicitly considers the effects of snow metamorphism under alternating temperature gradients (Pinzer and Schneebeli, 2009) by forcing the temperature gradient metamorphism not to occur in the top 20 cm of the model layers, although this method cannot reproduce observed high mass turnover accurately. SMAP is now implemented into the Meteorological Research Institute Earth System Model version1 (MRI-ESM1) (Yukimoto *et al.*, 2011) through the integrated land surface framework named Hydrology, Atmosphere, and Land surface (HAL) (Hosaka *et al.*, manuscript in preparation, 2012), which provides input data for SMAP. However, we restrict the number of model snow layers by eight at present due to high computational costs of SMAP.

We evaluated SMAP with meteorological and snow data observed during two winters from 2007 to 2009 at Sapporo, Japan. We compared the simulated snow depth, column-integrated SWE, Column-average snow density, snow grain shape profile, snow surface temperature, grain size in the top 2 cm of the snowpack, and broadband albedos with in-situ measurements. SMAP reproduced well all observed seasonal variations of these parameters for both winters. *RMSE* values of shortwave albedo obtained by SMAP were 0.051 and 0.084 for the 2007–2008 and 2008–2009 winters, respectively. The *RMSE* value for the 2007–2008 winter is comparable to that obtained by PBSAM (0.052) (Aoki *et al.*, 2011). Although the *RMSE* for the 2008–2009 winter is somewhat large compared to that obtained by PBSAM (0.042) (Aoki *et al.*, 2011), we attribute the discrepancy mainly to errors found during late December 2008, when SMAP failed to simulate rapid complete melting, and during late March 2009, when SMAP simulated unrealistic increases in albedo. Except for these periods (i.e., from 1 January 2009 to 15 March 2009, during which time the simulated snowpack existed continuously), SMAP obtained an *RMSE* value of 0.048. These results confirm that SMAP is able to bring out the potential accuracy of PBSAM and can be served for climate simulations by GCMs.

Finally, we investigated the effects of snow impurities on snowmelt at Sapporo during the 2007–2008 and 2008–2009 winters with a sensitivity test in which we assumed an absence of snow impurities. Snow depths simulated by the sensitivity test indicated that snow impurities forced snowpack durations at Sapporo to be shortened by 19 days and 16 days during the 2007–2008 and 2008–2009 winters, respectively. Most of the changes occurred during the ablation period. The estimated surface radiative forcings of snow impurities were quite low during ablation periods (around  $3.5 \text{ W m}^{-2}$ ) compared to accumulation periods ( $25.9 \text{ W m}^{-2}$  for 2007–2008 and  $21.0 \text{ W m}^{-2}$  for 2008–2009) for both winters. These radiative forcings were consequences of reductions in shortwave albedo by around 0.05 during accumulation periods, while around 0.175 during ablation

periods. The seasonal contrast was attributed to (1) the contrast of downward shortwave radiant flux; and (2) the difference in snow grain size between accumulation and ablation periods. Above mentioned results highlight the fact that GCMs, which incorporate detailed snow albedo models that calculate snow albedo explicitly, need to calculate mass concentrations of snow impurities accurately. For that purpose it is necessary for aerosol transport models implemented into GCMs to simulate aerosol depositions onto the snow surface accurately. In addition, we have to develop a formulation for movements of impurities in snowpack, which were not considered in this study.

### **Acknowledgements**

We are grateful to Michael Lehning at WSL Institute for Snow and Avalanche Research SLF, for providing us with the SNOWPACK model, from which we learned the essence of snow metamorphism processes. We thank Teppei J. Yasunari, Yuki Sawada, Kou Shimoyama, Tetsuo Sueyoshi, Junko Mori, Masahiro Takahashi, Tomoyasu Kuno, Hayato Oka, Taro Nakai, Kazuhiro Okuzawa, Tsutomu Watanabe, Shun Tsutaki, Chusei Fujiwara, Kohei Ohtomo, Niyi Sunmonu, Masaki Okuda, Tatsuya Nakayama, Hirokazu Hirano, and Etsuko Tanaka for help with snow pit observations during two winters at the Institute of Low Temperature Science of Hokkaido University. We also thank Masae Igosaki for performing the laboratory measurements of snow impurities. We gratefully appreciate the very helpful comments by Ruzica Dadic and an anonymous reviewer. This study was supported in part by (1) the Experimental Research Fund for Global Environment Conservation, the Ministry of the Environment of Japan, (2) the Grant for Joint Research Program, the Institute of Low Temperature Science, Hokkaido University, (3) the Global Change Observation Mission – Climate (GCOM–C) / the Second–generation GLObal Imager (SGLI) Mission, the Japan Aerospace Exploration Agency (JAXA), and (4) Japan Society for the Promotion of Science (JSPS), Grant-in-Aid for Scientific Research (S), number 23221004.



### 3. Attempts of advanced numerical snow modeling

Published in *Bulletin of Glaciological Research*, **32**, 65-78, doi:10.5331/bgr.32.65, 2014, entitled as

“Evaluation of updated physical snowpack model SMAP”.

**M. Niwano<sup>1</sup>, T. Aoki<sup>1</sup>, K. Kuchiki<sup>1</sup>, M. Hosaka<sup>1</sup>, Y. Kodama<sup>2</sup>, S. Yamaguchi<sup>3</sup>, H. Motoyoshi<sup>3</sup>, and Y. Iwata<sup>4</sup>**

<sup>1</sup> Meteorological Research Institute, Japan Meteorological Agency

<sup>2</sup> National Institute of Polar Research, Tachikawa

<sup>3</sup> Snow and Ice Research Center, National Research Institute for Earth Science and Disaster Prevention

<sup>4</sup> National Institute for Rural Engineering

#### 3.1. Introduction

A physical snowpack model is a useful tool as it can be employed for a wide range of scientific purposes, including studies on snow physical process, avalanche forecasting and providing boundary conditions for atmospheric general circulation models (GCMs) and regional climate models (RCMs) (Armstrong and Brun, 2008). Among the existing snowpack models, Crocus (Brun *et al.*, 1989, 1992; Vionnet *et al.*, 2012) and SNOWPACK (Bartelt and Lehning, 2002; Lehning *et al.*, 2002a, 2002b), which consider most snow physical processes utilizing multilayered model snow layers, are known to be the most extensive. The most outstanding feature of these two models is that they explicitly take into account the three representative snow metamorphism processes: (1) equilibrium temperature metamorphism, (2) temperature gradient metamorphism and (3) wet snow metamorphism. Crocus and SNOWPACK simulate internal snow physical states and energy exchanges between the snow surface and the atmosphere as a function of these metamorphic regimes. Furthermore, they have been successfully applied to various climate regimes around the world, implying that they are physically highly reliable. Indeed, Crocus has been employed in the French Alps (e.g., Rousselot *et al.*, 2010; Morin *et al.*, 2013); the mountainous region of northern

Hokkaido, Japan (*Hachikubo*, 2001); a tropical mountain environment in Ecuador (*Wagnon et al.*, 2009); an Arctic site near Fairbanks, Alaska, USA (*Jacobi et al.*, 2010); and Dome C, Antarctica (*Brun et al.*, 2011). Meanwhile, SNOWPACK has been applied in the Swiss Alps (e.g., *Fierz and Lehning*, 2001; *Lehning et al.*, 2002b); a mountainous region near Bozeman, Montana, USA (*Lundy et al.*, 2001); Finland (*Rasmus et al.*, 2004); interior Alaska, USA (*Saito et al.*, 2012); Nagaoka and Shinjyo in wet snow region of Japan (*Yamaguchi et al.*, 2004; *Saito et al.*, 2012); Sapporo, Kitami and Niseko in Hokkaido, Japan (*Hirashima et al.*, 2004; *Nishimura et al.*, 2005); and Dome C, Antarctica (*Groot Zwaaftink et al.*, 2013).

Recently, *Niwano et al.* (2012) developed a multilayered physical snowpack model called Snow Metamorphism and Albedo Process (SMAP) to serve for studies on snow physical processes, as well as climate simulations with GCMs or RCMs. SMAP is equipped with a state-of-the-art physically based snow albedo model (PBSAM) (*Aoki et al.*, 2011), which calculates snow albedo and solar heating profile in the snowpack by explicitly considering its physical characteristics: the near-infrared albedo is strongly affected by snow grain size (*Wiscombe and Warren*, 1980), while the visible albedo depends on snow impurities such as black carbon (BC) and dust (*Warren and Wiscombe*, 1980). *Niwano et al.* (2012) performed detailed validations of SMAP in terms of snow depth, column-integrated snow water equivalent (SWE), column-average snow density, snow grain shape profile, snow surface temperature, (optically equivalent) snow grain size defined by *Aoki et al.* (2007) in the top 2 cm of the snowpack and broadband albedos using the data obtained at Sapporo, Japan, during the 2007–2009 winters. Consequently, it was demonstrated that SMAP successfully reproduced all the observed variations of the physical properties of the snowpack for both winters. However, several inadequacies were revealed: (1) overestimation of snow depth, especially during the warm 2008–2009 winter when air temperatures were often above 0 °C, even in the accumulation period and (2) underestimation of snow surface temperature especially under very stable conditions.

In this study, we attempted to perform model improvements to overcome the problems mentioned above. Specifically, we introduced physically realistic schemes for water movement in the snowpack and snow settlement to improve snow depth simulations and examined the treatment of turbulent heat exchanges under very stable conditions to inhibit underestimation of snow surface temperature. The effects of these model updates were inspected using the same data as *Niwano et al.* (2012) used, which were obtained at Sapporo, Japan during the 2007–2008 and 2008–2009 winters (November to April). Next, the updated version of SMAP (hereafter, referred to as “new\_ctl”) as well as old version of SMAP (hereafter, called as “old\_ctl”) were applied to Nagaoka, Japan, which is located in one of the heaviest snow-fall regions in Japan. Because heat flux at the ground surface (ground heat flux), which is suitable for the bottom boundary condition of numerical simulations with the energy conservation equation of the snowpack, was not measured at Nagaoka during the period of interest, we introduced a soil submodel into SMAP to provide the boundary condition of the snowpack, described in Sect. 3.2.3.4. The purpose of performing model evaluations under several different climate conditions is to test the reliability of SMAP.

## **3.2. Materials and methods**

### **3.2.1. Field measurements**

#### **3.2.1.1. 2007–2009 Winters at Sapporo, Japan**

During the 2007–2009 winters, we carried out meteorological measurements using an automated weather station (AWS) installed at the Institute of Low Temperature Science, Hokkaido University (43°05'N, 141°21'E, 15 m a.s.l), which is located in an urban area within Sapporo city, Hokkaido, Japan (*Aoki et al.*, 2006). In addition, we performed snow pit measurements and snow sampling twice a week at approximately 1100 local time near the AWS. The observed parameters used to drive SMAP were the same as those used by *Niwano et al.* (2012), which are precipitation corrected by considering catch efficiencies for snow and rain as functions of gauge type and wind speed employing algorithms

by *Yokoyama et al.* (2003), air pressure, wind speed, air temperature, relative humidity, downward shortwave (wavelength  $\lambda = 0.305\text{--}2.8\ \mu\text{m}$ ) and near-infrared ( $\lambda = 0.708\text{--}2.8\ \mu\text{m}$ ) radiant fluxes, diffuse components of shortwave and near-infrared radiant fluxes, downward longwave radiant flux, ground heat flux, column-integrated SWE and mass concentrations of snow impurities (BC and dust) for the top 2 and 10 cm snow layers obtained from collected snow samples (*Kuchiki et al.*, 2009; *Aoki et al.*, 2011). Because the downward ultraviolet (UV)-visible radiant flux was not measured directly, it was calculated by subtracting the measured downward near-infrared radiant flux from the measured downward shortwave radiant flux. For meteorological input data we used data averaged every 30 min. The procedure to input mass concentrations of snow impurities into SMAP was the same as used by *Niwano et al.* (2012), where the values in the top 2 cm layers of the model snowpack were equated to the corresponding observed values, while for the lower layers of the model snowpack, the observed values for the top 10 cm of the snowpack were used. The data gaps of mass concentrations of snow impurities for the days between snow pit observations were filled using the values measured at the preceding points in time (*Niwano et al.*, 2012). For model evaluation, we used snow depth and snow surface temperature measured with the AWS and column-integrated SWE from snow pit measurements. In the following sections, we refer to November, December, January and February as the “accumulation period” and March and April as the “ablation period.”

#### **3.2.1.2. 2011–2012 Winter at Nagaoka, Japan**

Nagaoka is located in one of the heaviest snow-fall regions in Japan and the dominant snow grain shape is melt forms, because of the continuous formation and percolation of melt water throughout the entire winter period (*Yamaguchi et al.*, 2004). Therefore, it is worth testing the performance of SMAP developed and evaluated with the data measured at Sapporo, where dry snow is predominant during the accumulation period (*Niwano et al.*, 2012). In the present study, we employed meteorological data measured with an AWS installed in the observation field of the Snow and Ice Research Center,



National Research Institute for Earth Science and Disaster Prevention (NIED), located in Nagaoka city, Niigata, Japan, (37°25'N, 138°53'E, 97 m a.s.l) during the 2011–2012 winter; we also used snow pit measurements conducted once a week (*National Research Institute for Earth Science and Disaster Prevention, Japan, 2012*). The observed forcing parameters for SMAP model simulations at Nagaoka are hourly precipitation, air pressure, wind speed, air temperature, relative humidity, downward shortwave and near-infrared radiant fluxes and downward longwave radiant flux. Again, the downward UV-visible radiant flux was calculated from measured downward shortwave and near-infrared radiant fluxes in the same manner as for Sapporo (Sect. 3.2.1.1.). At Nagaoka, we did not measure diffuse fractions of UV-visible and near-infrared radiant fluxes. Therefore, they were simulated by SMAP using the scheme of *Goudriaan (1977)* as functions of internally calculated cloud fraction (*Niwano et al., 2012*) and solar zenith angle. Uncertainties in SMAP model simulations caused by this calculation process are assessed using the data obtained at Sapporo in Sect. 3.3.1. For the precipitation data, we corrected the measured precipitation by calculating catch efficiencies for snow and rain as functions of gauge type and wind speed using algorithms developed by *Yokoyama et al. (2003)*, as performed for the case at Sapporo by *Niwano et al. (2012)*. Because ground heat flux was not available at Nagaoka, we performed coupled simulations between the snowpack and the underlying soil using a newly developed soil submodel for SMAP introduced in Sect. 3.2.3.4. To initialize the soil physical states, the observed soil temperatures (at 10, 20, 50, 80, 100 and 150 cm in depths) were utilized. In addition, we performed snow sampling at several different times to acquire the mass concentration of snow impurities in the top 0–2 cm and 0–10 cm layers during the winter in the same manner as that for Sapporo, allowing us to input them into SMAP in a similar way to that employed at Sapporo. For performing the model evaluation at Nagaoka, we employed snow depth, column-integrated SWE, soil temperature and snow surface temperature measured with the AWS. We also introduced column-average snow density calculated from observed snow depth and column-

integrated SWE. The snow surface temperature was obtained from the observed downward and upward longwave radiant fluxes assuming the emissivity of the snow surface to be 0.98 (*Armstrong and Brun*, 2008). In addition to volumetric water content profiles obtained from snow density and water weight content measured with a dielectric probe (*Denoth*, 1994), regular snow pit measurements were used.

### **3.2.2. SMAP model overview**

Using the input parameters listed in Sect. 3.2.1., the 1D physical snowpack model SMAP calculates the temporal evolution of the physical characteristics of snow by considering energy balance, mass balance, snow settlement, phase changes, water percolation and snow metamorphism. Here precipitation included in the input parameters are partitioned into snow and rain by using the algorithm to calculate snow:rain ratios as a function of wet bulb temperature introduced by *Yamazaki* (1998, 2001).

The PBSAM component of SMAP calculates snow albedo and solar heating profiles by using profiles of snow grain size and SWE internally calculated by SMAP, together with the mass concentrations of snow impurities externally provided by *in situ* measurements or host GCMs or RCMs. Snow grain size is calculated using a model geometry that envisions two spherical ice particles connected by a neck (*Lehning et al.*, 2002a). SMAP obtains snow grain sizes by calculating the specific surface area (SSA) of snow per unit volume with the nonspherical model geometry. SMAP calculates the temporal evolution of snow grain size using the same formulations as SNOWPACK (*Lehning et al.*, 2002a), which takes equi-temperature metamorphism, temperature gradient metamorphism and wet snow metamorphism into consideration. Furthermore, SMAP implicitly considers the effects of snow metamorphism under alternating temperature gradients (*Pinzer and Schneebeli*, 2009) by forcing temperature gradient metamorphism not to occur in the top 20 cm of the model layers.

To calculate temporal evolution of physical states of snowpack, SMAP approximates and solves the

1D energy balance equation with the Crank-Nicolson finite difference implicit method where Neumann boundary conditions, which is prescribed in terms of snow temperature gradients at both the snow surface and the bottom of the snowpack, are imposed (Niwano *et al.*, 2012). Here SMAP assumes each model snow layer to have a thickness  $d$  that is allowed to range between  $d_{\min}$  and  $d_{\max}$  (values set in this study are explained in Sect. 3.2.4.). When new snow falls or surface hoar forms, SMAP adds a new snow layer to the top of the snowpack.

### 3.2.3. Model updates

#### 3.2.3.1. Water movement in the snowpack

In the original version of SMAP (Niwano *et al.*, 2012) (old\_ctl), water percolation was controlled by means of the mass fraction of water, where liquid water fraction greater than the prescribed maximum mass fraction of water is assumed to descend to the adjacent lower layer. Niwano *et al.* (2012) pointed out that this simple treatment of water movement in the snowpack could sometimes be unrealistic and inadequate, especially during the accumulation period, leading to errors in mass balance simulations. Therefore, to improve water movement processes in the snowpack, we have incorporated the Richards equation (Richards, 1931), which considers Darcy's law:

$$\frac{\partial \theta}{\partial t} = \frac{\partial}{\partial z} \left( D \frac{\partial \theta}{\partial z} - K \right), \quad (3.1)$$

where  $\theta$  is volumetric water content,  $t$  is time,  $D$  is hydraulic diffusivity and  $K$  is hydraulic conductivity. The formulations for  $D$  and  $K$  are taken from the van Genuchten model (van Genuchten, 1980) as follows:

$$K = K_s \theta^{1/2} \left[ 1 - (1 - \theta^{1/m})^m \right]^2, \quad (3.2)$$

$$D = \frac{(1-m)K_s}{\alpha m(\theta_s - \theta_r)} \theta^{1/2-1/m} \left[ (1 - \theta^{1/m})^{-m} + (1 - \theta^{1/m})^m - 2 \right], \quad (3.3)$$

$$m = 1 - \frac{1}{n}, \quad (3.4)$$

and

$$\theta = \left( \frac{\theta - \theta_r}{\theta_s - \theta_r} \right), \quad (3.5)$$

where  $K_s$  is the saturated hydraulic conductivity,  $\theta$  is the effective water saturation,  $\theta_s$  is the volumetric water content when liquid water has filled the available snow pore space,  $\theta_r$  is the irreducible water saturation (it indicates the volumetric content of water permanently retained by capillary forces) and  $\alpha$ ,  $m$  and  $n$  are model parameters. To obtain  $K_s$ ,  $\alpha$  and  $n$ , we adopted following formulations by *Shimizu* (1970), *Hirashima et al.* (2010), *Yamaguchi et al.* (2010) and *Yamaguchi et al.* (2012) developed from laboratory experiments:

$$K_s = 7.7 \times 10^{-4} (2r_g)^2 \frac{g}{v} \exp(-7.8 \times 10^{-3} \rho_s), \quad (3.6)$$

$$\alpha = 4.4 \times 10^6 \left( \frac{\rho_{s,dry}}{2 \times 10^{-3} r_g} \right)^{-0.98}, \quad (3.7)$$

and

$$n = 1 + 2.7 \times 10^{-3} \left( \frac{\rho_{s,dry}}{2 \times 10^{-3} r_g} \right)^{0.61}, \quad (3.8)$$

where  $r_g$  (mm) is geometrical snow grain size,  $g$  is the gravitational constant,  $\nu$  is the kinetic viscosity coefficient of water at 0 °C,  $\rho_s$  is snow density (kg m<sup>-3</sup>) and  $\rho_{s,dry}$  is dry snow density (kg m<sup>-3</sup>). The other snow physical parameters of  $\theta_s$  and  $\theta_r$  were set to be 90% of the porosity and 0.02, respectively, as given by *Yamaguchi et al.* (2012). In SMAP, snow grain size is defined as the optically equivalent snow grain size, which is generally smaller than the geometrical snow grain size. Although SMAP diagnoses geometrical snow grain size from optically equivalent snow grain size at every time step (*Niwano et al.*, 2012), it is still smaller than observations. Therefore, we multiplied the geometrical snow grain size by a factor calculated from a ratio between the geometrical new snow grain size set in SNOWPACK (*Lehning et al.*, 2002a) (0.15 mm) and SMAP calculated geometrical new snow grain size to obtain  $r_g$ . The Richards equation (Eq. 3.1) is numerically solved by the finite difference implicit method to obtain the time evolution of the volumetric water content profile.

### 3.2.3.2. Snow settlement

Although the SMAP old\_ctl could reproduce seasonal variations of column-average snow density for the 2007–2008 and 2008–2009 winters at Sapporo, it turned out that SMAP old\_ctl was prone to underestimate the column-average snow density, and that this tendency was more pronounced during the warm 2008–2009 winter when air temperature were often above 0 °C, even during accumulation period, and the snowpack was often subject to wet snow conditions (*Niwano et al.*, 2012). This error caused the failure of snow depth simulations. Thus, to solve the densification equation incorporated in SMAP, we employed a detailed scheme for the viscosity coefficient of snow  $\eta$  developed to improve the performance of Crocus by *Vionnet et al.* (2012), instead of the original relatively simple scheme developed by *Bader and Weilenmann* (1992) and *Morris et al.* (1997). The new scheme incorporates the effects of snow density, snow temperature, absolute liquid water content and geometric snow grain

size on the snow settlement as follows:

$$\eta = f_1 f_2 \eta_0 \frac{\rho_s}{c_\eta} \exp(a_\eta (T_{fus} - T_s) + b_\eta \rho_s), \quad (3.9)$$

where  $\eta_0 = 7.62237 \times 10^6 \text{ kg s}^{-1} \text{ m}^{-1}$ ,  $a_\eta = 0.1 \text{ K}^{-1}$ ,  $b_\eta = 0.023 \text{ m}^3 \text{ kg}^{-1}$ ,  $c_\eta = 250 \text{ kg m}^{-3}$ ,  $T_{fus}$  is the temperature of the water melting point,  $T_s$  is the snow temperature and  $f_1$  and  $f_2$  are defined as:

$$f_1 = \frac{1}{1 + 60 \frac{W_{liq}}{\rho_w d}}, \quad (3.10)$$

and

$$f_2 = \min[4.0, \exp(\min(g_1, 2r_g - g_2)/g_3)], \quad (3.11)$$

where  $W_{liq}$  is the absolute water content in each model layer ( $\text{kg m}^{-2}$ ),  $\rho_w$  is the density of water,  $d$  is the model layer thickness,  $g_1 = 0.4 \text{ mm}$ ,  $g_2 = 0.2 \text{ mm}$  and  $g_3 = 0.1 \text{ mm}$ .

### 3.2.3.3. Turbulent heat exchanges under very stable conditions

Accurate simulation of the night time snow surface temperature under calm and clear sky conditions is a challenging topic for any snowpack model, as sensible heat flux  $H_S$  calculated by bulk method tends to be underestimated under these stable atmospheric conditions (e.g., *Martin and Lejeune*, 1998; *Helgason and Pomeroy*, 2012; *Niwano et al.*, 2012). *Niwano et al.* (2012) pointed out that a possible reason for the underestimation for SMAP is the calculation procedure of the turbulent heat fluxes, including  $H_S$  and the latent heat flux  $H_L$ , calculated by the bulk method, in which  $H_S$  and  $H_L$  were set to be 0 when the bulk Richardson number exceeded the critical Richardson number (in *Niwano et al.*

(2012) 0.25 was selected). Thus, in SMAP new\_ctl, we set a limitation for the bulk Richardson number (i.e., a maximum Richardson number) to ensure minimum turbulent exchanges, even under very stable conditions, and bind the maximum Richardson number to 0.1 following *Brun et al.* (2011).

#### 3.2.3.4. Soil submodel

It is useful to employ observed ground heat flux as the boundary condition of snow temperature evolution simulations (the Neumann boundary condition) (e.g., *Niwano et al.*, 2012). When the ground heat flux is not available, constant bottom snow temperature of 0 °C (the Dirichlet boundary condition) or constant ground heat flux are often assumed. However, these simple assumptions could lead to errors in snow-melt simulations, because heating from the ground to the snowpack cannot be assessed realistically with either of these assumptions. On the basis of this consideration, we developed a soil submodel for SMAP to provide the realistic ground heat flux into the snowpack at Nagaoka, for which the measurements of ground heat flux were unavailable during the 2011–2012 winter. In this section, the formulations of the soil submodel are described briefly.

The 1D governing equation of the soil submodel is the energy conservation equation that considers phase changes and convection flow (e.g., *Jansson and Karlberg*, 2001):

$$c_g \frac{\partial T}{\partial t} = \frac{\partial}{\partial z} \left( k_g \frac{\partial T}{\partial z} \right) + L_f \rho_w \frac{\partial \theta_i}{\partial t} - c_w T \frac{\partial q_w}{\partial z} - L_v \frac{\partial q_v}{\partial z}, \quad (3.12)$$

where  $c_g$  is the heat capacity of soil,  $T$  is the soil temperature,  $k_g$  is the thermal conductivity of soil,  $L_f$  is the latent heat of fusion,  $\theta_i$  is the volumetric ice content,  $c_w$  is the heat capacity of water,  $q_w$  is water flux,  $L_v$  is the latent heat of evaporation and  $q_v$  is vapor flux. To obtain the temporal evolution of soil temperature, SMAP numerically solves Eq. 3.12 using the finite difference implicit method. Herein, we take 170 model layers with varying thicknesses  $d$  in soil with an overall thickness of 1000 cm.

Specifically,  $d$  is equally set to be 1 cm in the top 20 cm, 2 cm at depths of 20–100 cm, 5 cm at depths of 100–300 cm and 10 cm at depths greater than 300 cm. The boundary condition of Eq. 3.12 at the soil surface was given by the Neumann type condition, which is a consequence of the surface energy balance and essentially the same as that employed in the snowpack simulation explained by *Niwano et al.* (2012). At the bottom of the soil, we also selected the Neumann boundary condition, with zero flux assumed. The thermal conductivity of soil  $k_g$  in Eq. 3.12 was calculated using the parameterization by *Peters-Lidard et al.* (1998):

$$k_g = K_e(k_{sat} - k_{dry}) + k_{dry}, \quad (3.13)$$

where  $K_e$  is the Kersten number (a function of the degree of soil saturation),  $k_{sat}$  is saturated soil

thermal conductivity and  $k_{dry}$  is dry soil thermal conductivity. The two types of thermal

conductivities ( $k_{sat}$  and  $k_{dry}$ ) were given as functions of soil porosity and quartz content, respectively.

At the same time, we considered water flow in the soil using exactly the same equation as that employed for the water movement simulations in the snowpack described in Sect. 3.2.3.1. (Richards equation: Eq. 3.1). Again, in this soil submodel, the hydraulic diffusivity  $D$  and the hydraulic conductivity  $K$  are calculated from the van Genuchten model (*van Genuchten*, 1980) as functions of saturated hydraulic conductivity  $K_s$  and model parameters  $\alpha$  and  $n$ .

Ultimately, the problem comes down to the question of how to determine the five unknown parameters of soil porosity, quartz content,  $K_s$ ,  $\alpha$  and  $n$ . Although these parameters are largely controlled by soil types (e.g., *Peters-Lidard et al.*, 1998; *van Genuchten*, 1980), they are highly site-specific. Therefore, it is ideal to perform *in situ* measurements of these soil physical parameters, as conducted by *Iwata et al.* (2010), when a parameterization by *Peters-Lidard et al.* (1998) or the van



Genuchten model is employed strictly. However, in the present study, we focus only on providing realistic ground heat flux from the soil to the snowpack using the soil submodel; therefore, seeking precise soil properties in Nagaoka is beyond the scope of this paper. In the following numerical simulations, the soil porosity and quartz content were given from *Peters-Lidard et al.* (1998), the three van Genuchten model parameters were taken from a list presented by *van Dam and Feddes* (2000) and we provisionally assumed the soil type to be clay.

### 3.2.4. Model simulations and evaluation

SMAP requires some model input parameters: the number of subbands to be used in PBSAM, time step  $\Delta t$  and minimum and maximum model snow layer thicknesses  $d_{min}$  and  $d_{max}$  (*Niwano et al.*, 2012). Following *Niwano et al.* (2012), we employed four subbands for both the UV-visible and near-infrared bands in PBSAM, set  $\Delta t = 50$  s and forced the model snow layer thickness to the range between  $d_{min} = 0.5$  cm and  $d_{max} = 3$  cm. In every time step, the forcing variables explained in Sect. 3.2.1., which were updated every 30 min, were used. In the numerical simulations carried out at Nagaoka, additional site-specific settings for new snow density and roughness length for momentum of the snow surface were considered. At present, SMAP is equipped with the functions for new snow density  $\rho_{s,new}$  introduced by *Yamazaki* (1998, 2001), *Kajikawa* (1989) and *Lehning et al.* (2002b). When SMAP was applied at Sapporo, we employed the function by *Yamazaki* (1998, 2001), because it was developed and well validated under the climate condition at Sapporo (*Niwano et al.*, 2012). However, in the present case, we selected the following function by *Kajikawa* (1989) in order to exclude effects due to new snow density calculation on total model performance as much as possible:

$$\rho_{s,new} = 3.6u - 0.2T_a + 62, \quad (3.14)$$

where  $u$  is wind speed and  $T_a$  is air temperature. The usefulness of this function for wet snow condition

at Nagaoka has been confirmed by SNOWPACK simulations conducted by *Yamaguchi et al.* (2004) and *Saito et al.* (2012). The roughness length for momentum  $z_0$  is set to be  $7 \times 10^{-4}$  m following *Yamaguchi et al.* (2004).

Initially, evaluation of SMAP new\_ctl was conducted at Sapporo (2007–2009 winters) by introducing the indices of root mean square error (*RMSE*) and mean error on model accuracy (*ME*: the average of the difference between simulated values and observed values), which were obtained from a comparison of measured and simulated data. In Sect. 3.3.1, using the same data as *Niwano et al.* (2012) employed, we demonstrated the effects of the three newly implemented snow physical schemes (water movement, snow settlement and treatment of turbulent heat exchanges under very stable conditions) on snow depth (as well as column-integrated SWE) and snow surface temperature by comparing the results from new\_ctl with those from old\_ctl (*Niwano et al.*, 2012). Furthermore, we investigated the individual effects of each scheme by model sensitivity tests, where every scheme was sent back to the old ones from new\_ctl, as explained in Sect. 3.2.3. In the following, we refer to these numerical sensitivity tests as “new\_st1,” “new\_st2,” and “new\_st3.” They are essentially the same as “new\_ctl” but employ old schemes for water movement (water percolation in the snowpack is controlled by mass fraction of water), snow settlement (*Bader and Weilenmann*, 1992; *Morris et al.*, 1997) and turbulent heat exchanges under stable conditions ( $H_S$  and  $H_L$  were set to be 0 when the bulk Richardson number exceeded the critical Richardson number). In addition, we performed another sensitivity test named as “new\_dfc” to assess impacts of the scheme of *Goudriaan* (1977), which calculates diffuse fractions of UV-visible and near-infrared radiant fluxes. In new\_dfc, model settings are definitely as same as new\_ctl, but diffuse fractions of UV-visible and near-infrared radiant fluxes are calculated by SMAP itself using the scheme. The purpose of this test is to comprehend uncertainties caused by the scheme that is employed as default at Nagaoka, where these radiant fluxes are not

available.

Further model validation was performed using the data obtained at Nagaoka during the 2011–2012 winter. At Nagaoka, the newly developed soil submodel was coupled to SMAP to provide realistic ground heat flux into the snowpack. As mentioned in Sect. 3.2.1.2., observed soil temperatures (at 10, 20, 50, 80, 100 and 150 cm depths) were utilized to initialize the soil temperature profile. In the model soil layers (explained in Sect. 3.2.3.4.) shallower than 150 cm in depth, initial soil temperatures were calculated by linear interpolation using the observed data, while initial soil temperatures at depths greater than 150 cm were equated simply with the observed soil temperature at 150 cm depth. The validated parameters were snow depth, column-integrated SWE, column-average snow density, soil temperature profile, profiles of volumetric water content of snow and snow surface temperature. The validity of the calculated ground heat flux by the soil submodel is implicitly assessed from the simulated soil temperature profile in Sect. 3.3.2.

### **3.3. Results and discussion**

#### **3.3.1. Sapporo**

##### **3.3.1.1. Meteorological and snow conditions**

Meteorological conditions during the 2007–2008 and 2008–2009 winters at Sapporo were contrasting in terms of temperature. Average daily mean air temperatures during the period from December to March, when the snowpack existed continuously for both winters, were  $-1.58^{\circ}\text{C}$  for the first winter and  $-0.34^{\circ}\text{C}$  for the second (*Niwano et al.*, 2012). Although accumulated precipitation during the period from November to April was 385 mm for the first winter and 438 mm for the second, the snow depth after late January was greater during the first winter than the second. As for the near-surface mass concentrations of snow impurities (BC and dust), they were almost the same during the two winters. Median mass concentrations of dust and BC in the top 2 cm snow layers were 4.63 and 0.217 ppmw for the first winter, and 3.86 and 0.207 ppmw for the second, which are much higher than *in*

**Table 3.1.** Comparison of SMAP simulation results with *in situ* measurements in terms of snow depth during 2007–2009 winters at Sapporo, Japan. Experiments refer to model settings: “old\_ctl” follows the old control setting by *Niwano et al.* (2012) and “new\_ctl” is the updated version presented in this study. Three sensitivity tests indicated by “new\_st1,” “new\_st2,” and “new\_st3” are the same as “new\_ctl,” except that they employ old schemes for water movement, snow settlement and turbulent heat exchanges under stable conditions, respectively. Additional experiment “new\_dfc” is the same as “new\_ctl,” but it calculates diffuse fractions of UV-visible and near-infrared radiant fluxes using the scheme of *Goudriaan* (1977). *RMSE* and *ME* are abbreviations for root mean square error and mean error (the average of the difference between simulated values and observed values), respectively.

Parameter	Experiments	Period	<i>RMSE</i>	<i>ME</i>
Snow depth (m)	<b>old</b>	<b>2007-2008</b>	<b>0.064</b>	<b>0.045</b>
	<b>new_ctl</b>	<b>“</b>	<b>0.045</b>	<b>0.009</b>
	new_st1	“	0.043	0.016
	new_st2	“	0.063	0.004
	new_st3	“	0.048	0.028
	new_dfc	“	0.058	0.029
	<b>old</b>	<b>2008-2009</b>	<b>0.075</b>	<b>0.044</b>
	<b>new_ctl</b>	<b>“</b>	<b>0.050</b>	<b>0.014</b>
	new_st1	“	0.052	0.018
	new_st2	“	0.060	0.021
	new_st3	“	0.052	0.021
	new_dfc	“	0.057	0.024

*situ* measurement results obtained in the Arctic (*Aoki et al.*, 2011).

### 3.3.1.2. Snow depth

Figures 3.1a and 3.1b compares the time series of observed and simulated (with old\_ctl and new\_ctl)

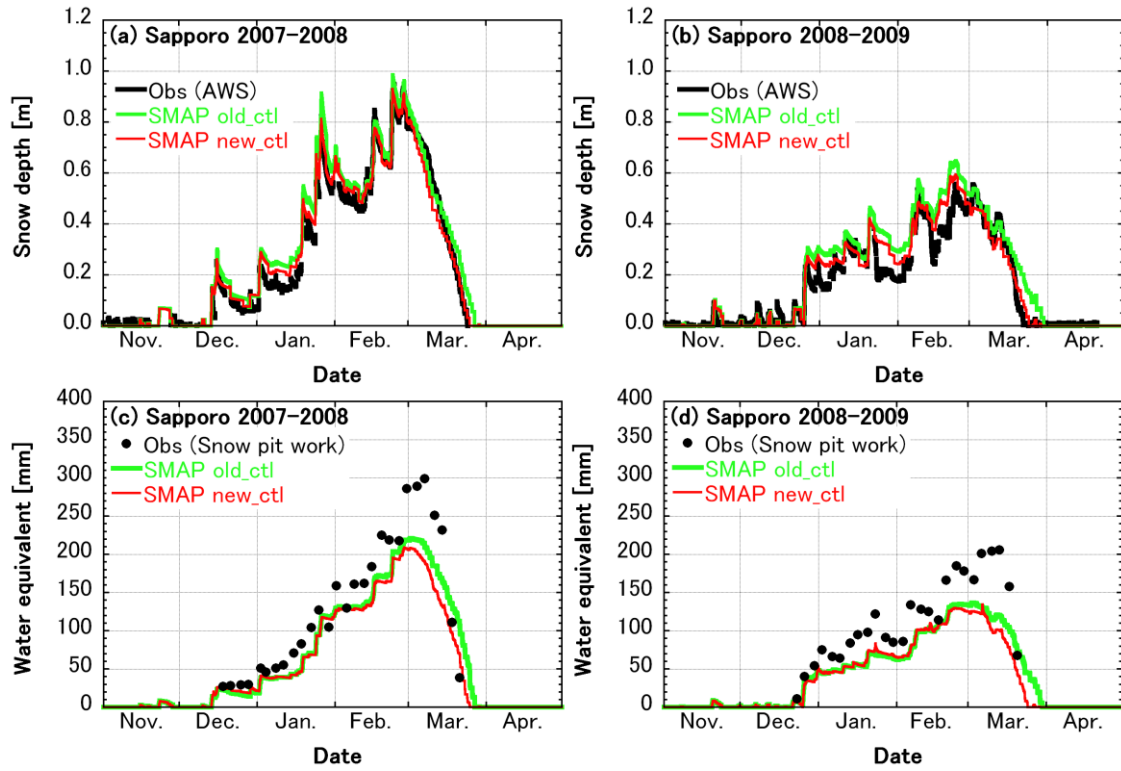


**Figure 3.1.** Seasonal evolution of observed (a, b) snow depth (black solid curves) and (c, d) column-integrated snow water equivalent (SWE) (black dots) during the 2007–2008 and 2008–2009 winters at Sapporo, Japan. Temporal changes in snow depth and SWE simulated with SMAP (green solid curves for the old version “old\_ctl” and red solid curves for the updated version “new\_ctl”) are also depicted.

snow depths at Sapporo during the 2007–2008 and 2008–2009 winters. In both winters the tendency of SMAP old\_ctl to overestimate snow depth was reduced in new\_ctl. Although the timing of complete melting during the 2008–2009 winter in the old\_ctl simulation was delayed from that in 2007–2008 (by about a week), the simulation by new\_ctl agreed with the observation satisfactorily. In fact, the *ME* values were reduced from 0.045 to 0.009 m and from 0.044 to 0.014 m for the 2007–2008 and 2008–2009 winters, respectively (Table 3.1). The *RMSE* values were also reduced (0.064 to 0.045 m and 0.075 to 0.050 m for each winter, respectively), suggesting that overall model performance was

**Table 3.2.** As Table 3.1, but for snow surface temperature.

Parameter	Experiments	Period	<i>RMSE</i>	<i>ME</i>
Snow surface temperature (°C)	<b>old</b>	<b>2007-2008</b>	<b>2.45</b>	<b>-0.30</b>
	<b>new_ctl</b>	<b>"</b>	<b>2.03</b>	<b>0.62</b>
	new_st1	"	1.82	0.53
	new_st2	"	2.12	0.63
	new_st3	"	2.40	-0.05
	new_dfc	"	1.91	0.45
	<b>old</b>	<b>2008-2009</b>	<b>2.03</b>	<b>-0.67</b>
	<b>new_ctl</b>	<b>"</b>	<b>1.50</b>	<b>-0.13</b>
	new_st1	"	1.42	-0.20
	new_st2	"	1.49	-0.14
	new_st3	"	1.88	-0.49
	new_dfc	"	1.49	-0.10

improved in new\_ctl. The most effective process for inducing this improvement was examined from the three sensitivity tests: new\_st1, new\_st2 and new\_st3 (Table 3.1). While the *RMSE* obtained from new\_st1 and new\_st3 were almost the same as that from new\_ctl, that from new\_st2 was obviously larger than that from new\_ctl for both winters, implying that the newly implemented snow settlement scheme by *Vionnet et al.* (2012) (Sect. 3.2.3.2.) played the most important role in improving the accuracy of snow depth simulations at Sapporo during both winters. In order to verify the usefulness of the newly improved snow settlement process, we compared column-integrated SWE obtained from old\_ctl and new\_ctl in Figs. 3.1c and 3.1d. These figures denote that simulated column-integrated SWE by old\_ctl and new\_ctl are almost on the same order during accumulation period, however, mass loss was enhanced in new\_ctl especially at the beginning of ablation period for both winters. This result implies that the newly implemented snow settlement scheme by *Vionnet et al.* (2012) performs reasonably during accumulation period at Sapporo, however, its efficiency during ablation period should be further inspected.

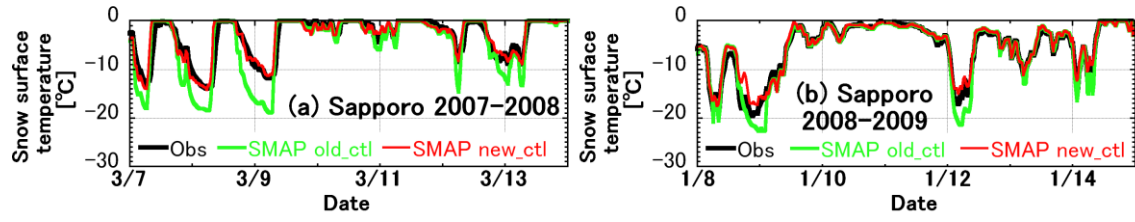


**Figure 3.2.** Examples of snow surface temperature comparisons between observation (black solid curves) and simulations (green solid curves for the old version “old\_ctl” and red solid curves for the updated version “new\_ctl”) during the (a) 2007–2008 and (b) 2008–2009 winter at Sapporo, Japan.

In addition, we investigated impacts of the scheme by *Goudriaan* (1977) on SMAP model performance. Comparison of the *RMSE* and *ME* values obtained from new\_dfc against those from new\_ctl indicates they are almost equal.

### 3.3.1.3. Snow surface temperature

The other issue to be resolved for old\_ctl was the underestimation of snow surface temperature, especially during stable atmospheric conditions. Figure 3.2 gives examples of significant underestimation of snow surface temperature by old\_ctl during the 2007–2009 winters at Sapporo, as discussed by *Niwano et al.* (2012). On the contrary, in new\_ctl, the bias has been fixed and simulation results fitted observations better. From the statistical point of view (Table 3.2), *ME* was improved in new\_ctl during the 2008–2009 winter ( $-0.67\text{ }^{\circ}\text{C}$  to  $-0.13\text{ }^{\circ}\text{C}$ ). However, during the 2007–2008 winter, the sign of *ME* turned from negative to positive and the absolute model bias increased ( $-0.30\text{ }^{\circ}\text{C}$  to  $0.62\text{ }^{\circ}\text{C}$ ). The reason for these changes can be mainly attributed to treatment of turbulent heat exchanges under very stable conditions, as indicated by the relatively large differences in *RMSE* and *ME* between new\_ctl and new\_st3 (Table 3.2). In SMAP sensible heat flux  $H_s$  is calculated as follows (*Niwano et al.*, 2012):

$$H_S = \rho_a c_{pa} C_H u (\theta - \theta_{s0}), \quad (3.15)$$

where  $\rho_a$  is the density of air,  $c_{pa}$  is the specific heat capacity of air at constant pressure,  $C_H$  is the bulk transfer coefficient for sensible heat and  $\theta$  and  $\theta_{s0}$  are potential temperature at measurement height of air temperature (1.5 m at Sapporo and 3.5 m at Nagaoka) and the snow surface, respectively. In practice,  $C_H$  is diagnosed at every time step considering atmospheric stability conditions (Niwano *et al.*, 2012). The new treatment introduced in Sect. 3.2.3.3. generally acts to increase  $C_H$ , and heating from the atmosphere to the snow surface can be reinforced, even under very stable conditions. In new\_ctl the smaller maximum Richardson number gives the larger  $H_S$  (i.e., surface heating is enhanced). Therefore, a possible cause for the deterioration in *ME* during the 2007–2008 winter could be the choice of the maximum Richardson number. To increase the model accuracy, the appropriate value for the maximum Richardson number should be further explored.

In the end, we investigated effects of the scheme by Goudriaan (1977) on SMAP simulated snow surface temperature by results from new\_dfc. As a result, we could confirm the *RMSE* and *ME* values obtained from new\_dfc were also on the same level with those from new\_ctl, and the scheme is useful when diffuse fractions of UV-visible and near-infrared radiant fluxes are not available.

### 3.3.2. Nagaoka

In this section, we apply SMAP to the snow at Nagaoka. It is worth testing and validating the new\_ctl setting of SMAP under the climatic conditions with high precipitation and frequent wet snow for the first time.

#### 3.3.2.1. Meteorological and snow conditions

Figure 3.3 depicts seasonal variations of observed meteorological conditions and near-surface mass concentration of snow impurities at Nagaoka during the 2011–2012 winter. At Nagaoka air



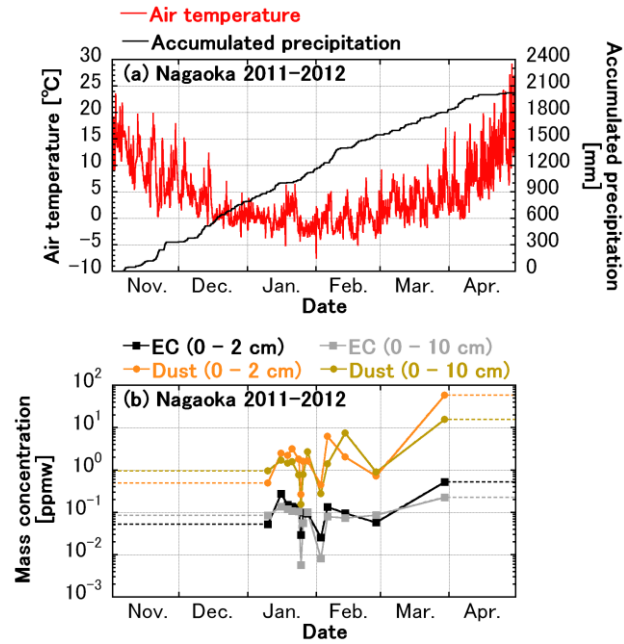


**Figure 3.3.** Observed conditions of (a) air temperature (red solid curve) and accumulated precipitation (black solid curve) and (b) mass concentrations of elemental carbon (EC) and dust for the top 2 and 10 cm of snowpack during the 2011–2012 winter at Nagaoka, Japan. Dashed lines indicate periods when no measurements were made.

temperature often exceeded over 0 °C even during January and February, and accumulated (corrected) precipitation reached no less than about 2000 mm during the winter (Fig. 3.3a), which is much higher than that in Sapporo (Sect. 3.3.1.1.). The measured mass concentrations of snow impurities (elemental carbon: EC and dust) are illustrated in Fig. 3.3b. In this study we have assumed BC to be equivalent to EC following *Aoki et al.* (2011). During the accumulation period, dust concentration was around 1 ppmw and BC concentration was approximately 0.1 ppmw, while they increased to more than 10 ppmw and approximately 0.2–0.5 ppmw in the ablation period. This feature was almost the same as that observed at Sapporo during the 2007–2009 winters reported by *Aoki et al.* (2011).

**Table 3.3.** As Table 3.1, but for snow depth during 2011–2012 winter at Nagaoka.

Parameter	Experiments	Period	RMSE	ME
	<b>old_ctl</b>	<b>2011–2012</b>	<b>0.268</b>	<b>0.183</b>
	<b>new_ctl</b>	<b>"</b>	<b>0.248</b>	<b>0.183</b>
Snow depth (m)	new_st1	"	0.307	0.241
	new_st2	"	0.273	0.219
	new_st3	"	0.258	0.193

### 3.3.2.2. Snow depth, snow water equivalent and snow density

We began SMAP model evaluation at Nagaoka by investigating the accuracy of mass balance simulated by both old\_ctl and new\_ctl settings during the 2011–2012 winter (Fig. 3.4). Figure 3.4 displays comparisons on snow depth (Fig. 3.4a), column-integrated SWE (Fig. 3.4b) and column-average snow density (Fig. 3.4c), together with the time evolution of model biases. Although simulated complete snow melting was delayed significantly for both settings, new\_ctl still performed better than old\_ctl at Nagaoka. We examined which process played the most important role in improving model performance at Nagaoka, in the same manner as performed at Sapporo (Sect. 3.3.1.2.). Table 3.3 indicates model performances with old\_ctl, new\_ctl, new\_st1, new\_st2 and new\_st3 settings, which were explained in Sect. 3.3.1.2. Because the largest differences of *RMSE* and *ME* between new\_ctl and the three sensitivity tests was found in new\_st1, we confirmed that the most effective process in improving snow depth simulations during the 2011–2012 winter at Nagaoka was the incorporation of the detailed water movement process in the snowpack, as introduced in Sect. 3.2.3.1. In the following part we examine the results of new\_ctl. During the accumulation period, simulated column-integrated SWE agreed quite well with the observations. However, underestimation of column-average snow density leads to some overestimation of the snow depth. After the ablation period, substantial overestimation of column-integrated SWE, as well as snow depth emerged, even though

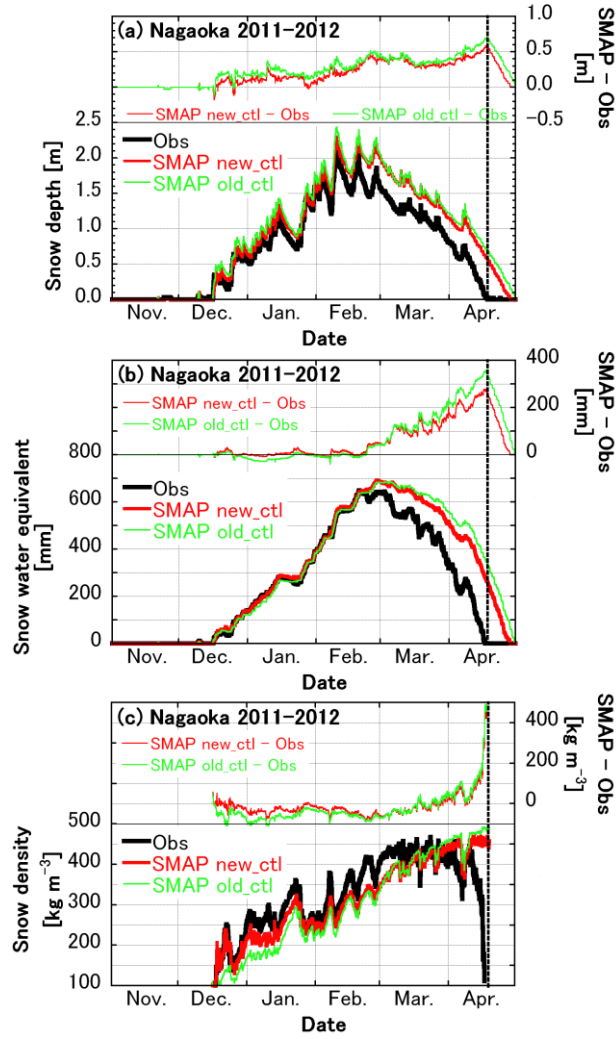


**Figure 3.4.** Comparison of (a) snow depth, (b) column-integrated snow water equivalent and (c) column-average snow density between observations (black solid curves) with simulation results from old and updated version of SMAP (old\_ctl: green solid curves and new\_ctl: red solid curves) during the 2011–2012 winter at Nagaoka, Japan. Temporal evolutions of model biases (SMAP simulations – observations) are also indicated in each panel. Vertical dashed lines denote the observed timing for complete melting of snowpack.

underestimation of column-average snow density was settled and it turned to be overestimated.

Generally, possible reasons for this type of delay in simulated snow melting are: (1) insufficient

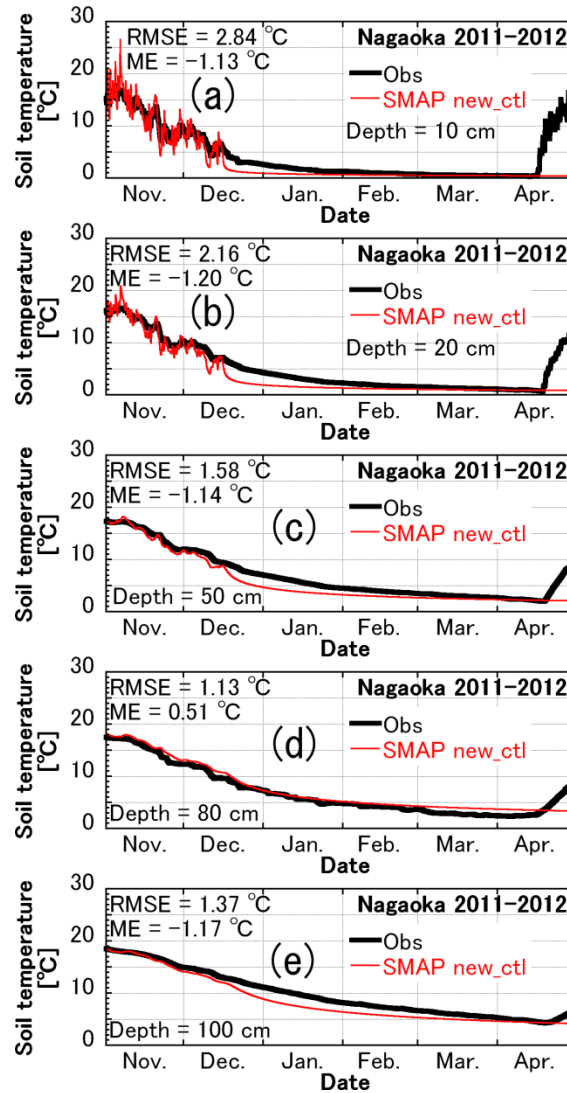


**Figure 3.5.** Seasonal evolution of soil temperatures at (a) 10 cm, (b) 20 cm, (c) 50 cm, (d) 80 cm and (e) 100 cm in depth simulated by the updated version of SMAP (new\_ctl: red solid curves) together with observations (black solid curves) during the 2011–2012 winter at Nagaoka, Japan.

heating from the underlying ground, (2) failure in simulations of melt water movement and subsequent increase in porosity, (3) excessive formation of near-surface refreezing layers as a result of defects in the surface energy balance calculation and (4) observation error in input meteorological parameters.

We next discuss the respective possibilities of these suggested reasons.

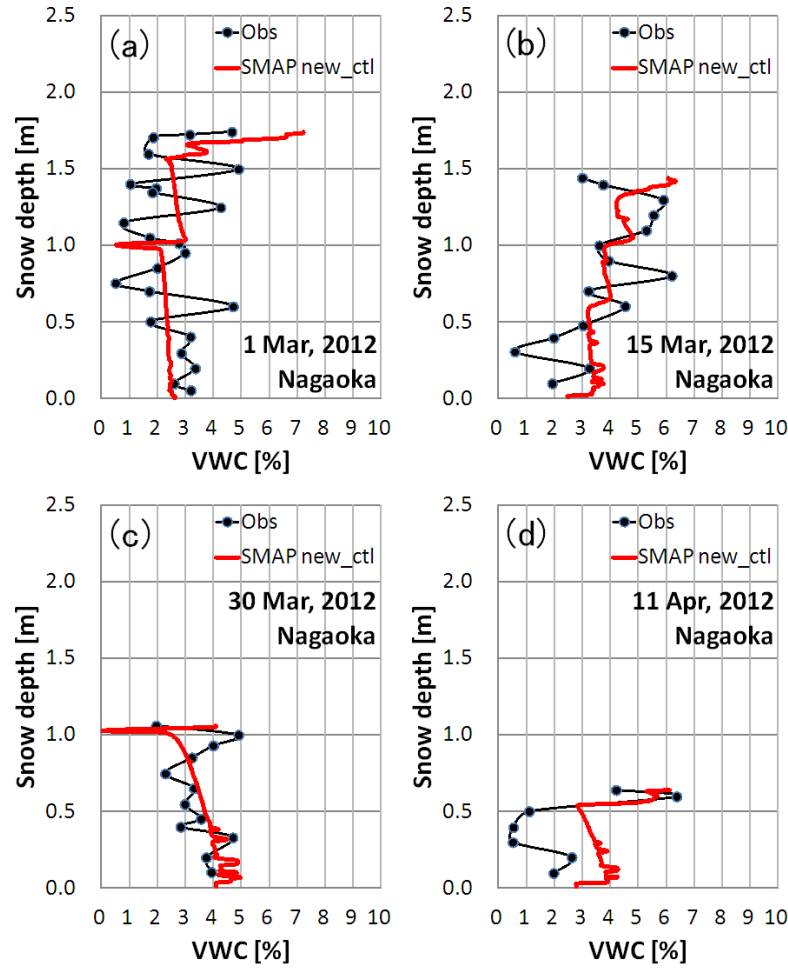


**Figure 3.6.** Profile comparison for volumetric water content (VWC) between observations (black solid curves with filled circles) and simulations by the updated version of SMAP (new\_ctl: red solid curves) during the ablation period of the 2011–2012 winter: (a) March 1, (b) March 15, (c) March 30, and (d) April 11 at Nagaoka, Japan. Simulated snow depths are adjusted to the observations.

### 3.3.2.3. Soil temperature

In the simulation performed at Nagaoka for this study, the ground heat flux was calculated from the soil submodel introduced in Sect. 3.2.3.4. Average simulated ground heat flux (defined to be positive when it is directed downward) was  $-8.4 \text{ W m}^{-2}$  during January and February, and  $-5.8 \text{ W m}^{-2}$  during March and April. We first checked whether the soil submodel could reproduce soil temperature and

ground heat flux adequately. Figure 3.5 illustrates the seasonal evolution of soil temperatures (at 10, 20, 50, 80 and 100 cm in depth) at Nagaoka during the 2011–2012 winter simulated by new\_ctl. Although new\_ctl was prone to underestimate soil temperature, especially during mid-December to early March, the observed seasonal evolution was roughly reproduced and calculated soil temperatures could meet observations during the ablation period. From these results we indirectly confirmed that the ground heat flux, at least during the ablation period, could be simulated reasonably and we could thus abandon the first possibility mentioned above.

#### **3.3.2.4. Volumetric water content in the snowpack**

Next, we investigated the accuracy of simulated volumetric water content profiles by comparing them with measurements obtained from snow pit observations. In this process we adjusted the simulated snow depths into observed snow depths. Figure 3.6 shows selected comparisons during the ablation period. As shown in the figures, there were no large discrepancies in the amount of volumetric water content between observations and simulations, implying that the newly incorporated water movement scheme worked reasonably and it could not thus be the main cause of the snow-melt delay. To improve the performance of new\_ctl and reproduce observed frequent fluctuations found in the volumetric water content profiles, it would be necessary to calculate the new snow density and snow grain size, as well as their evolution (snow settlement and snow metamorphism) more accurately, because the present formulations governing the water movement in the snowpack are controlled by snow grain size and snow density, as explained in Sect. 3.2.3.1. In addition, it would be necessary to take heterogeneous 3d water movement in the snowpack into account in some way.

#### **3.3.2.5. Snow surface temperature**

Finally, we looked at the surface energy balance simulated by new\_ctl in terms of snow surface temperature. Figure 3.7a compares observed and simulated snow surface temperatures at Nagaoka during the 2011–2012 winter. Although *RMSE* and *ME* during the entire winter season were

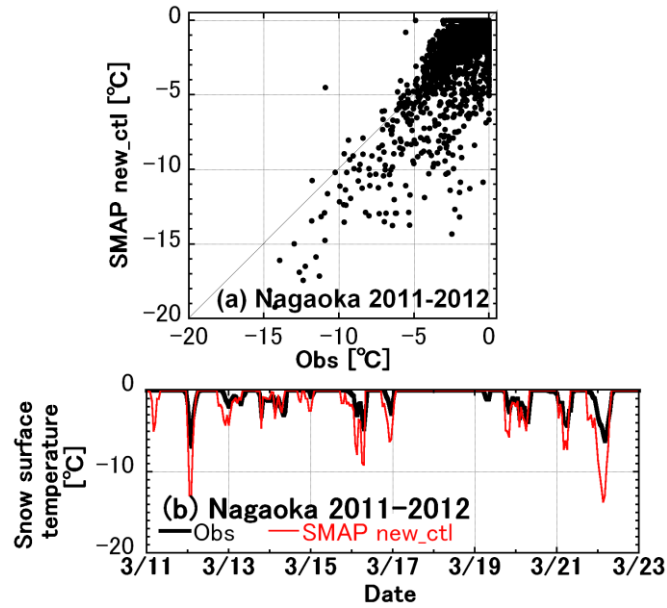


**Figure 3.7.** (a) Scatter plot for snow surface temperature between observation and simulation by the updated version of SMAP (new\_ctl) during the 2011–2012 winter at Nagaoka, Japan. (b) Example of diurnal cycles of snow surface temperature comparing between observation and simulation.

sufficiently low ( $1.49\text{ }^{\circ}\text{C}$  and  $-0.31\text{ }^{\circ}\text{C}$ , respectively) compared with simulation results at Sapporo in the 2007–2009 winters (Table 3.2), underestimation was enhanced, especially when the snow surface did not reach  $0\text{ }^{\circ}\text{C}$ . In fact, *RMSE* and *ME* for the case when the observed snow surface temperature was negative was  $2.17\text{ }^{\circ}\text{C}$  and  $-0.65\text{ }^{\circ}\text{C}$ , respectively. This underestimation could even be found during ablation period (Fig. 3.7b). This means that, in SMAP, the heating energy available during the daytime was first used to heat the cooled snow surface temperature; thus, there was insufficient energy remaining for the surface melt. Besides, the present result suggests that new treatment introduced in Sect. 3.2.3.3. was not effective in this case. During the 2011–2012 winter, average observed wind speed at Nagaoka was lower ( $0.67\text{ m s}^{-1}$ ) compared to those at Sapporo during the 2007–2009 winters ( $1.94$  and  $2.69\text{ m s}^{-1}$ ). Since turbulent heat fluxes calculated by SMAP are controlled by not only the bulk transfer coefficient but also wind speed (Eq. 3.15), the present treatment could not be effective

under weak wind condition at Nagaoka during the 2011-2012 winter. Therefore, it is necessary to develop more accurate formulation for turbulent heat fluxes. At present, we do not have substantive information to judge which mechanism was the main cause for this failure in the surface energy balance calculation: the formulation of SMAP itself or observational errors in the input meteorological data. According to Yamaguchi *et al.* (2004), they also encountered almost the same situation in their SNOWPACK model simulations at Nagaoka and Shinjo. The maximum snow depth error increased with increasing observed maximum snow depth (more than about 1 m). Therefore, it is necessary to perform further investigations on snow-melt processes for thick seasonal snowpack. For this purpose, it would be effective to acquire more comprehensive knowledge regarding characteristics of SMAP model performance by extending model evaluations to more seasons and more sites.

### **3.4. Conclusions**

To solve the problems of SMAP pointed out by Niwano *et al.* (2012) with their model evaluations at Sapporo during the 2007–2009 winters, namely (1) overestimation of snow depth, especially during the warm 2008–2009 winter when the air temperatures were often above 0 °C, even in the accumulation period and (2) enhanced underestimation of snow surface temperature under very stable conditions, we performed the following model updates:

- implementation of a detailed scheme of water movement in the snowpack based on the Richards equation and the van Genuchten model (*van Genuchten*, 1980; *Shimizu*, 1970; *Hirashima et al.*, 2010; *Yamaguchi et al.*, 2010, 2012);



- incorporation of a physically realistic snow settlement formulation that considers the effects of snow density, snow temperature, absolute liquid water content and geometric snow grain size (Vionnet *et al.*, 2011); and
- modification of the treatment of turbulent heat exchanges under very stable conditions by setting a limitation for the Richardson number to ensure minimum turbulent exchanges.

Using the same data as Niwano *et al.* (2012) employed, we evaluated the performance of the updated SMAP model, new\_ctl. Additional sensitivity tests to inspect the individual effects of the above-mentioned three updates were also conducted. Consequently, we found that snow depth simulations were improved in new\_ctl for both the 2007–2008 and 2008–2009 winters, as the scores indicating model accuracy (*ME* and *RMSE*) were reduced significantly. The most effective update for this improvement at Sapporo was the introduction of the snow settlement scheme by Vionnet *et al.* (2011). The underestimation of the snow surface temperature was also improved, mainly by revising the treatment of turbulent heat exchanges under very stable conditions. However, we highlighted that the choice of maximum Richardson number should be examined in more detail, because surface heating was more enhanced in new\_ctl compared to old\_ctl, the sign of *ME* turned from negative to positive and the absolute model bias increased during the 2007–2008 winter.

Next, SMAP was applied to Nagaoka, which is located in one of the heaviest snow-fall regions in Japan and is subject to melt forms throughout the winter season. The purpose of this application was to test the reliability of SMAP by demonstrating its usability under different climate conditions. Because ground heat flux, which is used for the bottom boundary condition for solving energy conservation equation of the snowpack in SMAP, was not available at Nagaoka during the 2011–2012 winter when the present numerical studies were performed, we developed a soil submodel that

provides realistic ground heat flux into the snowpack. The soil submodel employs an energy conservation equation that considers phase changes and convection flow as its governing equation. Furthermore, water flow in the soil is controlled by the Richards equation, as well as by the van Genuchten model (*van Genuchten*, 1980). Results from the snow-soil-coupled simulations by SMAP new\_ctl proved that model-estimated ground heat flux could be reasonably calculated and also that water movement in quite thick snowpack (more than 2.0 m) could also be simulated reasonably well. In addition, we found that new\_ctl performed better compared than old\_ctl at Nagaoka in terms of mass balance simulations. The most effective process in this improvement was the implementation of a detailed scheme of water movement in the snowpack (*van Genuchten*, 1980; *Shimizu*, 1970; *Hirashima et al.*, 2010; *Yamaguchi et al.*, 2010, 2012). However, we still found underestimation of the snow surface temperature, as well as substantial overestimation of column-integrated SWE and snow depth by SMAP new\_ctl after ablation period. We discussed two possible reasons for these failures: a defect in the SMAP model calculations in the surface energy balance simulation and observational errors in the model input data. Because a situation similar to the present study was reported in the previous simulation study by *Yamaguchi et al.* (2004) with the SNOWPACK model, we conclude that it is necessary to perform further investigation on snow-melt processes for thick seasonal snowpack.

## **Acknowledgements**

We gratefully appreciate the very helpful comments by Takeshi Yamazaki and an anonymous reviewer. This study is supported in part by (1) Japan Society for the Promotion of Science (JSPS), Grant-in-Aid for Scientific Research (S), number 23221004, (2) the Grant for Joint Research Program, the Institute of Low Temperature Science, Hokkaido University, (3) the Experimental Research Fund for Global Environment Conservation, the Ministry of the Environment of Japan and (4) the Global Change Observation Mission - Climate (GCOM-C) / the Second-generation GLobal Imager (SGLI) Mission, the Japan Aerospace Exploration Agency (JAXA).



## **4. Wintertime snow surface energy balance and ablation characteristics at Sapporo, Japan (2005–2015)**

### **4.1. Introduction**

Snow cover, of which ~98% of its extent is recognized in the Northern Hemisphere, occupies the second-largest portion of the cryosphere with a mean maximum areal extent of 47 million km<sup>2</sup> following the seasonally frozen ground (Armstrong and Brun, 2008). As the presence of snow cover modulates the surface energy balance (SEB) through albedo (snow surface is characterized by its relatively high albedo among all terrestrial land surface types) and temperature (snow surface temperature never rises above 0 °C), it plays an important role in the global climate system. For example, the presence of seasonal snow cover has a significant influence on the ground thermal regime in cold regions (e.g., Zhang, 2005; Iwata et al., 2010). Therefore, with recent climate change, special attention has been paid to the duration of snow cover. Brown and Mote (2009) clarified that the largest decreases of trends in snow cover duration during the 1966–2007 period were concentrated in a zone where seasonal mean air temperatures were in the range of –5 to +5 °C, which extended around the mid-latitudinal coastal margins of the continents. Tedesco et al. (2009) investigated pan-arctic terrestrial snowmelt trends for the period 1979–2008 derived from space-borne microwave brightness temperature and revealed that melt has been starting (finishing) ~0.5 days year<sup>–1</sup> (~1 days year<sup>–1</sup>) earlier and the length of the melting season is shortening by ~0.6 days year<sup>–1</sup>. Brown and Robinson (2011) elucidated that the Northern Hemisphere spring snow cover extent has undergone significant reductions over the past ~90 years and that the rate of this decrease has accelerated over the past 40 years. Derksen and Brown (2012) demonstrated that the rate of loss of the June snow cover extent between 1979 and 2011 was –17.8% decade<sup>–1</sup>, which was greater than the loss of the September sea ice extent (–10.6% decade<sup>–1</sup>) over the same period.

In order to understand the ongoing rapid changes in the physical states of the terrestrial snowpack, it is extremely important to perform detailed in-situ measurements focusing on the snowpack as well as surface meteorology from various aspects continuously. An in-depth understanding of the observed features with the aid of physical snowpack models would enable a high precision of future climate predictions, especially in the cryosphere. For example, in the Greenland ice sheet (GrIS), Steffen and Box (2001) installed 18 automated weather stations (AWS) distributed in most of the climatic zones in the GrIS. The AWS network established in spring 1995 is called GC-net (Greenland Climate Network) and has been providing valuable long-term datasets for surface meteorology. van den Broeke et al. (2011) presented a record of the SEB as well as surface meteorology obtained from their three AWS located along the K-transect, a stake array in southwest Greenland. The data was employed to develop a regional climate model known as RACMO2 (Ettema et al., 2010a, 2010b). In the mid-latitudes, Météo-France has a long history of conducting snow and meteorological measurements at the experimental station Col de Porte, located in the French Alps (Morin et al., 2012). Using the data obtained at the site, a multi-layered physical snowpack model called Crocus was developed (e.g., Brun et al., 1989, 1992; Vionnet et al., 2012; Morin et al., 2013). In the Swiss Alps, an AWS at Weissfluhjoch has also been measuring meteorological and snow conditions over a long period of time (Wever et al., 2015). The data was employed for the development of the multi-layered SNOWPACK model (e.g., Bartelt and Lehning, 2002; Lehning et al., 2002a, 2002b; Wever et al., 2015). Recently, an international network of surface measurement stations in the cryosphere called CryoNet has been organized by the World Meteorological Organization's Global Cryosphere Watch (<http://globalcryospherewatch.org/cryonet/sites.php>).

These motivated us to perform continuous climate monitoring, focusing on the wintertime snow-covered period at Sapporo, Japan, where we have performed a wide variety of studies related to

snow physics and chemistry in the last 10 years. Aoki et al. (2006) revealed that the effect of atmospheric aerosol deposition into the snowpack on snow albedo reduction is important for snow albedo variation at Sapporo, where absorptive atmospheric aerosols are frequently deposited into the snow. Following the study, Aoki et al. (2007a) investigated the measured relationships between broadband albedos and the mass concentration of snow impurities and demonstrated that they agreed with the theoretically predicted relationships obtained from calculations with a radiative transfer model for the atmosphere-snow system (Aoki et al., 1999, 2000), where contamination of mineral dust and black carbon are assumed. Now, fully quality-controlled data for near-surface mass concentrations of snow impurities (black carbon and mineral dust) from 2007 to the present have been acquired (Kuchiki et al., 2015). According to Kuchiki et al. (2015), the near-surface mass concentrations of snow impurities showed no discernible trend over the 2007–2013 winters, and they tended to increase with the number of days elapsed since the last snowfall. Kuchiki et al. (2009) succeeded in developing an optical instrument named GSAF (ground-based spectral radiometer system for albedo and flux) to automatically retrieve near-surface mass concentrations of snow impurities and optically equivalent snow grain size (Aoki et al., 2007b). The retrieval algorithm employed a look-up table method as an inverse calculation, in which the table was created from theoretical calculations with a radiative transfer model developed by Aoki et al. (1999, 2000). The retrieval algorithm is now computationally accelerated by Tanikawa et al. (2015), where the forward/inverse calculation has been replaced with the neural network approach and optical estimation technique. Yasunari et al. (2011, 2014) developed and validated the GOSWIM (Goddard Snow Impurity Module) component to calculate snow albedo, considering the effects of snow impurities explicitly, which was incorporated into the National Aeronautics and Space Administration (NASA) Goddard Earth Observing System, Version 5 (GEOS-5) Earth System Model. Aoki et al. (2011) developed a physically based snow albedo model (PBSAM) to calculate

broadband snow albedos and the solar heating profile in the snowpack as functions of the optically equivalent snow grain size and mass concentrations of snow impurities. By taking full advantage of PBSAM's high precision, Niwano et al. (2012, 2014) developed a multi-layered physical snowpack model called SMAP (Snow Metamorphism and Albedo Process), which incorporates the PBSAM component as a core module.

The main purpose of this paper is to present the characteristics of wintertime snow SEB and the resultant ablation at Sapporo from 2005 to 2015 by utilizing in-situ measurements and the SMAP model. As for ablation, we focus on the factors controlling runoff rate during the ablation period (in this study it denotes March and April, while accumulation period indicates November, December, January, and February following Niwano et al. (2012)). In the present study, model simulations were performed from November to April every winter; however, the SEB analysis focused only on the period between December and March. This is because the snowpack did not exist during November or April in some winter seasons. The validity of the SMAP model forced by conventional surface meteorological data and snow depth (explained in Sect. 4.2.4) was evaluated in terms of the column-integrated snow water equivalent (SWE), snow density profile, snow surface temperature, and the snow temperature profile.

Recently, more attention has been paid to the effects of clouds on the SEB and subsequent surface melt than ever before. For instance, Conway et al. (2015) investigated the effects of clouds on surface radiant fluxes in the Southern Alps of New Zealand and concluded that overcast conditions appear to play a crucial role in extending the ablation season out of the traditional summer season by increasing the energy available for the melting of snow and ice during autumn, winter, and spring. Niwano et al. (2015) demonstrated through SEB analysis that low-level clouds accompanied by a significant temperature increase played an important role in the melt event observed at the SIGMA-A site (Aoki et al., 2014) located in the northwest GrIS during the 2012

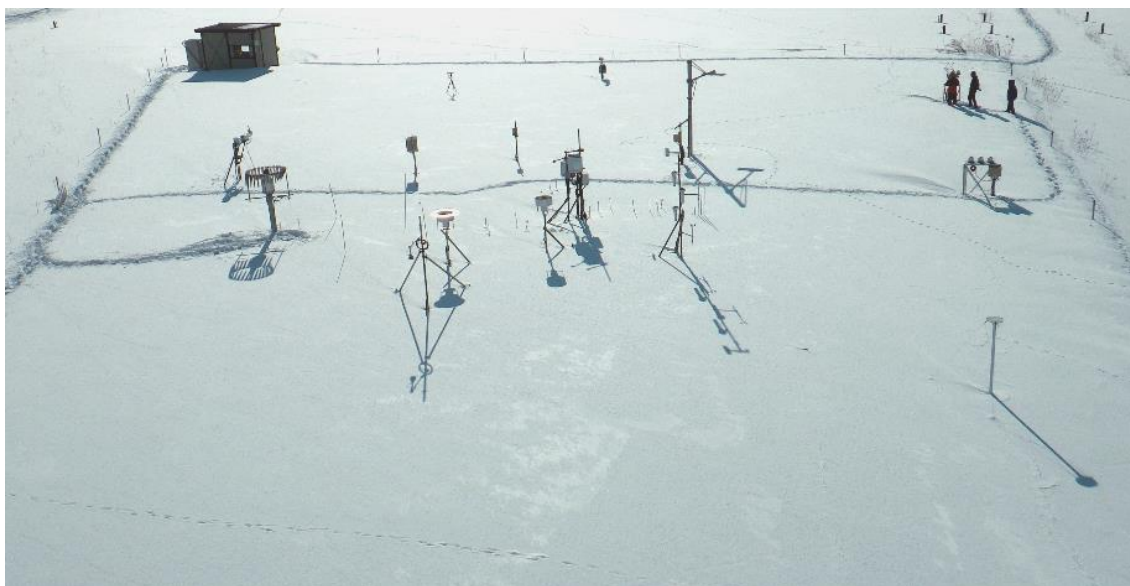


**Figure 4.1.** Panoramic view of the present Sapporo AWS operated since October 2008.

record surface melt event (e.g., Nghiem et al., 2012). Van Tricht et al. (2016) showed that clouds enhance meltwater runoff by about one-third relative to clear skies, where they reduce meltwater refreezing, especially during night time, thereby accelerating bare-ice exposure and enhancing meltwater runoff. Therefore, in this study, we also pay attention to the effects of cloud fraction on snow ablation at Sapporo especially during the ablation period in terms of modeled meltwater runoff.

In the following section, we begin by introducing the in-situ atmospheric and snow measurements performed at Sapporo during the 2005–2015 winters. Then, the setup procedure of the SMAP model numerical simulation performed in this study is described. Using the in-situ data, the SMAP model is evaluated from various aspects and the wintertime snow SEB at Sapporo, calculated by the SMAP model during the study period (2005–2015), is presented. Finally, the characteristics of the modeled meltwater runoff rate from the snowpack at Sapporo during the ablation period are examined.



## **4.2. Data and methods**

### **4.2.1. Meteorological measurements**

Detailed meteorological measurements have been performed at an AWS installed in the observation field in the Institute of Low Temperature Science, Hokkaido University, for more than 10 years. In October 2008, the observation field was moved north-westward by about 0.6 km from the previous position (43°04'56"N, 141°20'30"E, 15 m a.s.l.) to the present position (43°05'09"N, 141°20'11"E, 12 m a.s.l.). In the following section, this observation site is called "Sapporo AWS" as necessary.

Figure 4.1 displays an overview of the environment in the present Sapporo AWS. The Sapporo AWS measured air temperature and relative humidity with a humidity and temperature probe (HMP45D, Vaisala, Finland) protected by an aspirated radiation shield at 1.5 m above the ground surface. In addition, the wind speed at 1.5 m above the ground surface was measured with a wind speed sensor (010C, Met One, USA), the surface air pressure was measured with a barometric pressure sensor (091, Met One, USA), and snow depth was measured with an ultrasonic distance sensor (SR50, Campbell, USA). The measured air temperature, vapor pressure (calculated from relative humidity), and wind speed were converted to values at standard measurement heights (2, 2, and 10 m, respectively) above the snow surface by using the flux profile relationship. Soil heat flux at the ground surface, which was used as a bottom boundary condition for the heat of the snowpack in the SMAP model simulation (explained in Sect. 4.2.4), was measured with a heat flux plate (PHF-01, REBS, USA). During the study period, precipitation measurements were conducted using two types of rain gauges: RT-3 (TK-1, Takeda, Japan) and GEONOR (T-200B, GEONOR, USA). The former sensor (with an accuracy of 3%) was operational during the whole study period, while the latter sensor (with an accuracy of 0.1%) was available from the 2009–2010 winter to the present. Precipitation data obtained with RT-3 and GEONOR were corrected by considering the catch efficiencies of both gauges following Yokoyama et al. (2003) and Forland et al. (1996), respectively.

**Table 4.1.** 10-year-averaged (2005–2015) wintertime monthly-mean surface meteorological conditions, snow albedo, and the snow SEB at Sapporo. Snow albedo and the snow SEB were calculated and averaged only when the snowpack existed. Only cloud fraction was measured at JMA Sapporo, while other variables were obtained at the Sapporo AWS.  $S_{net}$ ,  $L_{net}$ ,  $H_S$ ,  $H_L$ ,  $H_R$ ,  $H_G$ , and  $Q_{net}$  denote the net shortwave radiant flux, net long-wave radiant flux, sensible heat flux, latent heat flux, heat supply by rainfall, subsurface conductive heat flux, and the net energy flux, respectively.

Variable	Dec	Jan	Feb	Mar	Dec–Mar
2 m air temperature (°C)	−0.9	−3.3	−2.7	1.2	−1.4
2 m vapor pressure (hPa)	4.1	3.3	3.5	4.4	3.8
10 m wind speed (m s <sup>−1</sup> )	2.8	3.2	3.4	3.5	3.2
Precipitation (mm)	123	116	89	80	102
Downward shortwave radiant flux (W m <sup>−2</sup> )	56	71	102	143	93
Downward longwave radiant flux (W m <sup>−2</sup> )	264	253	254	268	260
Cloud fraction (0–1)	0.8	0.8	0.8	0.8	0.8
Snow albedo	0.77	0.84	0.81	0.70	0.78
$S_{net}$ (W m <sup>−2</sup> )	10	12	20	43	21
$L_{net}$ (W m <sup>−2</sup> )	−24	−28	−33	−31	−29
$H_S$ (W m <sup>−2</sup> )	16	16	14	21	17
$H_L$ (W m <sup>−2</sup> )	−6	−8	−12	−12	−10
$H_R$ (W m <sup>−2</sup> )	0	0	0	0	0
$H_G$ (W m <sup>−2</sup> )	4	4	6	5	5
$Q_{net}$ (W m <sup>−2</sup> )	0	−5	−5	26	4

In the present study, precipitation data was obtained from the RT-3 measurements until the 2008–2009 winter, when it was taken from the GEONOR measurements from the 2009–2010 winter to the present. As for the radiation-related properties, downward and upward shortwave radiant fluxes were

measured with two sets of pyranometers (CMP21, Kipp & Zonen, the Netherlands), and the downward and upward long-wave radiant fluxes were measured with two sets of pyrgeometers (CG4, Kipp & Zonen, the Netherlands), respectively. These data were sampled and stored in a data logger (CR1000, Campbell, USA) every 1 min, and 30 min averaged or accumulated (for precipitation) fully quality-controlled data were used in the present study.

Using the observed downward and upward long-wave radiant flux ( $L^\downarrow$  and  $L^\uparrow$ ), the snow surface temperature  $T_{s0}$  was obtained from the following relationship:

$$T_{s0} = \left\{ \frac{L^\uparrow - (1 - \epsilon_s)L^\downarrow}{\epsilon_s \sigma} \right\}^{1/4}, \quad (4.1)$$

where  $\epsilon_s$  is the emissivity of the snow surface and  $\sigma$  is the Stefan–Boltzmann constant. In this study,  $\epsilon_s$  was assumed to be 0.98 following Armstrong and Brun (2008). The snow albedo inputted into the model (explained in Sect. 4.2.4) was corrected by employing the so-called accumulated albedo approach (e.g., van den Broeke et al., 2004; Cullen et al., 2014) to reduce errors caused by the cosine response of the pyranometer under the conditions of a high solar zenith angle. Here, the accumulated albedo is defined as the ratio of the sum of the upward shortwave radiant flux and the sum of the downward shortwave radiant flux over a 1-day time window. According to van den Broeke et al. (2004) and Cullen et al. (2014), the snow SEB can be diagnosed realistically using this method. In the following section, the accumulated albedo is simply called albedo.

Table 4.1 lists the 10-year-averaged wintertime monthly-mean (or accumulated) meteorological conditions. January was the coldest month of the winter period within the 10 years, and the 2 m vapor pressure reached a minimum value in the month accordingly. The 10 m wind speed was around  $3 \text{ m s}^{-1}$  throughout the winter period. The monthly-accumulated precipitation amount was over 100 mm during December and January; however, it decreased gradually along with seasonal

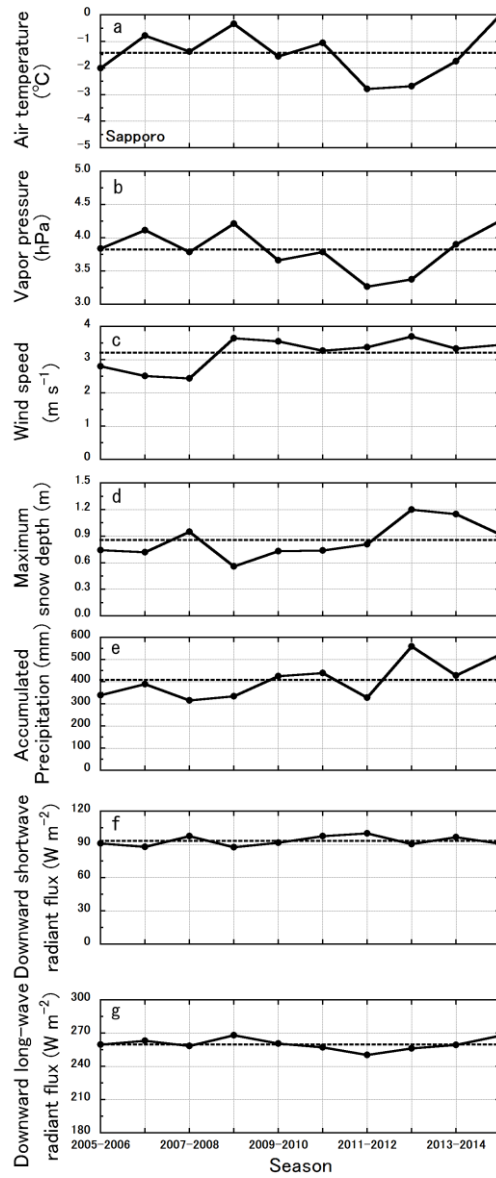


**Figure 4.2.** Inter-annual variabilities of the surface meteorological conditions averaged or accumulated during December to March at the Sapporo (black solid lines) together with the 10-year-averaged values (black dots): (a) 2 m air temperature, (b) 2 m vapor pressure, (c) 10 m wind speed, (d) maximum snow depth, (e) accumulated precipitation, (f) downward shortwave radiant flux, and (g) downward long-wave radiant flux. Accumulated precipitation was observed with the RT-3 rain gauge until the 2008–2009 winter and it was obtained from the GEONOR rain gauge from the 2009–2010 winter onwards.

transition. As for the radiation-related properties, the downward shortwave radiant flux showed a clear seasonal variation: it increased from the accumulation period to the ablation period. On the other hand, the downward long-wave radiant flux was mainly related to air temperature (and vapor pressure).

The inter-annual variabilities of the wintertime averaged meteorological conditions are displayed in Fig. 4.2. The seasonally-averaged 2 m air temperature during the study period was  $-1.4^{\circ}\text{C}$  (Table 4.1). Compared to this value, it can be seen that the 2006–2007, 2008–2009, 2010–2011, and 2014–2015 seasons had warmer winters (Fig. 4.2a). According to Yamaguchi et al. (2009), the 2006–2007 winter season was the warmest season in Japan within more than 100 years as of 2009. During the 2014–2015 winter, the average air temperature reached  $0^{\circ}\text{C}$  for the first time in 10 years. On the other hand, the 2011–2012 and 2012–2013 winters were exceptionally cold seasons. The 2 m vapor pressure (Fig. 4.2b) was around 3.8 hPa (Table 4.1) and ranged between 3.2 and 4.3 hPa. It decreased during the relatively cold seasons and increased during the warmer seasons. In the record of 10 m wind speed (Fig. 4.2c), a clear transition can be seen between the 2007–2008 and 2008–2009 winters. This was caused by the above-mentioned movement of the Sapporo AWS conducted in October 2008, suggesting that wind speed is very sensitive to changes in observation environments. The maximum snow depth at Sapporo (Fig. 4.2d) was less than 1 m until the 2011–2012 winter; however, it exceeded 1 m thereafter. Accumulated precipitation during the winter period was around 400 mm (Fig. 4.2e); however, it ranged widely year by year between 300 and 600 mm. A clear relationship between the accumulated precipitation (or snow depth) and air temperature did not exist. In Japan, the downward shortwave radiant flux was observed to increase (brightening) from the mid-1980s (Ohmura, 2009). Kudo et al. (2012) demonstrated that the brightening observed in Japan has been caused by changes in the aerosol optical properties of single scattering albedo in particular, rather than by changes related to cloud. Figure 4.2f shows the changes in the downward shortwave

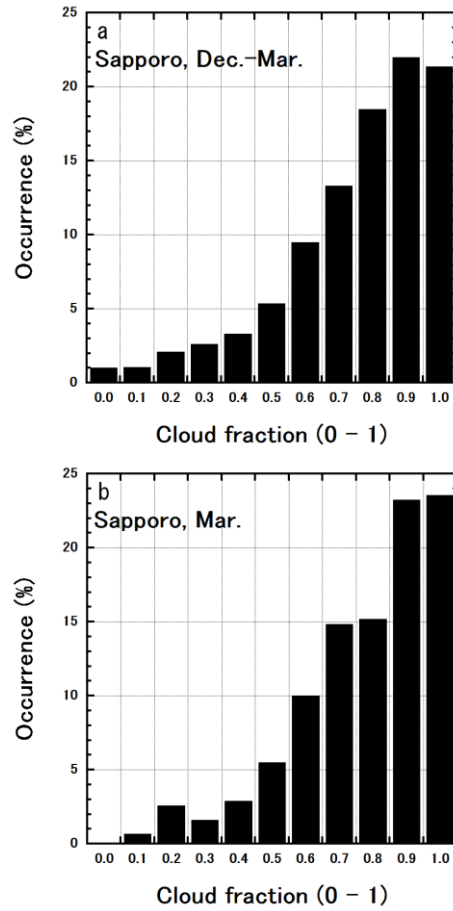


**Figure 4.3.** Occurrence of (a) the wintertime (December to March) and (b) March daily-mean cloud fraction observed at JMA Sapporo from 2005 to 2015.

radiant flux at Sapporo during the study period. Obvious trend cannot be seen during this period.

Again, a clear trend was not found for the downward long-wave radiant flux either; however, it is obvious that the downward long-wave radiant flux was related to air temperature and vapor pressure (Fig. 4.2g).

#### 4.2.2. Cloud fraction observation

In the Sapporo AWS, cloud fraction was not measured during the study period 2005–2015.

Therefore, in this study, it was obtained from the SYNOP (Surface Synoptic Observations) data from

the Sapporo District Meteorological Observatory, Japan Meteorological Agency (43°03'36"N, 141°19'42"E, 17 m a.s.l.; hereafter referred to as "JMA Sapporo"), where operational visual observations of cloud are performed seven times (03, 06, 09, 12, 15, 18, and 21 JST) a day. JMA Sapporo is located about 3 km south of the Sapporo AWS. In this study, daily-mean cloud fraction was employed, calculated simply by averaging these seven measurements. By referring to the measured daily-mean cloud fraction (clf; 0–1), sky conditions are categorized into the following three types: clear-sky (clf = 0–0.1), partly cloudy-sky (clf = 0.2–0.8), and overcast (clf = 0.9–1).

Figure 4.3a shows the occurrence of the wintertime clf (0–1) obtained at JMA Sapporo from 2005 to 2015. The most frequently occurring sky condition during the wintertime was overcast (43%). On the other hand, the occurrence of clear-sky conditions was only 2%. During March (the characteristics of snow ablation during March is investigated in Sect. 4.3.3), the occurrence of clf (Fig. 4.3b) documents almost have the same features as those obtained during the whole winter period (Fig. 4.3a). The occurrences of overcast and clear-sky conditions were 47 and 1%, respectively. The reason why overcast conditions were frequently observed at Sapporo is that it is located in the southwest part of Hokkaido in Japan, facing the Sea of Japan, and it is continuously exposed to the cold winter north-westerly monsoon during most of the winter period. The average clf during each winter period (December to March for the 10 years) did not show a significant increasing nor decreasing trend: it remained at 0.7 or 0.8 every year. This result supports the discussion by Kudo et al. (2012) mentioned above. Also, significant seasonal variation was not found during the period (each monthly-mean clf from December to March was 0.8) (Table 4.1).

#### **4.2.3. Snow pit measurements**

At the Sapporo AWS, standard snow pit measurements following the Japanese Society of Snow and Ice (2010) were conducted twice a week at about 1100 JST during the 2005–2015 winters. Manually measured snow physical properties employed in this study are SWE, profiles for snow density,

temperature, and grain shape. The classification method for snow grain shape was adapted from that established by Fierz et al. (2009).

#### 4.2.4. Numerical simulation with the SMAP model

The latest version of a one-dimensional multi-layered physical snowpack model SMAP (Niwano et al., 2014) was used to calculate the temporal evolution of seasonal snow internal physical properties (including runoff rate of meltwater examined in this study) as well as the snow SEB:

$$S_{net} + L_{net} + H_S + H_L + H_R + H_G = Q_{net} , \quad (4.2)$$

where,  $S_{net}$ ,  $L_{net}$ ,  $H_S$ ,  $H_L$ ,  $H_R$ ,  $H_G$ , and  $Q_{net}$  are the net shortwave radiant flux, net long-wave radiant flux, sensible heat flux, latent heat flux, heat supply by rainfall, subsurface conductive heat flux, and net energy flux, respectively. These fluxes are defined to be positive when they are directed into the snow surface. If  $Q_{net}$  is positive, the surface is heated and surface melt can be induced if the snow surface temperature is 0 °C.

The SMAP model adopts a one-dimensional energy balance equation as the main governing equation of the snowpack, where the solar heating of the snowpack and melt-freeze cycles are taken into account (Niwano et al., 2012). In the latest version (Niwano et al., 2014), vertical water percolation is now calculated using the Richards equation (Richards, 1931). In addition, the viscosity coefficient of snow is calculated using the scheme presented by Vionnet et al. (2012) and an upper bound of 0.1 on the Richardson number (an indicator of the near-surface atmospheric stability condition) is set to ensure small but non-zero turbulent heat exchanges under very stable conditions. Snow grain shape classification is performed following the approach developed by the SNOWPACK model (Lehning et al., 2002a). In the present study, the SMAP model was driven by the 30 min averaged meteorological properties from November to April introduced in Sect. 4.2.1: snow depth,



air temperature, relative humidity, wind speed, downward shortwave and long-wave radiant fluxes, snow surface albedo, and ground surface soil heat flux. Additionally, 30 min accumulated liquid rainfall was inputted to force the model because the air temperature at Sapporo sometimes rose above 0 °C even during the accumulation period, and consequently, rain-on-snow events occurred frequently (Niwano et al., 2012). Liquid rainfall was obtained from the observed precipitation by partitioning it into snow and rain following the method by Yamazaki (2001). Related to the radiation process of the snowpack, the snow albedo is determined from in-situ measurements, and the solar heating profile in the snowpack is calculated using the PBSAM module as functions of the internally calculated optically equivalent snow grain size and externally given mass concentrations of snow impurities (Sect. 4.1). At Sapporo, fully quality-controlled data for near-surface mass concentrations of black carbon and mineral dust from 2007 to the present (Kuchiki et al., 2015) were processed; however, information for the period during the 2005–2007 winters were not available. Therefore, in the present study, monthly-averaged mass concentrations of black carbon and mineral dust presented by Kuchiki et al. (2015) was prescribed as a constant model parameter throughout each ten winter season in order to maintain consistency in the procedures of the numerical calculations.

In the SMAP model calculation, the snowpack is divided into several model snow layers, where each model layer thickness  $d$  is allowed to range between  $d_{min}$  and  $d_{max}$ . In the present study,  $d_{min}$  and  $d_{max}$  were set as 1.5 cm and 0.5 cm, respectively. The time step of the numerical integration was set as 50 sec. The snow surface roughness length for momentum was set to be constant at 0.23 mm, which was obtained by Kondo and Yamazawa (1986) for seasonal snow. Using this value, roughness lengths for heat and moisture were diagnosed following Andreas (1987). New snow density was calculated by using a parameterization as a function of wind speed (Yamazaki 2001; Niwano et al., 2012), which was well validated under the climate conditions at Sapporo. As for the effective

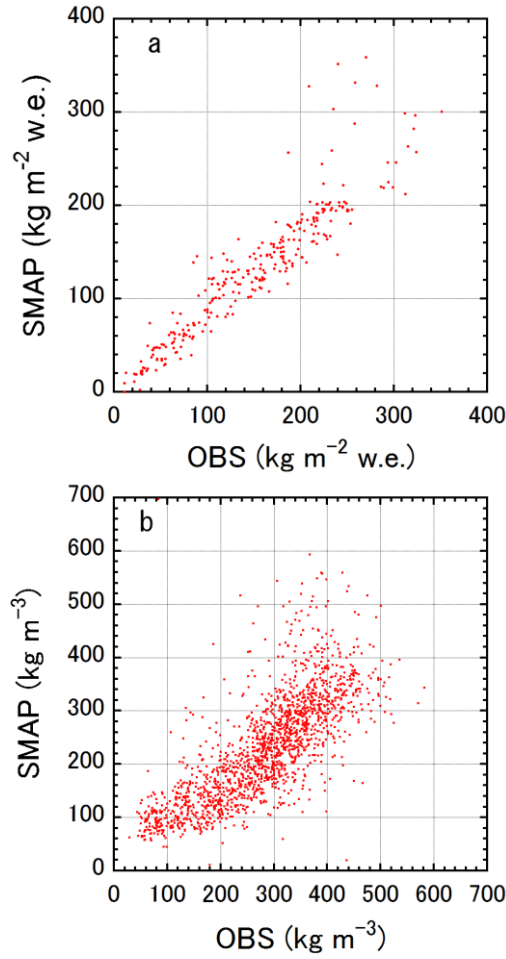


**Figure 4.4.** Comparisons of the observed and simulated (a) column-integrated SWE and (b) the snow density profiles at Sapporo during the 2005–2015 winters. Observed SWE and snow density profiles were obtained from snow pit measurements.

thermal conductivity of snow, a parameterization by Devaux (1933) was chosen. At Sapporo, this parameterization works reasonably, as demonstrated by Yamazaki (2001) and Niwano et al. (2012).

The validity of the SMAP model calculation was evaluated in terms of the column-integrated snow water equivalent (SWE), snow density profile, snow surface temperature, and snow temperature profile (Sect. 4.3.1) in advance of analyses of the snow SEB (Sect. 4.3.2) and modeled meltwater runoff (Sect. 4.3.3). Investigations on the snow SEB (Sect. 4.3.3) and modeled meltwater

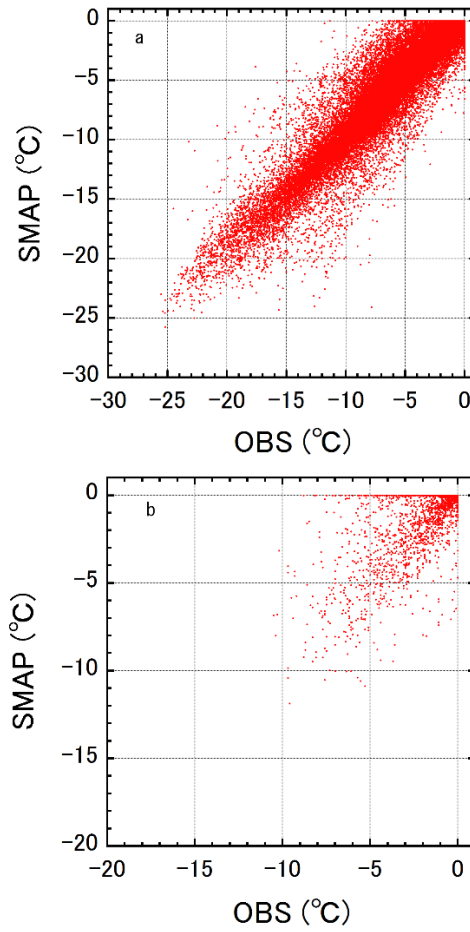
runoff (Sect. 4.3.4) were conducted by using daily-mean simulation results by the SMAP model together with the daily-mean measurement data mentioned above.

### **4.3. Results and discussion**

#### **4.3.1. Model evaluation**

In this section, the performance of the SMAP model simulating the mass and energy balances of the snowpack is evaluated using the data obtained during the 2005–2015 winters at Sapporo. The accuracy of the simulated mass balance of the snowpack is assessed in terms of the SWE and snow density profile. On the other hand, the calculated energy balance of the snowpack is evaluated from the standpoint of the snow surface temperature and snow temperature profile.

A 10-year comparison of the column-integrated SWE (Fig. 4.4a; total 273 in-situ data were available) revealed that the model tended to underestimate by  $-19 \text{ kg m}^{-2}$  w.e. (ME; mean error is defined as the average of the difference between the simulated and observed values), and the obtained RMSE (root mean square error) was  $34 \text{ kg m}^{-2}$  w.e. This means that the column-integrated snow density can be underestimated as well. Niwano et al. (2014) reported the performance of the latest version of the SMAP model forced by precipitation, where model validation was performed at Sapporo during the 2007–2009 winters using the same data as employed in this study. During the two winters, the performance of the SMAP model forced by precipitation and snow depth with liquid rainfall were  $-36$  and  $-31 \text{ mm}$  for ME, and  $47$  and  $39 \text{ mm}$  for RMSE, respectively. This result indicates that a better performance of simulating SWE could be obtained in a case where the model was forced by snow depth with liquid rainfall compared to a case where the model was driven by precipitation only. This implies that the SMAP model simulated the mass balance of the snowpack adequately during the study period. The same tendency was also reported by Wever et al. (2015) for the SNOWPACK model, suggesting that the correction technique for measured precipitation (Sect. 4.2.1) is still insufficient and should be improved.



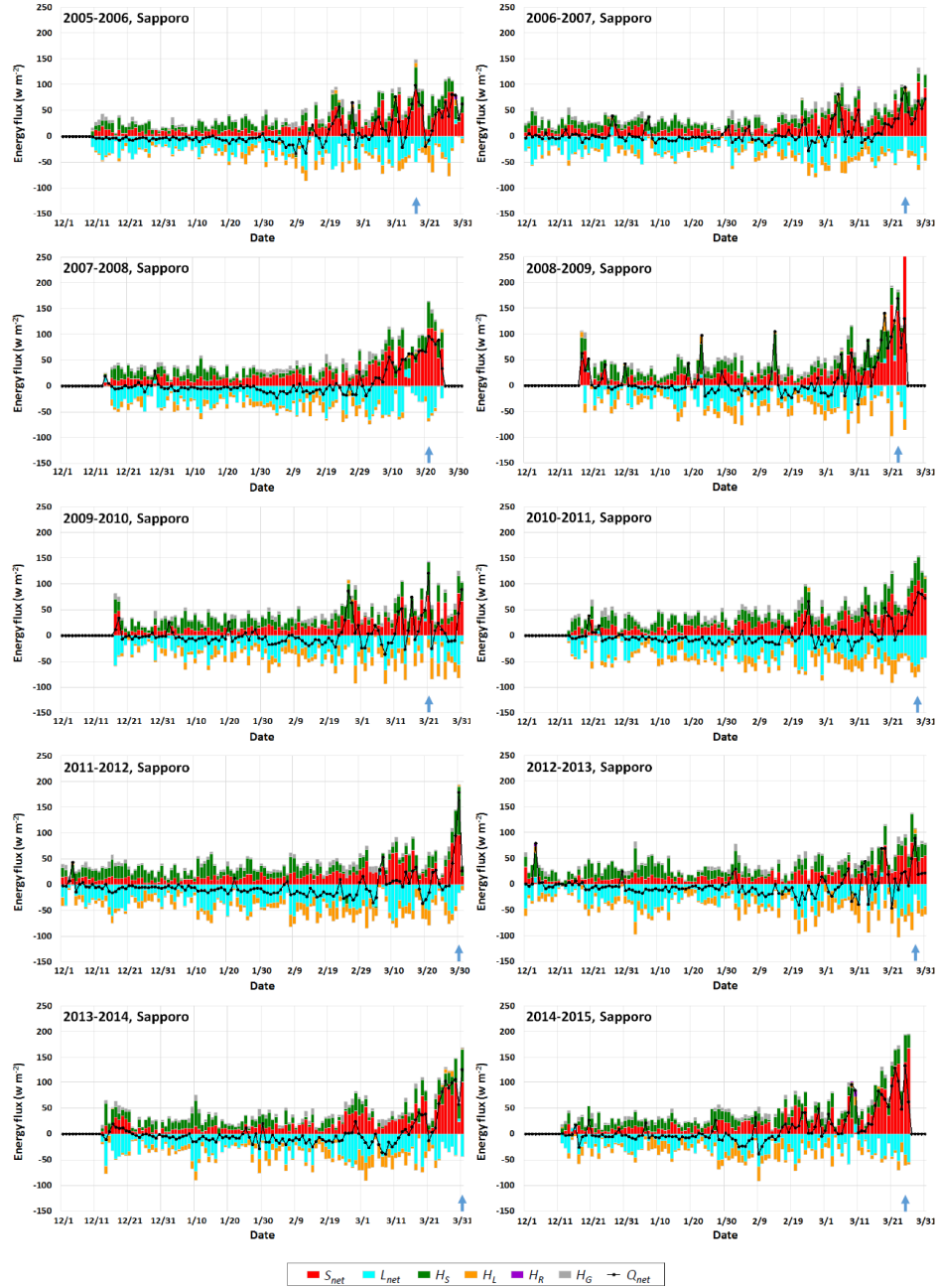
**Figure 4.5.** Comparisons of the observed and simulated (a) 30 min interval snow surface temperature measured by the AWS and (b) snow temperature profiles obtained from snow pit measurements performed twice a week at the Sapporo during the 2005–2015 winters.

Figure 4.4b compares the observed and calculated snow density during the study period. A total number of 1688 measured profiles of snow density were available for this comparison. For reference, Figs. 4.S1 and 4.S2 in the supplementary information of this paper display the SMAP model-simulated snow density for the 2005–2010 and 2011–2015 winters, respectively. As suggested by the comparison of the observed and simulated SWE, the model tended to underestimate snow density (ME was  $-51 \text{ kg m}^{-3}$ ) in almost the entire range of observed snow density. The obtained

RMSE was  $88 \text{ kg m}^{-3}$ . As the temporal evolution of snow density is simulated by a densification equation in the SMAP model (Niwano et al., 2012), new snow density, which is calculated by a simple parameterization as a function of the surface meteorological conditions (Sect. 4.2.4) at present, should be improved. The physical characteristics of this type of parameterization strongly reflect the climate conditions in which the parameterization was developed. As a result, once climate conditions change, the reliability of the scheme can be significantly lowered, even in the same location as where the scheme was developed. Therefore, a physically based scheme for new snow density that can be applied to the global climate condition should be developed.

In order to check the validity of the model calculations on energy exchanges between the snow surface and the atmosphere, 30 min interval simulated snow surface temperatures were compared against in-situ measurements. Figure 4.5a compares the observed and simulated snow surface temperature during the study period, where neither systematic or considerable overestimation nor underestimation were found ( $\text{ME} = 0.4 \text{ }^{\circ}\text{C}$ ). As the obtained RMSE was also at a sufficiently reasonable level ( $1.6 \text{ }^{\circ}\text{C}$ ) of this type of SEB study (e.g., van den Broeke et al., 2011; Cullen et al., 2014), it was confirmed that the SEB analysis could be performed using the results from the SMAP model simulations.

In the model, snow temperature is mainly affected by snow density through the effective thermal conductivity of snow (Niwano et al., 2012). RMSE for snow density during the 10 years ( $88 \text{ kg m}^{-3}$ ) resulted in a ME of  $0.4 \text{ }^{\circ}\text{C}$  and a RMSE of  $1.6 \text{ }^{\circ}\text{C}$  for snow temperature (Fig. 4.5b). A total number of 2562 measured profiles of snow temperature were available for this comparison. These scores were almost the same as those for the case of snow surface temperature mentioned above. Figs. 4.S1 and S2 in the supplementary information show the temporal evolution of the simulated snow temperature profiles for the 2005–2010 and 2011–2015 winters, respectively. A slight overestimation of the snow temperature would be caused by an underestimation of snow density, because the



**Figure 4.6.** 10-year record of the daily-mean snow SEB at Sapporo: Temporal changes in the net shortwave radiant flux ( $S_{net}$ ), net long-wave radiant flux ( $L_{net}$ ), sensible heat flux ( $H_S$ ), latent heat flux ( $H_L$ ), heat supply by rainfall ( $H_R$ ), subsurface conductive heat flux ( $H_G$ ), and the net energy flux ( $Q_{net}$ ) are shown. Blue vertical arrows indicate the days when the largest  $Q_{net}$  were recorded during each winter season.

modeled insulation effect of the snowpack during the period when the snow SEB was negative (the snow surface is cooled) could be enhanced. In order to reduce the uncertainties in the model performance regarding snow temperature calculation, increasing the accuracy of the snow density is necessary above all. In addition to this, the development of a physically based scheme for the effective thermal conductivity of snow is also necessary, because the present parameterization as a function of snow density (Sect. 4.2.4) has the same problem as mentioned above regarding the parameterization for new snow density.

### 4.3.2. Snow surface energy balance

The daily-mean wintertime snow SEB during the study period at Sapporo was investigated and is shown Fig. 4.6. Table 4.1 lists the 10-year averaged monthly-mean snow SEB. As compiled by Armstrong and Brun (2008), Giesen et al. (2009), and Cullen and Conway (2015), the signs and magnitudes of the SEB components in the left-hand side of Eq. 4.2 differ significantly depending on the climatic conditions. At Sapporo,  $S_{net}$ ,  $H_S$ , and  $H_G$  tended to heat the snow surface, while  $L_{net}$  and  $H_L$  played a role in cooling the surface in general. Although rain-on-snow events often occurred at Sapporo,  $H_R$  can be neglected practically. However, it should be kept in mind that the effects of rainfall on the thermal regime of the snowpack are very important, because the release of latent heat due to the refreezing of rainfall (and of course, melt water) significantly warms the snowpack (e.g., Phillips et al., 2010). During December and January,  $H_S$  was the main contributor to surface heating, while it was superseded by  $S_{net}$  after February. On the other hand,  $L_{net}$  was the main contributor to surface cooling continuously throughout the wintertime. The monthly-mean  $Q_{net}$  was very small (around  $0 \text{ W m}^{-2}$ ) during December and became negative during the rest of accumulation period. After the ablation period, it increased rapidly in accordance with the increases in  $S_{net}$  and  $H_S$ . At Sapporo, the seasonally maximum  $Q_{net}$  (i.e., seasonally maximum surface heating) was recorded late in March (after March 20; they are indicated in Fig. 4.6 with blue vertical arrows) except for the

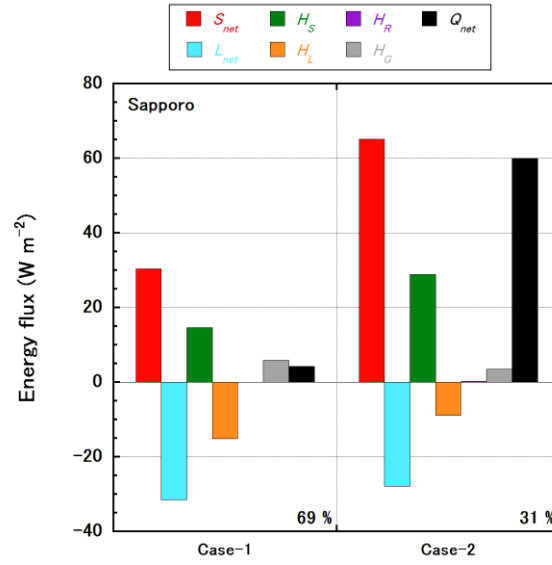


**Figure 4.7.** Daily-mean snow SEB averaged from March 1 to 25 at Sapporo during the 2005–2015 winters. The snow SEB is categorized and averaged for two cases: Case-1 (daily runoff rate was less than  $7 \text{ kg m}^{-2} \text{ w.e. day}^{-1}$ ) and Case-2 (daily runoff rate was more than  $7 \text{ kg m}^{-2} \text{ w.e. day}^{-1}$ ). The occurrence of each case (%) is indicated together.  $S_{net}$ ,  $L_{net}$ ,  $H_S$ ,  $H_L$ ,  $H_R$ ,  $H_G$ , and  $Q_{net}$  denote the net shortwave radiant flux, net long-wave radiant flux, sensible heat flux, latent heat flux, heat supply by rainfall, subsurface conductive heat flux, and net energy flux, respectively.

2005–2006 winter, in which it was recorded on March 17. In accordance with the seasonal transition in the snow SEB, dry snow grain shapes were often measured on site until around the beginning of March; however, isothermal wet snow suddenly prevailed in the entire snowpack afterward. This situation was successfully reproduced by the SMAP model (Figs. 4.S3 and 4.S4 in the supplementary information). Once the entire snowpack consisted of wet snow, ablation due to meltwater runoff from snowpack accelerated drastically.

#### 4.3.3. Modeled meltwater runoff rate

In this section, we investigate the factors controlling the (daily-accumulated) modeled meltwater runoff rate ( $\text{kg m}^{-2} \text{ w.e. day}^{-1}$ ) at Sapporo during the ablation period. As shown in Fig. 4.6, melting



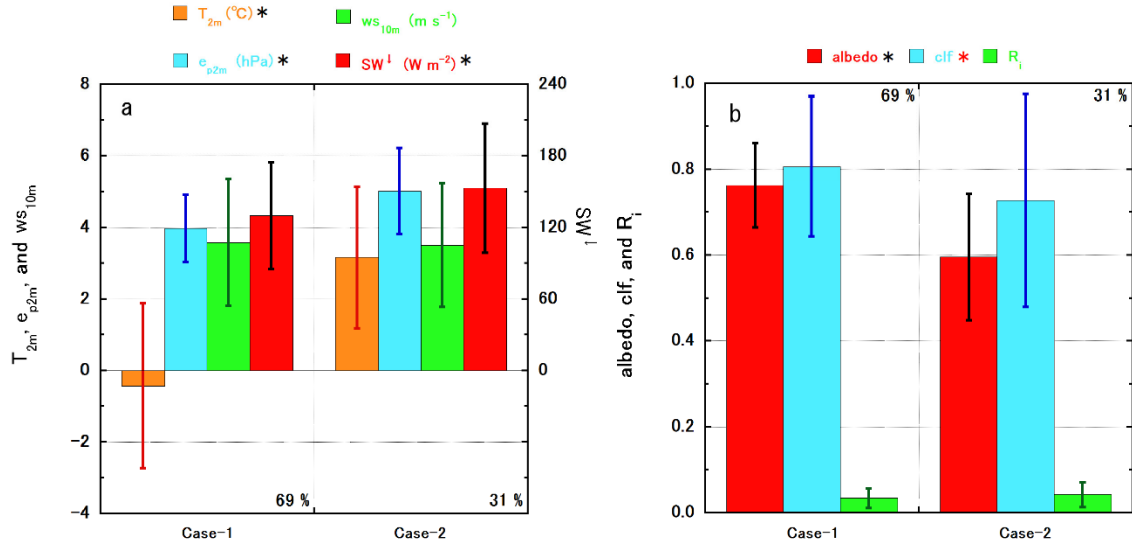


**Figure 4.8.** The daily-mean 2 m air temperature ( $T_{2m}$ ), 2 m vapor pressure ( $e_{p2m}$ ), 10 m wind speed ( $ws_{10m}$ ), downward shortwave radiant flux ( $SW^{\downarrow}$ ), albedo, cloud fraction ( $clf$ ), and the Richardson number ( $R_i$ ) for Case-1 (daily runoff rate was less than  $7 \text{ kg m}^{-2} \text{ w.e. day}^{-1}$ ) and Case-2 (daily runoff rate was more than  $7 \text{ kg m}^{-2} \text{ w.e. day}^{-1}$ ). The vertical lines indicate the standard deviations for each property. Those properties with a black asterisk indicate that average values between the two categories are significantly different ( $p < 0.01$  by a T-test). A red asterisk denotes that the difference in a condition between the two categories is statistically significant (see text).

was often completed before March 25. Therefore, this analysis was focused from March 1 to 25 every year. During the 10 years, the SMAP model simulated that runoff was caused every day (i.e., a total of 250 days), and estimated that the average daily-mean runoff rate was  $7 \text{ kg m}^{-2} \text{ w.e. day}^{-1}$ . The total number of days when meltwater runoff rate was below average was 173 (69%).

Figure 4.7 compares the characteristics of the snow SEB when the runoff rate was reduced (less than  $7 \text{ kg m}^{-2} \text{ w.e. day}^{-1}$ ; this case is referred to as “Case-1”) or increased (more than  $7 \text{ kg m}^{-2} \text{ w.e. day}^{-1}$ ; “Case-2”). Clearly, meltwater runoff was enhanced when the snow surface was heated

sufficiently (Case-2; average  $Q_{net}$  was  $60 \text{ W m}^{-2}$ ). In this case, increments of  $S_{net}$ ,  $H_s$ , and  $H_L$  from Case-1 (+35, +14, and +6  $\text{W m}^{-2}$ , respectively) contribute mainly to the increase in  $Q_{net}$  (+56  $\text{W m}^{-2}$ ). The differences in these energy fluxes for both cases were statistically significant ( $p < 0.01$  by the T-test). On the other hand,  $L_{net}$  and  $H_G$  indicated almost the same order for both cases.

$S_{net}$  are modulated by downward shortwave radiant flux, clf, and albedo, while turbulent heat fluxes are controlled by 2 m air temperature and vapor pressure, 10 m wind speed, and the Richardson number. Therefore, the average values of these properties for both Case-1 and Case-2 conditions were examined (Fig. 4.8). In Case-2, it was found that the downward shortwave radiant flux was larger and albedo was smaller compared to Case-1 significantly ( $p < 0.01$  by T-test) (Figs. 4.8a and 8b). As for clf, the average value during Case-2 (0.7) was smaller than that for Case-1 (0.8); however, this difference was not statistically significant. In Case-2, the standard deviation of clf was much larger compared to that for Case-1 (Fig. 4.8b), suggesting that an increased runoff rate could be achieved under a wide range of clf. In fact, the maximum modeled runoff rate during the study period ( $108 \text{ kg m}^{-2} \text{ w.e. day}^{-1}$ ) was recorded under overcast conditions (clf = 1) on March 10, 2015. As the second largest modeled runoff rate during the 10 years was  $31 \text{ kg m}^{-2} \text{ w.e. day}^{-1}$  (March 21, 2010), it was an exceptional flooding event. On March 10, 2015, the total precipitation rate reached  $93 \text{ kg m}^{-2} \text{ w.e. day}^{-1}$  (rainfall and snowfall rates were 68 and  $25 \text{ kg m}^{-2} \text{ w.e. day}^{-1}$ , respectively), implying that the exceptional flooding event was caused by a heavy rain-on-snow event. If this event was excluded from the analysis, a statistically significant difference in clf could be obtained (the average clf values were still 0.8 and 0.7 for Case-1 and Case-2, respectively). Regarding the properties related to the turbulent heat fluxes, the average 10 m wind speed and the Richardson number were almost in the same order between Case-1 and Case-2 (Figs. 4.8a and 4.8b); however, significant differences in the 2 m air temperature and vapor pressure were found. Overall, it can be summarized that the characteristics of Case-2 were an increased downward shortwave radiant flux, 2

m air temperature and vapor pressure, as well as a decreased albedo and  $\text{clf}$ . The average values for these properties in Case-2 were  $153 \text{ W m}^{-2}$ ,  $3.2 \text{ }^{\circ}\text{C}$ ,  $5.0 \text{ hPa}$ ,  $0.60$ , and  $0.7$ , respectively. Their differences against the monthly-mean values listed in Table 4.1 were  $10 \text{ W m}^{-2}$ ,  $2.0 \text{ }^{\circ}\text{C}$ ,  $0.6 \text{ hPa}$ ,  $-0.10$ , and  $-0.1$ , respectively. These suggest that sunny weather conditions in the daytime, which can cause surface heating and a resultant albedo reduction through snow grain growth by wet snow metamorphism, was an ideal condition for increases in the  $Q_{\text{net}}$  and subsequent meltwater runoff during the study period at Sapporo.

#### 4.4. Conclusions

We investigated the factors controlling ablation from the snowpack at Sapporo during the 2005–2015 winters (December to March) from the standpoint of the snow SEB by employing fully quality-controlled meteorological and snow data. In order to calculate the daily-mean snow SEB and resultant meltwater runoff rate, a physical snowpack model SMAP was driven by the 30 min averaged meteorological properties including snow depth, air temperature, relative humidity, wind speed, downward shortwave and long-wave radiant fluxes, snow surface albedo, ground surface soil heat flux, and 30 min accumulated liquid rainfall. The SMAP model was evaluated in terms of SWE, snow density profile, snow surface temperature, and snow temperature profile, and it was confirmed that the model simulated the energy and mass balances of the snowpack realistically. The calculated snow SEB indicated that the  $S_{\text{net}}$ ,  $H_S$ , and  $H_G$  tended to heat the snow surface, while the  $L_{\text{net}}$  and  $H_L$  played a role in cooling the surface in general. During December and January,  $H_S$  was the main contributor for the surface heating, while it was superseded by  $S_{\text{net}}$  after February. On the other hand,  $L_{\text{net}}$  was the dominant energy flux that cooled the snow surface continuously throughout the wintertime. The resultant  $Q_{\text{net}}$  was below  $0 \text{ W m}^{-2}$  until February; however, it increased drastically in March as a result of increases in  $S_{\text{net}}$  and  $H_S$ . Based on this consideration, the characteristics of the modeled meltwater runoff were investigated only during March in the present study. In this process,

the physical conditions of the snowpack and atmosphere under the following two cases, Case-1 (daily-mean meltwater runoff rate was below average during March:  $7 \text{ kg m}^{-2} \text{ w.e. day}^{-1}$ ) and Case-2 (daily-mean meltwater runoff rate was larger than average), were examined. Comparison of the snow SEB between Case-1 and Case-2 showed that the meltwater runoff was enhanced (Case-2) under the higher  $Q_{net}$  condition (difference in  $Q_{net}$  between these two cases was  $+60 \text{ W m}^{-2}$ ). The difference could be attributed mainly to changes in  $S_{net}$ ,  $H_S$ , and  $H_L$  ( $+35$ ,  $+14$ , and  $+6 \text{ W m}^{-2}$ , respectively). As these fluxes are affected by the downward shortwave radiant flux,  $clf$ , albedo, 2 m air temperature and vapor pressure, 10 m wind speed, and the Richardson number, differences in these properties for Case-1 and Case-2 were explored further. As a result, statistically significant differences were found for the downward shortwave radiant flux, 2 m air temperature and vapor pressure, albedo, and  $clf$ . The average values of these properties in Case-2 were higher (or lower) than each monthly average by  $10 \text{ W m}^{-2}$ ,  $2.0 \text{ }^{\circ}\text{C}$ ,  $0.6 \text{ hPa}$ ,  $(0.10)$ , and  $(0.1)$ , respectively. Therefore, we concluded that a sunny weather condition in the daytime, which can induce surface heating and resultant albedo reduction through snow grain growth via wet snow metamorphism, was the ideal condition for enhanced meltwater runoff during the study period at Sapporo.

### **Acknowledgements**

We sincerely appreciate Teppei J. Yasunari, Masahiro Takahashi, Yuki Sawada, Tomoyasu Kuno, Kou Shimoyama, Taro Nakai, Tetsuo Sueyoshi, Shun Tsutaki, Tsutomu Watanabe, Hayato Oka, Kazuhiro Okuzawa, Junko Mori, Tatsuya Nakayama, Hirokazu Hirano, Chusei Fujiwara, Niyi Sunmonu, Kohei Otomo, Masaki Okuda, Makoto Shimamura, Takehiro Fukuda, Akane Tsushima, Kenta Tone, Hirotaka Sasaki, Momoko Nakayama, Ikumi Oyabu, Yukito Hayashi, Kosuke Tsubokura, Naoya Kanna, Daisuke Nishimura, Takako Saeki, Satoshi Yoshida, Shiho Sato, Daiki Sakakibara, Satoshi Matsuno, Satoshi Omiya, Nobuyoshi Konishi, Takeshi Ishikawa, Masahiro Minowa, Yoshinori Iizuka, and Etsuko Tanaka for the snow pit work at the Institute of Low

Temperature Science, Hokkaido University. We thank Kazuyoshi Suzuki (JAMSTEC) for supporting precipitation measurements with the GEONOR rain gauge at the Sapporo AWS, and Masae Igosaki (Meteorological Research Institute) for helping the Sapporo AWS data processing. This study was supported in part by (1) the Japan Society for the Promotion of Science (JSPS), Grant-in-Aid for Scientific Research (A), number 16H01772, (2) the Grant for Joint Research Program, the Institute of Low Temperature Science, Hokkaido University, (3) the Japan Society for the Promotion of Science (JSPS), Grant-in-Aid for Scientific Research (A), number 15H01733, (4) the Japan Society for the Promotion of Science (JSPS), Grant-in-Aid for Scientific Research (S), number 23221004, (5) the Experimental Research Fund for Global Environment Conservation, the Ministry of the Environment of Japan, and (6) the Global Change Observation Mission - Climate (GCOM-C) / the Second-generation GLobal Imager (SGLI) Mission, the Japan Aerospace Exploration Agency (JAXA).

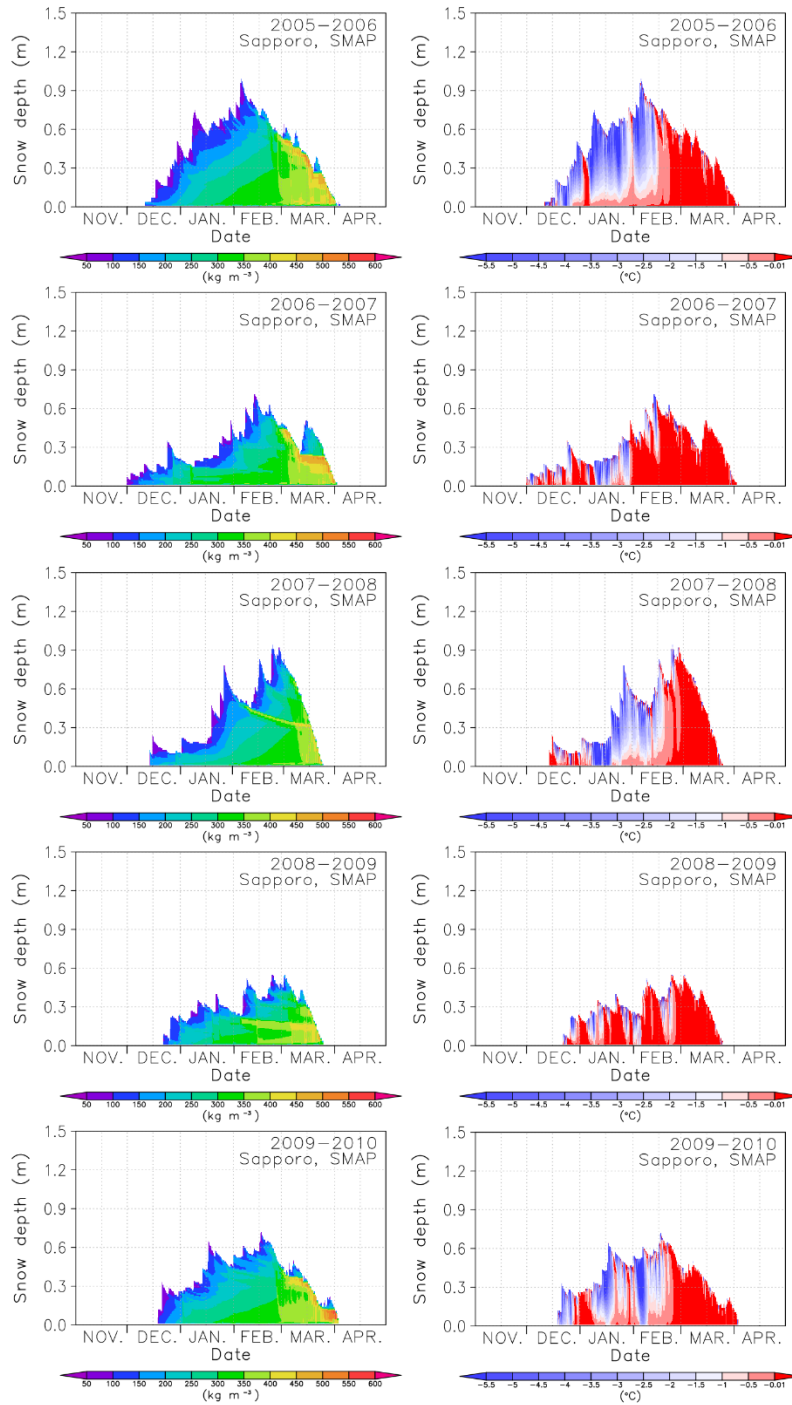


**Figure 4.S1.** Temporal evolution of snow density (left row) and snow temperature (right row) at Sapporo, simulated with the SMAP model from 2005 to 2010.

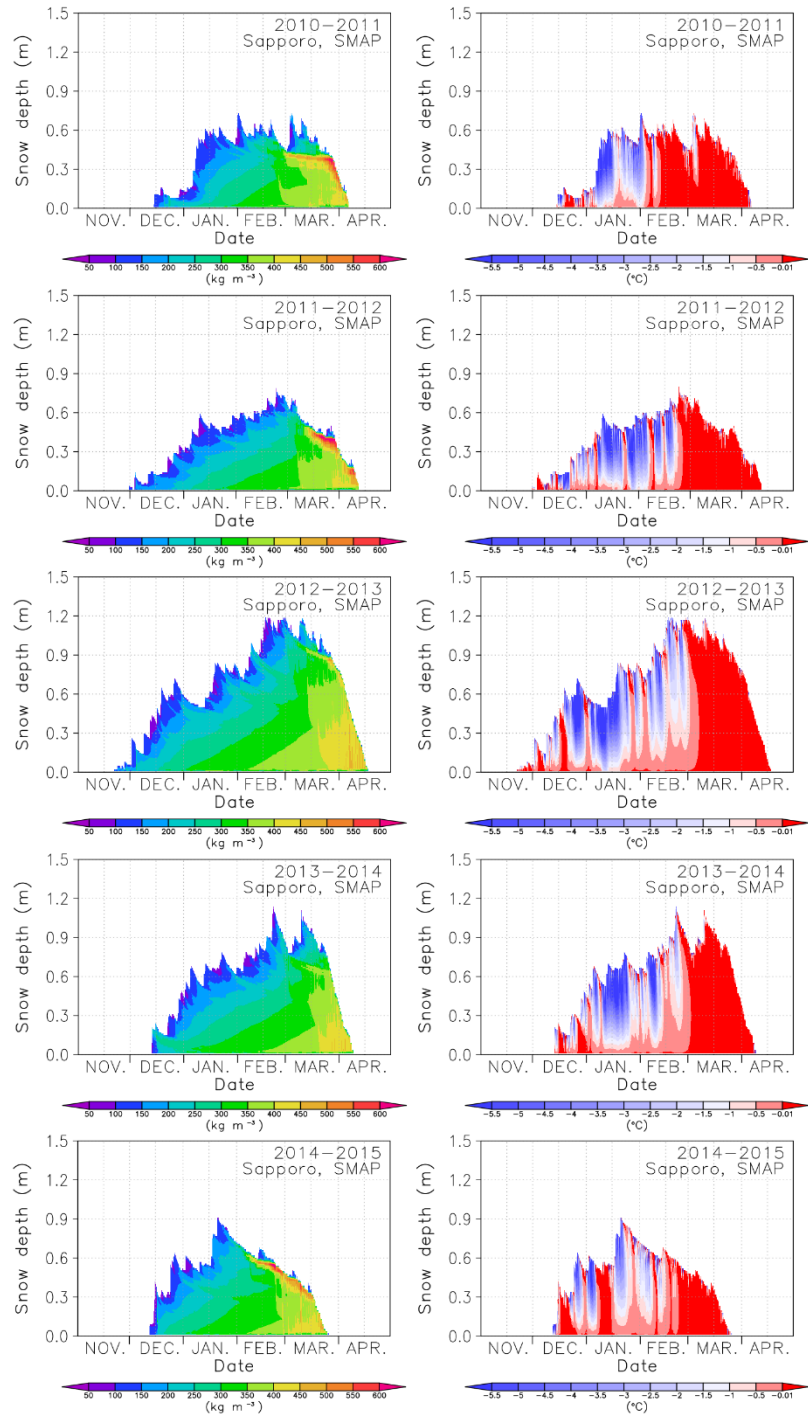


**Figure 4.S2.** Temporal evolution of snow density (left row) and snow temperature (right row) at Sapporo, simulated with the SMAP model from 2011 to 2015.

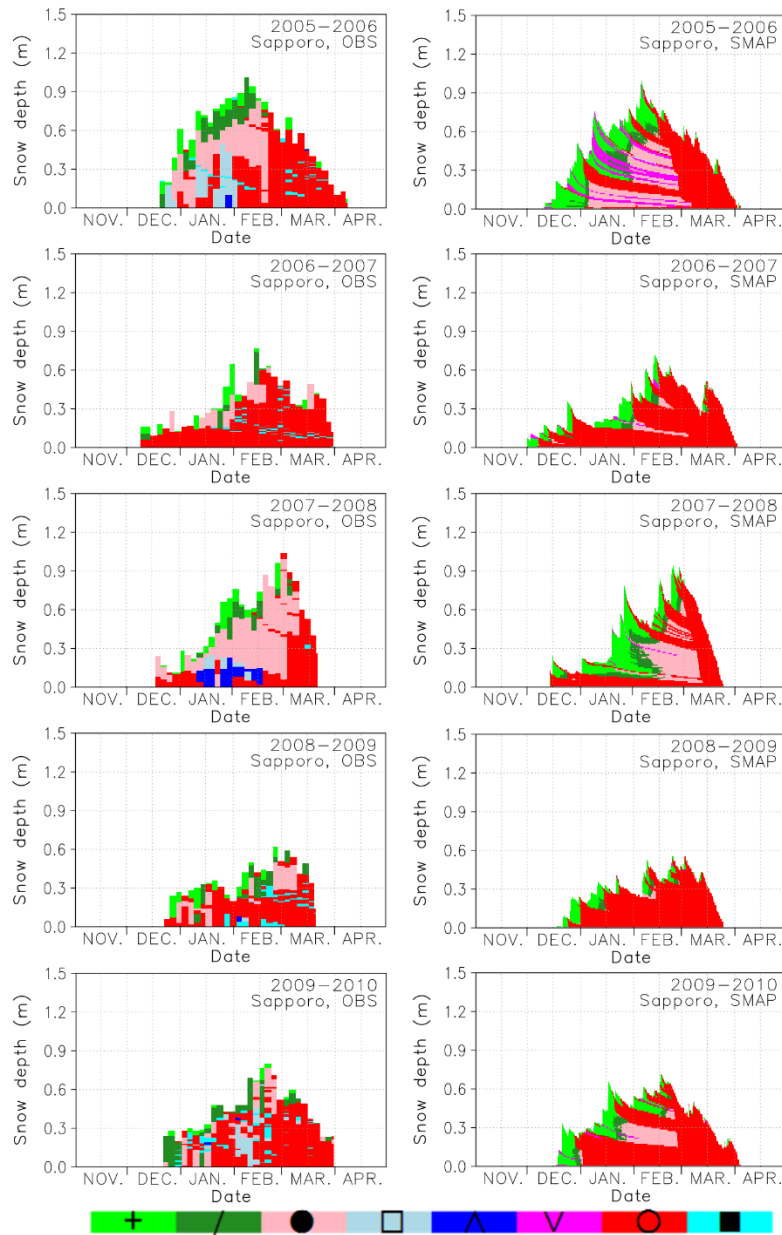


**Figure 4.S3.** Observed (left row) and simulated (right row) major snow grain shapes at Sapporo from 2005 to 2010. The characters and colors indicating snow grain shape follow the definitions by Fierz et al. (2009). In sequence from the left they denote the precipitation particles, decomposing and fragmented precipitation particles, rounded grains, faceted crystals, depth hoar, surface hoar, melt forms, and ice layer. The observed snow grain shapes are illustrated only for the days when snow pit measurements were conducted.



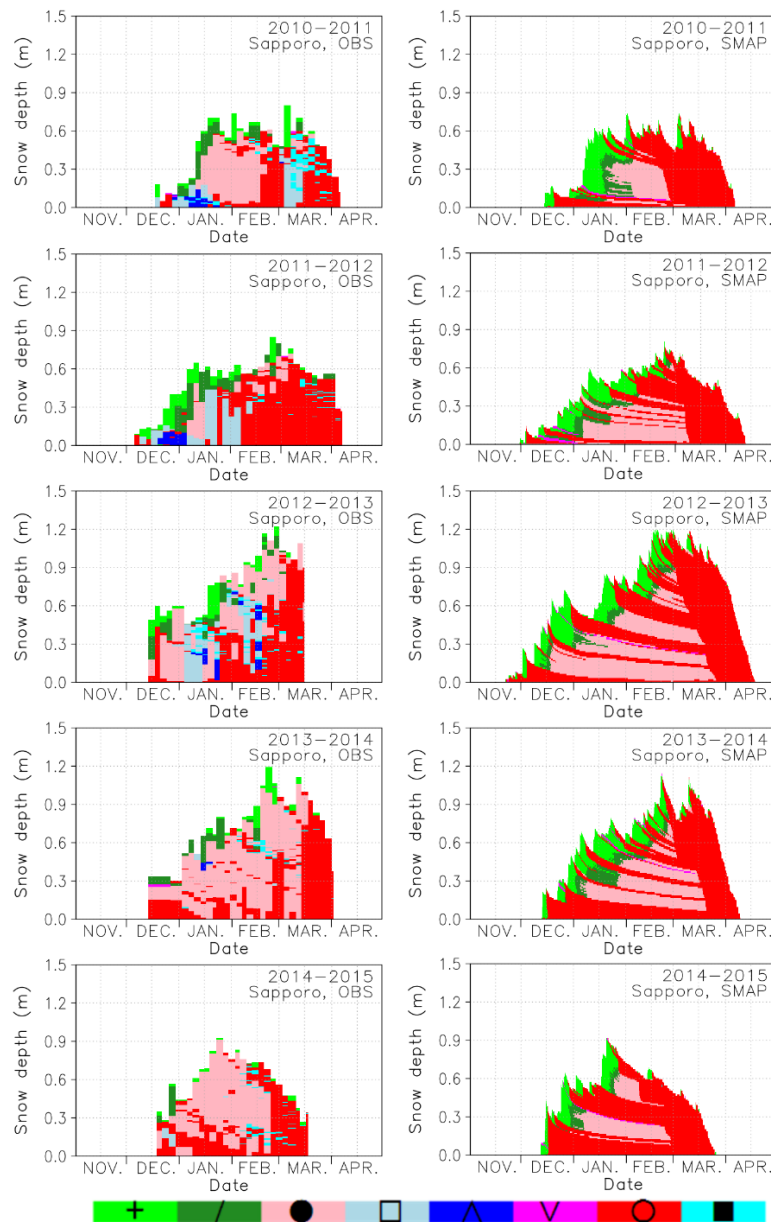


**Figure 4.S4.** Observed (left row) and simulated (right row) major snow grain shapes at Sapporo from 2011 to 2015. The characters and colors indicating snow grain shape follow the definitions by Fierz et al. (2009). In sequence from the left they denote the precipitation particles, decomposing and fragmented precipitation particles, rounded grains, faceted crystals, depth hoar, surface hoar, melt forms, and ice layer. The observed snow grain shapes are illustrated only for the days when snow pit measurements were conducted.

## 5. Application of the SMAP model to the Greenland ice sheet

Published in *The Cryosphere*, **9**, 971–988, doi:10.5194/tc-9-971-2015, 2015, entitled as “**Numerical simulation of extreme snowmelt observed at the SIGMA-A site, northwest Greenland, during summer 2012**”.

**M. Niwano<sup>1</sup>, T. Aoki<sup>1</sup>, S. Matoba<sup>2</sup>, S. Yamaguchi<sup>3</sup>, T. Tanikawa<sup>4, 6</sup>, K. Kuchiki<sup>1</sup>, and H. Motoyama<sup>5</sup>**

<sup>1</sup> Meteorological Research Institute, Japan Meteorological Agency

<sup>2</sup> Institute of Low Temperature Science, Hokkaido University

<sup>3</sup> Snow and Ice Research Center, National Research Institute for Earth Science and Disaster Prevention

<sup>4</sup> Earth Observation Research Center, Japan Aerospace Exploration Agency

<sup>5</sup> National Institute of Polar Research

<sup>6</sup> Now at Meteorological Research Institute, Japan Meteorological Agency

### 5.1. Introduction

Snow and ice on the Greenland ice sheet (GrIS) experienced a record near-surface melt extent in summer 2012 (*Nghiem et al.*, 2012; *Tedesco et al.*, 2013; *Hall et al.*, 2013; *Hanna et al.*, 2014; *Bennartz et al.*, 2013). The physical conditions of the atmosphere and the snow (as well as ice) surface during summer 2012 have been gradually clarified. The most notable feature of the event is that the extent of surface melt was the largest in the satellite era (March 2000 to the present).

According to several studies that used satellite data (*Nghiem et al.*, 2012; *Tedesco et al.*, 2013; *Hall et al.*, 2013), at least 95% of the entire surface of the GrIS melted during the period 30 June to 14 July 2012. At present, it is hypothesized that a significant temperature increase over the GrIS may have been a major cause of the record near-surface melt event. *Hall et al.* (2013) examined the ice surface temperature (IST) of the GrIS derived from the Moderate-resolution Imaging Spectroradiometer (MODIS) and concluded that the 2012 summer was the warmest (IST:  $-6.38 \pm 3.98$  °C) in the MODIS record. *Bennartz et al.* (2013) have demonstrated that low-level clouds

consisting of liquid-water droplets played a key part in the melt event by increasing near-surface temperature via radiative effects. *Nghiem et al.* (2012) pointed out the existence of an anomalous ridge of warm air that could be identified by a 500 hPa height anomaly, and they concluded that the ridge acted as a strong heat dome that became stagnant over the GrIS during the period. *Hanna et al.* (2014) concluded that the extreme melt was forced mainly by atmospheric conditions linked with changes in the summer North Atlantic Oscillation (NAO), Greenland Blocking Index, and polar jet stream. The combination of these conditions favored southerly warm air advection along the western coast. According to *Fettweis et al.* (2013), the frequency of occurrence of anticyclones centered over the GrIS at the surface and at 500 hPa has doubled since the end of the 1990s. They associated this increased frequency with an increase of negative phases of the NAO, which induce more frequent southerly warm air advection along the western Greenland coast and over the neighboring Canadian Arctic Archipelago.

However, a temperature increase cannot induce surface melt if the surface temperature, which is physically controlled by the surface energy balance (SEB), is below 0 °C. The SEB is equal to the sum of the net shortwave radiant flux, net long-wave radiant flux, sensible heat flux, latent heat flux, heat supply by rainfall, and subsurface conductive heat flux (*Armstrong and Brun*, 2008). In this study, these fluxes are defined to be positive when they are directed towards the snow surface, and a positive sum of these fluxes (net energy flux) induces surface melt only if the surface temperature equals 0 °C. A temperature increase raises the net energy flux mainly by affecting the sensible heat flux, although other energy fluxes, especially net long-wave radiant flux, can of course be affected by a temperature increase. Therefore, it is necessary to pay close attention to other fluxes in addition to the sensible heat flux when surface melt is investigated.

Several attempts that focus on the summer GrIS SEB characteristics have been performed. Presented results show that the net shortwave radiant flux is the main contributor for the surface

heating in general; however, detailed characteristics vary from place to place and differ from year to year. *Greuell and Konzelmann* (1994) unveiled temporal changes in SEB at the ETH Camp (69°34' N, 49°18'W, 1155 m a.s.l.), west Greenland, during the 1990 summer (June, July, and August). During this summer, average net shortwave radiant flux ( $82 \text{ W m}^{-2}$ ) and sensible heat flux ( $34 \text{ W m}^{-2}$ ) acted to heat the surface, while average net long-wave radiant flux ( $-54 \text{ W m}^{-2}$ ) and latent heat flux ( $-28 \text{ W m}^{-2}$ ) played a role in cooling the surface. SEB characteristics during the 1991 summer at the same place was presented by *Ohmura et al.* (1994). According to their results, the absolute values of each dominant SEB component averaged in this summer decreased obviously from the 1990 summer (net shortwave radiant flux was  $65 \text{ W m}^{-2}$ ; net long-wave radiant flux was  $-44 \text{ W m}^{-2}$ ; sensible heat flux was  $16 \text{ W m}^{-2}$ ; and latent heat flux was  $-6 \text{ W m}^{-2}$ ). Summer SEB characteristics at the higher place on the GrIS was described by *Cullen and Steffen* (2001). They demonstrated that average turbulent (sensible and latent) heat fluxes at Summit (72°58'N, 38°51'W, 3203 m a.s.l.) during 21 June to 6 July 2000 was small ( $4$  and  $3 \text{ W m}^{-2}$ , respectively), while average net shortwave radiant flux ( $82 \text{ W m}^{-2}$ ) and net long-wave radiant flux ( $-68 \text{ W m}^{-2}$ ) were comparable with previous results at ETH Camp. *van den Broeke et al.* (2011) presented long-term records of SEB at three automated weather stations (AWSs) situated along the K-transect, a stake array in southwest Greenland that extends from the ice margin to 1850 m a.s.l. They demonstrated that the temperature and moisture contrasts between ambient atmosphere and (melting) ice surface are less pronounced higher on the ice sheet, resulting in smaller summertime values of turbulent heat fluxes and net long-wave radiant flux at the higher elevations.

In the present study, our goal was to understand the record near-surface melt event that occurred over the GrIS in 2012 by investigating snow–atmosphere interactions from the standpoint of the SEB. For this purpose, we employed data obtained from in situ measurements made at a site named SIGMA (Snow Impurity and Glacial Microbe effects on abrupt warming in the Arctic)-A (*Aoki et al.*,

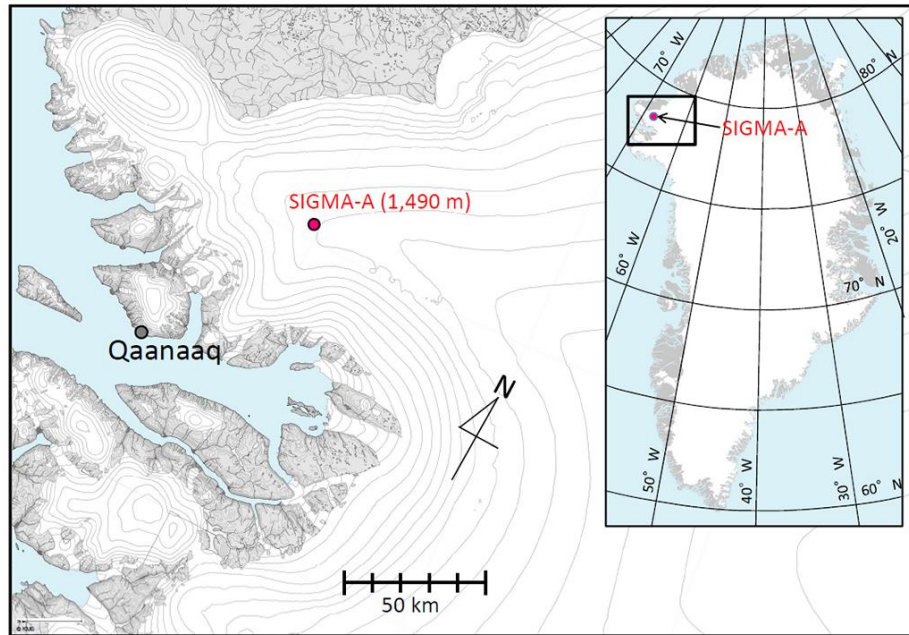


**Figure 5.1.** The location of site SIGMA-A together with ice sheet surface elevation contours (m a.s.l.). Height interval is 100 m.

2014a) in northwest Greenland during the 2012 summer intensive observation period (30 June to 14 July, hereafter IOP). During the latter half of the IOP, which coincided with the period of the record near-surface melt event reported by *Nghiem et al.* (2012), we observed remarkable melting of the near-surface snowpack and encountered continuous rainfall (*Aoki et al.*, 2014b; *Yamaguchi et al.*, 2014). In the process of calculating the SEB, radiation-related terms could be determined from in situ measurements (described in Sect. 5.2); however, the sensible heat flux, latent heat flux, and heat supply by rainfall, which were not measured directly at the SIGMA-A site, had to be calculated in some way. In this study, we therefore calculated these fluxes by using the physical snowpack model SMAP (Snow Metamorphism and Albedo Process), which was originally developed and evaluated for seasonal snowpack (*Niwano et al.*, 2012, 2014). Because this study was the first attempt to apply the SMAP model in a polar region, we carried out a preliminary examination of various aspects of

the capacity of the SMAP model. This model validation study was expected to increase the reliability both of the SMAP model itself and of the Meteorological Research Institute Earth System Model version1 (MRI-ESM1) (*Yukimoto et al.*, 2011), in which the SMAP model is used to calculate energy exchanges between the snow surface and atmosphere in the global cryosphere.

We begin by presenting an outline of our in situ measurements conducted at SIGMA-A during summer 2012. Then we describe the modification of the SMAP model that enabled its use to simulate polar conditions. We verified the accuracy of the model with respect to the snow temperature profile, snow surface temperature, surface optically equivalent snow grain radius, and shortwave albedo. Finally, we used the SMAP model to explore the SEB during the IOP at the SIGMA-A site by diagnosing the turbulent heat fluxes and heat supplied by rainfall.

## **5.2. Field measurements at the SIGMA-A site**

In this section we report the in situ data acquired during the IOP at site SIGMA-A (78°03'N, 67°38'W, 1490 m a.s.l.) (*Aoki et al.*, 2014a) in northwest Greenland (Fig. 5.1), and we report the observed meteorological and snow conditions. An AWS was newly installed at site SIGMA-A on 29 June 2012 (*Aoki et al.*, 2014a). In the northwest GrIS, two GC-Net AWS sites exist (Steffen and Box, 2001): one is the Humboldt site (78°32'N, 56°50'W, 1995 m a.s.l.) and the other is the GITS site (77°08'N, 61°02'W, 1887 m a.s.l.). *Steffen and Box* (2001) presented monthly mean temperatures at these stations and also demonstrated that the mean temperature lapse rate over GrIS in summer was 0.4 °C per 100 m. This information allows us to estimate the average near-surface air temperature during July at the SIGMA-A site, resulting in a value of −6.5 °C. This region of the northwestern GrIS is now being carefully monitored, because since around late 2005 the ice loss over southern portions of the GrIS has been spreading rapidly northward along the northwest coast (*Khan et al.*, 2010). Dates and times throughout this paper are expressed in terms of the universal time clock (UTC); the difference between local time (LT) at site SIGMA-A and UTC is −2 h.

### 5.2.1. Meteorological observations

The AWS measured air temperature and relative humidity with respect to water with a humidity and temperature probe (HMP155, Vaisala, Finland) protected from direct solar irradiance by a naturally aspirated 14-plate Gill radiation shield (41005, Young, USA) at 3.0 and 6.0 m above the snow surface on 29 June. According to *van den Broeke et al.* (2009), radiation errors in the unventilated air temperature measurement can be up to 3 °C under conditions of low wind speed and high insolation. However, no corrections were made to measured air temperature in the present study, because low wind speeds ( $< 1.0 \text{ m s}^{-1}$ ) were rarely observed at SIGMA-A during IOP, as noted later in this section. As for relative humidity with respect to water, we converted it into relative humidity with respect to ice when air temperature was below 0 °C and performed the correction presented by *Anderson* (1994). The AWS also measured wind speed and direction with a wind monitor (05103, Young, USA) at 3.0 and 6.0m above the surface. The AWS was also equipped with a digital barometer (PTB210, Vaisala, Finland) and an ultrasonic distance sensor (SR50, Campbell, USA) for snow depth monitoring. We used a net radiometer (CNR4, Kipp & Zonen, the Netherlands) to measure downward and upward shortwave (wavelength  $\lambda = 0.305\text{--}2.8 \text{ }\mu\text{m}$ ) and long-wave ( $\lambda = 4.5\text{--}42 \text{ }\mu\text{m}$ ) radiant fluxes. Downward and upward near-infrared ( $\lambda = 0.715\text{--}2.8 \text{ }\mu\text{m}$ ) radiant fluxes were observed by pyranometers (CMP6, Kipp & Zonen, the Netherlands) with RG715 cutoff filter domes. Measured data were sampled and stored in a data logger (CR1000, Campbell, USA) every 1 min. *Aoki et al.* (2014a) have provided a more detailed description of the AWS. In the present study, we used 5 min average values of AWS data, but to highlight important temporal evolution the SEB data reported after Sect. 5.5 are 1 h averages.

In addition to the automatic measurements, we performed manual spectral albedo measurements using a field spectroradiometer (FieldSpec 3, Analytical Spectral Devices, Inc., USA) ( $\lambda = 0.35\text{--}2.5 \text{ }\mu\text{m}$ ). The details of the measurement procedure were based on the method of *Aoki et al.* (2000). Use

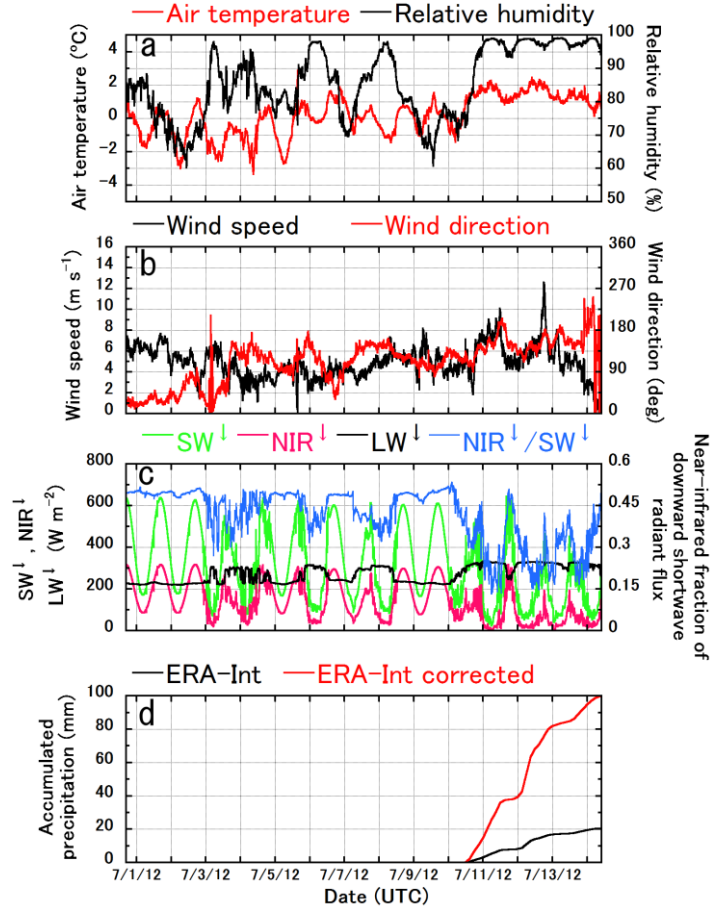


**Figure 5.2.** Meteorological conditions measured at SIGMA-A during the IOP (30 June to 14 July 2012): (a) air temperature and relative humidity with respect to water observed at a nominal height of 3.0 m above the snow surface; (b) wind speed and direction observed at 3.0 m above the snow surface on 29 June 2012 (wind direction is denoted in degrees that indicate the direction from which the wind is blowing; the degrees increase from 0 to 360 as the direction is rotated clockwise from north); (c) downward shortwave ( $SW^{\downarrow}$ ), near-infrared ( $NIR^{\downarrow}$ ), long-wave ( $LW^{\downarrow}$ ) radiant fluxes, and the near-infrared fraction of the  $SW^{\downarrow}$ ; and (d) accumulated precipitation obtained from 3-hourly ERA-Interim reanalysis data (ERA-Int), where the black line denotes the original amount of precipitation and the red line reflects the correction based on in situ measurements of accumulated precipitation measured during the period from 20:00 UTC on 12 July 2012 to 11:00 UTC on 14 July 2012.



of the obtained spectral albedo in a GSAF (ground-based spectral radiometer system for albedo and flux; *Kuchiki et al.*, 2009) channel with a  $\lambda$  of 1.23  $\mu\text{m}$  allowed us to retrieve the surface optically equivalent snow grain radius (hereafter simply referred to as the “snow grain size” unless otherwise stated) with the GSAF algorithm developed by *Kuchiki et al.* (2009). In the latest version of this algorithm, the model of snow grain shape can be arbitrarily chosen to be a sphere, spheroid, or Voronoi aggregate. In this study we selected the Voronoi aggregate model developed by *Ishimoto et al.* (2012), because this choice led to the best agreement with manually measured in situ surface snow grain size in the case of our data (see Sect. 5.2.2). We henceforth refer to these data as snow grain size retrieved by ground-based remote sensing (GRS). We used GRS data for model evaluation (Sect. 5.4.3).

Figure 5.2 presents time series of meteorological conditions measured with the AWS during the IOP. Until 9 July, air temperature at 3.0 m above the surface was already high and often exceeded 0 °C in the daytime. The time interval from 10 July until the end of the IOP coincided with the record near-surface melt event period reported by *Nghiem et al.* (2012); during that time air temperature increased slightly and remained above 0 °C, which is much larger than the estimated possible average air temperature at the SIGMA-A site: −6.5 °C (Sect. 5.2) continuously (Fig. 5.2a). The relative humidity with respect to water recorded at 3.0m above the surface was related to the high air temperature and tended to be high, the values sometimes approaching 100 % (Fig. 5.2a). At site SIGMA-A, low wind speeds ( $< 1.0 \text{ m s}^{-1}$ ) were rarely observed at 3.0 m above the surface during the IOP (Fig. 5.2b). The gradual day-by-day rise of air temperature was accompanied by a strong southeast wind with a speed sometimes over  $10 \text{ m s}^{-1}$ . Radiation parameters (Fig. 5.2c) reflect sky conditions. For example, until 3 July and around 9 July, we observed clear-sky conditions on site. During the clear-sky period, the downward shortwave and near-infrared radiant fluxes showed an obvious diurnal cycle, whereas the downward long-wave radiant flux was almost constant. In

contrast, cloudy-sky conditions (subjectively observed prevailing cloud types were Cumulus, Stratocumulus, and sometimes Stratus) on 3, 4, 6, 7, and 8 July and after 10 July were characterized by reduced downward shortwave and near-infrared radiant fluxes and increased downward long-wave radiant flux. During such conditions, the near-infrared fraction of the downward shortwave radiant flux decreased to around 0.3, while it was around 0.5 under clear-sky conditions. *Neff et al.* (2014) examined synoptic-scale atmospheric conditions over the GrIS during July 2012 from various aspects and summarized notable features as follows: (1) warm air originating from a record North American heat wave (the North American drought of 2012 was the worst since 1895), (2) transitions in the Arctic Oscillation, (3) transport of water vapor via an atmospheric river over the Atlantic to Greenland, and (4) the presence of warm ocean waters south of Greenland. *Bonne et al.* (2015) clearly showed that moist air mass was advected northward following a narrow band reaching southern Greenland and then it moved northward along the western Greenland coast around 9 July. Observed features of above-mentioned meteorological properties during the IOP at the SIGMA-A site are consistent with these large-scale atmospheric conditions.

At the SIGMA-A site, no rainfall was observed on site until 9 July. After 10 July, we encountered continuous rainfall until 14 July (*Aoki et al.*, 2014b; *Yamaguchi et al.*, 2014). Because precipitation is one of the critical parameters for a snowpack model that is used to calculate mass balance of a snowpack, the total amount of precipitation during 10–14 July was estimated on the basis of precipitation collected with a bucket during the period from 12 July, 20:00 UTC, to 14 July, 11:00 UTC, and on the 3-hourly European Centre for Medium-Range Weather Forecasts (ECMWF) Interim reanalysis (ERA-Interim) data (*Dee et al.*, 2011). At first, the precipitation that accumulated in the bucket from 12 July, 20:00 UTC, to 14 July, 11:00 UTC, and the 3-hourly ERA-Interim reanalysis data were compared. For this comparison, ERA-Interim 1 h accumulated precipitation was simply estimated to be one-third of the 3-hourly accumulated precipitation. The comparison

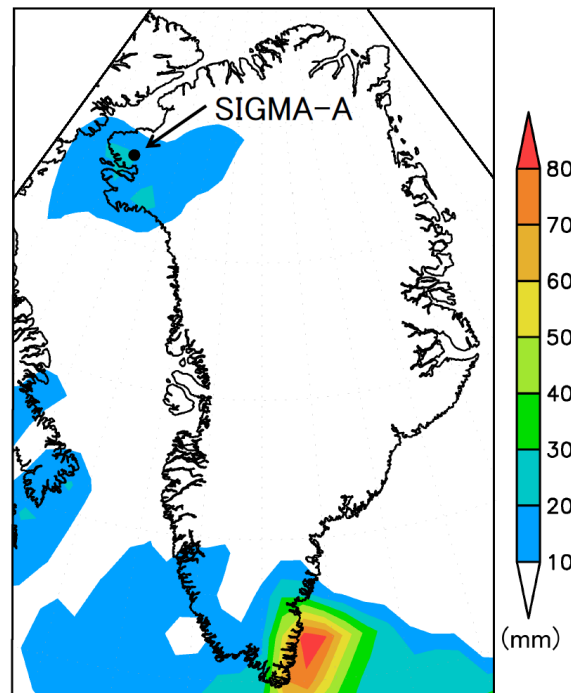


**Figure 5.3.** Accumulated precipitation from 00:00 UTC on 10 July 2012 to 12:00 UTC on 14 July 2012 obtained from the 3-hourly ERA-Interim reanalysis data. Black colored circle indicates the location of site SIGMA-A.

indicated that the accumulated precipitation obtained from the ERA-Interim reanalysis data was lower by a factor of 1 / 4.9. The most prevailing reason for this discrepancy was not a misrepresentation of the true area of rainfall but just underestimation by the ERA-Interim reanalysis (Fig. 5.3). As demonstrated by *Chen et al.* (2011), ERA-Interim data originally tend to underestimate annual accumulation in the area north of 68°N, even though it shows close spatial pattern of accumulation to the observations over the whole area of GrIS. In addition, it is possible that insufficient horizontal resolution (0.75°) and a hydrostatic atmospheric model, which cannot reproduce a short-time mesoscale convective system realistically in general, might have caused the large discrepancy. Finally, the precipitation that accumulated between 10 and 14 July, 100 mm, was

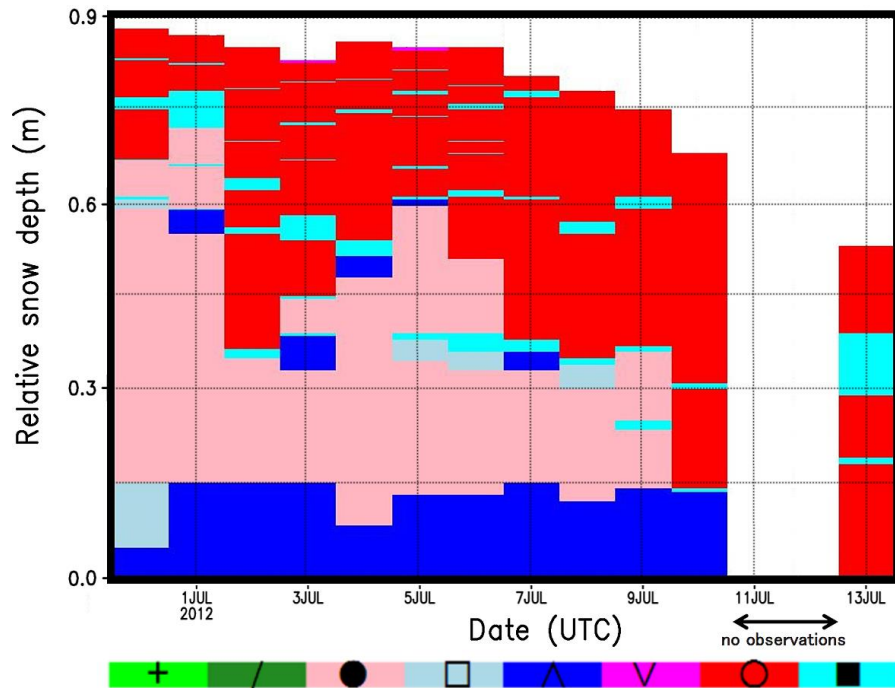


**Figure 5.4.** Temporal evolution of observed main snow grain shape profile within the NSL, which was defined by a thick bottom ice layer, at SIGMA-A during the IOP. Vertical axis (relative snow depth) denotes the height above the bottom thick ice layer. Characters and colors indicating snow grain shape follow the definition by *Fierz et al.* (2009). In sequence from the left they denote precipitation particles, decomposing and fragmented precipitation particles, rounded grains, faceted crystals, depth hoar, surface hoar, melt forms, and ice layer.

obtained by multiplying ERA-Interim reanalysis data by a factor of 4.9 (Fig. 5.2d). According to *Ohmura and Reeh* (1991), annual total precipitation near the SIGMA-A site is extrapolated to be around 200–300 mm w.e. The estimated total precipitation during this event can account for more than 30–50 % of the annual total precipitation. The procedure to input this information into the SMAP model is described in Sect. 5.3.3.

### 5.2.2. Snow pit measurements

Over the course of the IOP, we performed snow pit observations in the local morning (around 09:30 LT) in order to characterize the physical profiles of the snow (*Yamaguchi et al.*, 2014). We also collected near-surface snow samples to measure the mass concentrations of light-absorbing snow impurities such as black carbon (BC) and dust (*Aoki et al.*, 2014b).

The near-surface layer (NSL) of the snow was recognizable by quite a thick bottom ice layer. We focused on this near-surface layer in the snow pit observations, which were performed every day from 30 June to 13 July except for 11 and 12 July, when there was heavy rain at the SIGMA-A site. The thickness of the layer (above the ice layer) was 88 cm on 30 June. At present, the NSL has not been determined to be the latest annual layer because of the lack of justification. Measured properties included profiles of snow grain shape, snow temperature (including bottom ice layer temperature), snow density, volumetric water content, and geometric snow grain size. In addition, the snow grain size of the top 10 cm was measured manually after 1 July. In this snow grain size measurement process, we followed the definition of “ $r_2$ ” presented by *Aoki et al.* (2000, 2003, 2007): half the branch width of dendrites or half the width of the narrower portion of broken crystals. Figure 5.4 shows the temporal evolution of the observed snow grain shape profile in the NSL at the SIGMA-A site from 30 June to 13 July 2012. On the whole, until 9 July this layer could be roughly divided into three parts: a bottom layer composed of depth hoar, a middle layer of rounded grains (sometimes including faceted crystals), and a top layer composed of melt forms, including an ice layer of variable thickness. After 10 July, a wet snow layer expanded from the top to the bottom as the air temperature increased slightly (Fig. 5.2a), and the rainfall event occurred (Fig. 5.2d). The measured snow temperature profile is presented in Sect. 5.4.1 and compared to the results simulated by the SMAP model. In this comparison, a total of 221 profiles (after rejecting unphysical data) were available. As for the other snow properties, we used only the data that we obtained on 30 June to

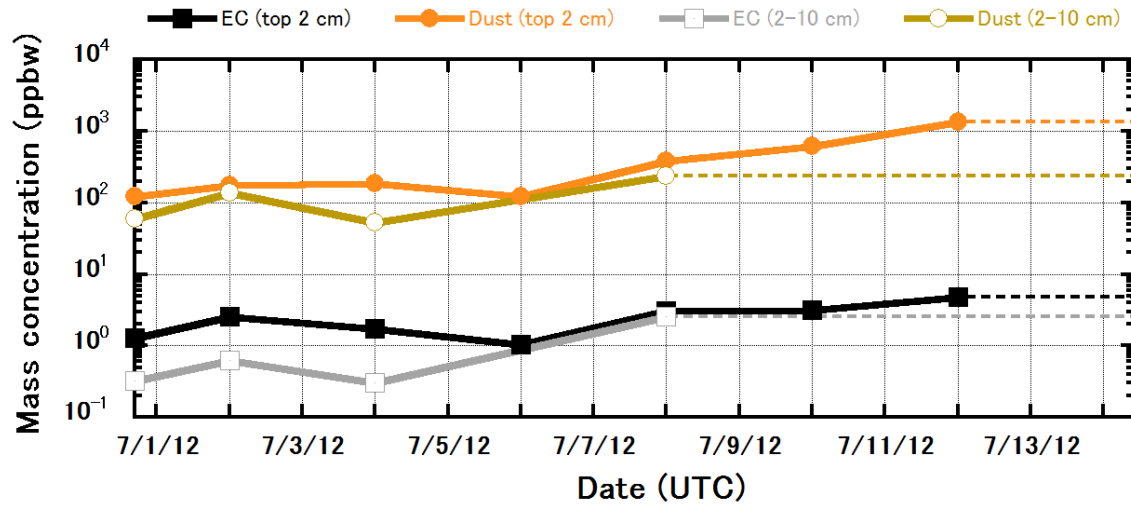


**Figure 5.5.** Measured mass concentrations of elemental carbon (EC) and dust in the top 2 cm of snow layers and the subsurface (2–10 cm) layers at the SIGMA-A site during the IOP. Dashed lines indicate periods when there were no measurements.

specify the initial physical conditions of the snowpack at the SIGMA-A site for the SMAP model simulations. The procedure is briefly explained in Sect. 5.3.3.

Snow samples to measure the mass concentrations of snow impurities were collected from the top 2 cm and the 2–10 cm layer every other day from 30 June to 12 July (Aoki *et al.*, 2014b). To obtain the mass concentrations of elemental carbon (EC), the samples were melted and filtered on site, and the filters were weighed and assayed with a carbon analyzer (Lab OC-EC Aerosol Analyzer, Sunset Laboratory Inc., USA). In this study we assumed, following Aoki *et al.* (2011), that EC was equivalent to BC. The dust concentrations were determined by subtracting total carbon concentrations from the total impurity concentrations, which were estimated from the difference between the dry weights of the filters before and after filtering (Aoki *et al.*, 2003, 2007). The detailed analytical procedure is precisely described by Kuchiki *et al.* (2009) and Aoki *et al.* (2011, 2014b).

Figure 5.5 shows the temporal changes in the mass concentrations of EC and dust in the near-surface

snowpack at the SIGMA-A site during the IOP; the EC concentrations increased rapidly after 6 July. *Aoki et al.* (2014b) have discussed the reasons for this obvious increase, and they concluded that effects of sublimation/evaporation and snowmelt amplification due to the low scavenging efficiency of meltwater played an important role.

### **5.3. Numerical simulation with the SMAP model**

#### **5.3.1. SMAP model overview**

The multilayered physical snowpack model SMAP calculates mass and energy balances of the snowpack by taking snow settlement, phase changes, water percolation, and snow metamorphism into account. The most distinguishing characteristic of the SMAP model is the fact that it incorporates the physically based snow albedo model (PBSAM) developed by *Aoki et al.* (2011). PBSAM calculates snow albedo and the solar heating profile in the snowpack by explicitly considering effects of snow grain size and light-absorbing snow impurities such as BC and mineral dust. In default configuration, the SMAP model requires precipitation (partitioned in the model into snow and rain by using the algorithm to calculate snow: rain ratios as a function of wet bulb temperature; *Yamazaki*, 2001), air pressure, wind speed, air temperature, relative humidity, downward ultraviolet (UV)–visible and near-infrared radiant fluxes, the diffuse components of UV–visible and near-infrared radiant fluxes, downward long-wave radiant flux, subsurface heat flux, and the mass concentrations of snow impurities (BC and dust) (*Niwano et al.*, 2012). In the present study, the diffuse components of the UV–visible and near-infrared radiant fluxes were not available, as explained in Sect. 5.2.1. Under these circumstances, SMAP calculates these fluxes by using the scheme of *Goudriaan* (1977) together with internally diagnosed cloud fraction calculated from air temperature and simulated net long-wave radiant fluxes at the snow surface. The procedure for obtaining cloud fraction is based on the approach of *van den Broeke et al.* (2004, 2006). *Niwano et al.* (2014) used data obtained during the winters of 2007–2009 at Sapporo to investigate the

effectiveness of the process, and they demonstrated that the accuracy of the simulated snow depth and snow surface temperature were comparable in magnitude to the accuracy of the default configuration.

The main governing equation of the SMAP model is a one-dimensional energy balance equation that takes solar heating of the snowpack and melt–freeze cycles into account (*Niwano et al.*, 2012). This equation is approximated and solved with the Crank–Nicolson finite difference implicit method. In this numerical solution, the SMAP model assumes each model snow layer to have a thickness  $d$  that is allowed to range between  $d_{min}$  and  $d_{max}$ . The values of  $d_{min}$  and  $d_{max}$  used in the present study are discussed in Sect. 5.3.3. Solar heating of the snowpack was calculated with a component of PBSAM. Input requirements for this component include internally calculated profiles of snow grain size and snow water equivalent, as well as the mass concentrations of snow impurities given externally from in situ measurements or host global or regional circulation models. Snow grain size was calculated by employing a model geometry that envisions two spherical ice particles connected by a neck (*Lehning et al.*, 2002). By calculating the specific surface area of snow per unit volume with the nonspherical model geometry, SMAP obtains snow grain size. Temporal evolution of snow grain size is governed by the following three types of metamorphism regimes: equi-temperature metamorphism, temperature-gradient metamorphism, and wet snow metamorphism. The formulation of these metamorphism laws is based on results from the SNOWPACK model (*Lehning et al.*, 2002). Furthermore, the SMAP model implicitly takes into account the effects of snow metamorphism under alternating temperature gradients (small rounded grains can be formed even when the temperature gradient is large when the sign of the temperature gradient changes with a 24 h cycle) (*Pinzer and Schneebeli*, 2009) by forcing temperature gradient metamorphism, which generally induces rapid grain growth, not to occur in the top 20 cm of the each model layer.



Recently, the SMAP model was updated with respect to water movement in the snowpack, snow settlement, and turbulent heat exchanges under very stable conditions (*Niwano et al.*, 2014). Water movement in the snowpack is now governed by the Richards equation (*Richards*, 1931), which takes into consideration Darcy's law; hydraulic diffusivity and hydraulic conductivity are calculated by the van Genuchten model (*van Genuchten*, 1980) adapted to snow (*Shimizu*, 1970; *Hirashima et al.*, 2010; *Yamaguchi et al.*, 2010, 2012). As for snow settlement, the updated version of the SMAP model calculates the viscosity coefficient of snow using the scheme presented by *Vionnet et al.* (2012), which was developed to improve the performance of the Crocus model (*Brun et al.*, 1989, 1992; *Vionnet et al.*, 2012; *Carmagnola et al.*, 2014). To ensure small but non-zero turbulent heat exchanges under very stable conditions, we set an upper bound of 0.1 on the Richardson number. During IOP, low wind speeds were rarely observed at the SIGMA-A site, as mentioned in Sect. 5.2.1. As a result, preliminary numerical simulation revealed that the impact of the upper bound was not clear during IOP; however, it is still set in this study.

### 5.3.2. Adaption of the SMAP model to the Greenland snowpack

In this section we discuss the adaptation of the model that enabled the SMAP model to be suitable for polar (especially Greenland) snowpack simulations. To simulate the temporal evolution of snow temperature accurately by solving the one-dimensional energy balance equation in the snowpack, the thermal conductivity of snow  $k_{eff}$  ( $\text{W m}^{-1} \text{K}^{-1}$ ) should be assigned an appropriate value. In this study, we employed the parameterization of *Anderson* (1976) that describes  $k_{eff}$  as a function of snow density  $\rho_s$  ( $\text{kg m}^{-3}$ ):

$$k_{eff} = 0.021 + 2.5 \left( \frac{\rho_s}{1000} \right)^2. \quad (5.1)$$

This equation is widely used in polar regions (e.g., *van den Broeke et al.*, 2005; *Kuipers Munneke et al.*, 2009; *van As*, 2011; *Brun et al.*, 2011).

The snow surface roughness length for momentum  $z_0$  affects turbulent heat exchanges between the snow surface and the atmosphere. *Brock et al.* (2006) compiled published data of  $z_0$  and demonstrated that the values were quite dependent on surface conditions and places. Considering this, we assumed the following constant values for  $z_0$  (mm) presented by *Greuell and Konzelmann* (1994):

$$z_0 = \begin{cases} 0.12 & \text{for snow before melting} \\ 1.3 & \text{for snow after melting.} \end{cases} \quad (5.2)$$

They simulated the mass balance and englacial temperature at the ETH Camp, west Greenland, during the 1990 summer melting period with these values. During IOP, the surface condition at SIGMA-A was smooth. *van den Broeke et al.* (2009) presented time series of  $z_0$  at sites S5 (490 m a.s.l.), S6 (1020 m a.s.l.), and S9 (1520 m a.s.l.) on the K-transect in southwest Greenland during August 2003 to August 2007. The above-mentioned values for  $z_0$  (Eq. 5.2) fall in the range of their result at S9, where surface condition was relatively smooth. The uncertainty of the SMAP model calculated SEB caused by the choice of  $z_0$  is investigated in Sect. 5.5. In the SMAP model, roughness lengths for heat and moisture are calculated following *Andreas* (1987) as explained by *Niwano et al.* (2012).

### 5.3.3. Model configuration

In the present study we calculated the temporal evolution of snow physical states in the NSL (see Sect. 5.2.2) at the SIGMA-A site from 30 June 2012, 16:45 UTC, to 14 July 2012, 12:00 UTC. To perform detailed model simulations we divided the NSL into several thin model layers. According to *Dadic et al.* (2008), the recommended model vertical resolution for an Arctic snowpack is on the

order of 10 mm, because there is a strong feedback between small-scale snow structure and snow temperature that should be simulated accurately by snowpack models. Based on this consideration, the SMAP model vertical layer thickness (see Sect. 5.3.1) used in this study ranged between  $d_{min} = 2\text{mm}$  and  $d_{max} = 6\text{ mm}$ . Accordingly, it became necessary for the time step of the numerical integration  $\Delta t$  to be shortened. Thus,  $\Delta t$  was set to 30 s in the present study.

Input parameters used to drive the SMAP model in the present study were air pressure; air temperature and relative humidity at 3.0 m above the snow surface (Fig. 5.2a); wind speed at 3.0 m above the snow surface (Fig. 5.2b); downward shortwave, near-infrared, and long-wave radiant fluxes (Fig. 5.2c); accumulated precipitation (Fig. 5.2d); the temperature of the thick bottom ice layer in the NSL (lower boundary condition); and the mass concentrations of snow impurities (Fig. 5.5). In addition, the emissivity of the snow surface  $\varepsilon_s$  was assumed to be 0.98 (*Armstrong and Brun, 2008; van As, 2011*) throughout this study.

The time interval for meteorological properties was selected to be 5 min, whereas daily values were used for other properties. The corrected 3-hourly accumulated precipitation data were divided equally into each time interval. Regarding the measured mass concentrations of snow impurities (Fig. 5.5), we followed the same method used by *Niwano et al. (2012)*, who equated the values in the top 2 cm of the model layers of the snowpack to the corresponding observed values and assigned the observed values in the 2–10 cm depth interval equally to the lower model layers. During the period when measurements of the mass concentrations of snow impurities were unavailable (dashed lines in Fig. 5.5), we used the values measured at the nearest point in time. The initial physical states of the snowpack in the NSL on 30 June (profiles of snow grain shape, snow temperature, snow density, volumetric water content, and geometric snow grain size) were taken from the snow pit observations conducted on 30 June 2012, 16:45 UTC (*Yamaguchi et al., 2014*). These observations were distributed within the model layers, and the layer thickness  $d$  was in all cases set to 5mm in the NSL

**Table 5.1.** Comparison of SMAP simulation results with in situ measurements. RMSE and ME are the root mean square error and mean error (the average of the difference between simulated values and observed values), respectively. Figures in parentheses indicate scores when the observed temperature was negative (i.e., dry snow conditions).

Parameters	RMSE	ME
Snow temperature profile (°C)	0.60 (0.81)	−0.16 (−0.24)
Snow surface temperature (°C)	0.58 (0.94)	0.25 (0.68)
Surface snow grain size (mm)	0.21	0.17
Shortwave albedo	0.022	0.008

at that time. Because the SMAP model calculates shortwave albedo as a function of snow grain size and the mass concentrations of snow impurities, information regarding an optically equivalent snow grain size profile was necessary. In the present study, an optically equivalent profile was obtained by multiplying the geometric profile by a factor that produced agreement between the calculated shortwave albedo and observations on 30 June 2012, 16:45 UTC. The assigned factor was 0.88.

#### 5.4. Model evaluation using the data at the SIGMA-A site

In this section we evaluate the SMAP model using the data measured at the SIGMA-A site during the IOP to adapt it to the GrIS snowpack. The following parameters were validated quantitatively: snow temperature profile, snow surface temperature, surface snow grain size, and shortwave albedo. When a measured snow temperature profile was compared against simulation results, the depth of the NSL simulated by the model (the SMAP model tended to underestimate the NSL’s depth by  $-2.0$  cm compared to the snow pit measurements during the IOP) was adjusted to the measured depth as a post-process in which model simulated internal properties were not modified at all. The measured snow surface temperature  $T_{s0}$  was calculated from the following relationship between the observed downward and upward long-wave radiant fluxes ( $L^\downarrow$  and  $L^\uparrow$ ):

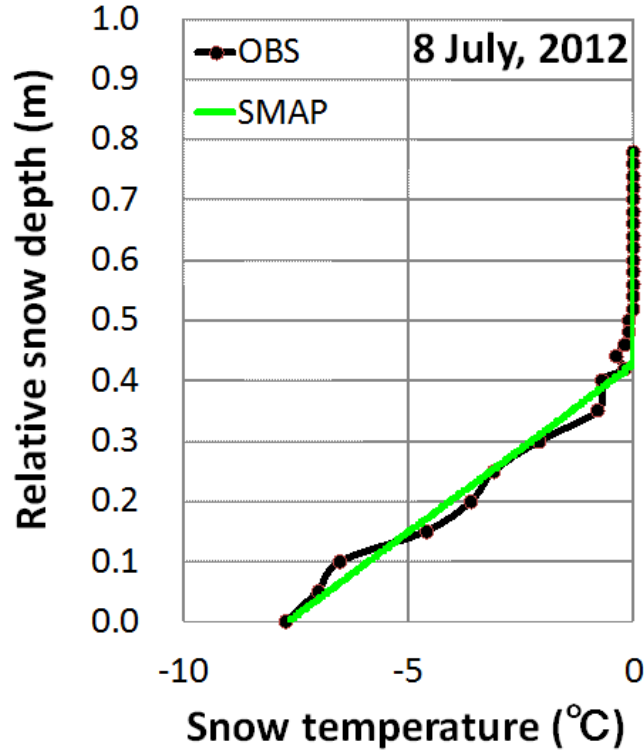


**Figure 5.6.** Comparison of snow temperature profiles in the NSL at the SIGMA-A site between snow pit observations (OBS) and profiles simulated with the SMAP model at 11:30 UTC on 8 July 2012.

Relative snow depth denotes the height of the NSL above the thick bottom layer of ice. The snow depths simulated by the SMAP model were adjusted to the measurements.

$$L^{\uparrow} = \varepsilon_s \sigma T_{s0}^4 + (1 - \varepsilon_s) L^{\downarrow} , \quad (5.3)$$

where  $\sigma$  is the Stefan–Boltzmann constant. The model performance was assessed in terms of the root mean square error (RMSE) and mean error (ME) (Table 5.1). In this paper ME is defined as the average difference between simulated and observed values.

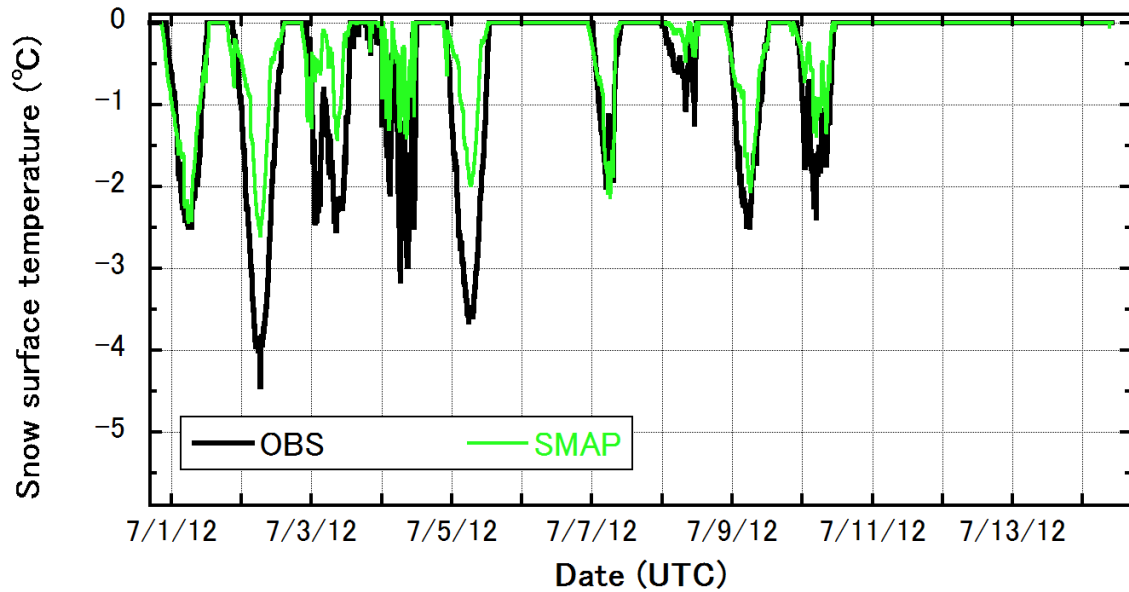


**Figure 5.7.** Snow surface temperature at the SIGMA-A site during the IOP observed with the AWS and simulated by the SMAP model. Observed snow surface temperature was calculated from observed downward and upward long-wave radiant fluxes (Sect. 5.4).

#### 5.4.1. Snow temperature profile

We first examined whether the SMAP model could reproduce the internal physical states of the NSL in terms of the snow temperature profile. Model performance during the IOP (Table 5.1) indicated that the model simulated the temperatures reasonably. An example profile comparison on 8 July showed that the top 40 cm of the observed snowpack was wet (Fig. 5.6), and the condition was reproduced by the SMAP model. Even when such observed wet snow conditions were excluded from the statistical assessment of model performance, the order of magnitude of the RMSE and ME did not change (Table 5.1).

#### 5.4.2. Snow surface temperature

Snow surface temperature affects all energy flux components of the SEB except for the net shortwave radiant flux. A comparison of observed and simulated snow surface temperatures during

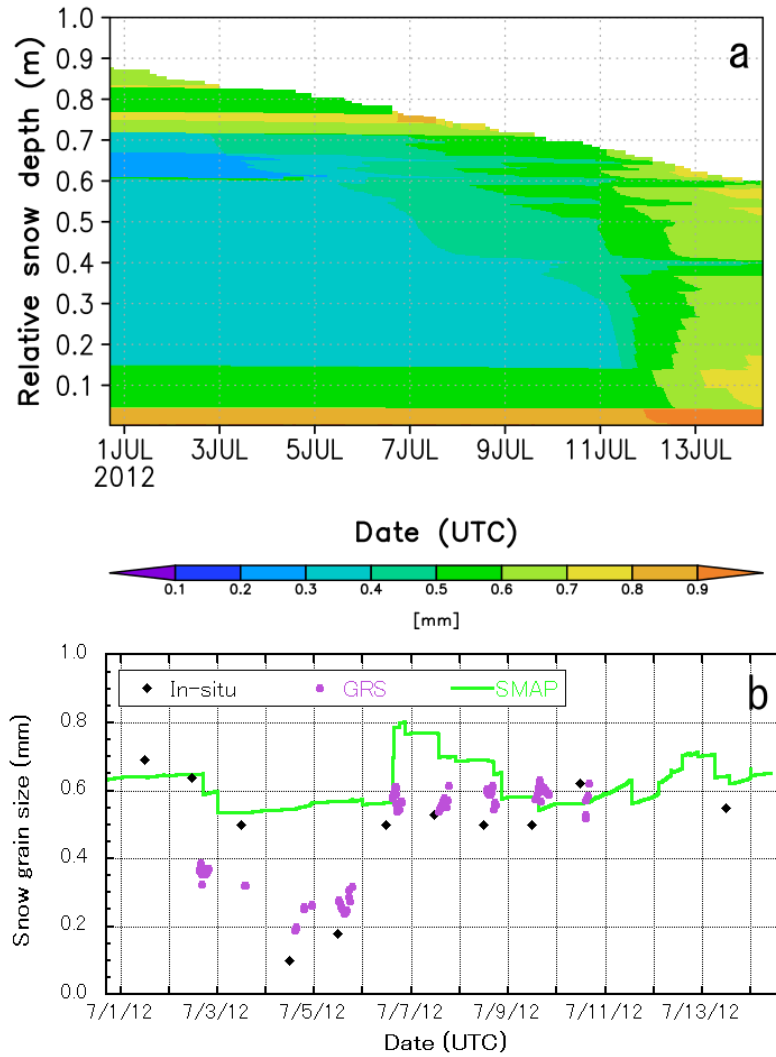


**Figure 5.8.** Temporal evolution of (a) simulated snow grain size profile in the NSL and (b) surface snow grain size from in situ snow pit observations (black diamond patterns), ground-based remote sensing (GRS) using spectral albedo data measured with a spectrometer (purple dots), and simulated by the SMAP model (solid green curve) at the SIGMA-A site during the IOP. Vertical axis in the upper panel (relative snow depth) denotes the height above the thick bottom ice layer in the NSL.

the IOP (Fig. 5.7) as well as the obtained MEs (Table 5.1) indicated that the SMAP model tended to overestimate snow surface temperature; however, the RMSE obtained in this study (0.58 °C) was an improvement compared to the previous study by *Niwano et al.* (2012) at Sapporo during the winters

of 2007–2009 (2.45 and 2.3 °C for the winters of 2007–2008 and 2008–2009, respectively). In this case as well, scores under dry snow surface conditions were still reasonable (RMSE = 0.94 °C and ME = 0.68 °C). These foregoing statistics are almost the same order of magnitude as the analogous statistics from previous, detailed snow modeling studies performed in polar regions (*Kuipers Munneke et al.*, 2009, 2012; *Brun et al.*, 2011).

#### **5.4.3. Surface snow grain size**

For the SMAP model, snow grain size is one of the key parameters to be simulated accurately, because the SMAP model calculates the snow albedo and solar heating profile in the snowpack using the PBSAM, for which snow grain size is an input parameter. Figure 5.8a depicts the simulated snow grain size profile in the NSL, and Fig. 5.8b compares the surface snow grain size determined from in situ manual measurements and GRS against the simulation result. Because the GRS estimates agreed well with in situ measurements, and because we could obtain more data from GRS than from in situ manual measurements, model validation was performed against GRS data in the present study. The simulated surface snow grain size sometimes decreased abruptly (Fig. 5.8b), although a new snowfall event was not observed during the IOP. The abrupt decrease in grain size was caused by rapid surface melting and subsequent continuous exposure of layers beneath that were simulated by the SMAP model (Fig. 5.8a). The order of magnitude of the simulated snow grain size was almost the same with the SMAP model and GRS, and the RMSE (0.21 mm) and ME (0.17 mm) (Table 5.1) were almost the same order of magnitude as the analogous errors reported by *Niwano et al.* (2012) for seasonal snow simulations at Sapporo, Japan, during the winters of 2007–2009 (RMSE = 0.31 and 0.15 mm, and ME = –0.04 and –0.02 mm for the winters of 2007–2008 and 2008–2009, respectively). During 3–5 July, when we observed surface hoar with small grains of snow on the surface at the SIGMA-A site (*Yamaguchi et al.*, 2014), discrepancies between observations and simulations stood out (Fig. 5.8b). The reason for this failure is that the SMAP model could not



simulate surface hoar formation during this period. In the SMAP model surface hoar is created when the latent heat flux is positive and the wind speed is less than  $3 \text{ m s}^{-1}$  (Föhn, 2001); however, the simulated  $H_L$  from the night of 2 July to the morning of 5 July was continuously negative (more detailed discussion follows in Sect. 5.6.2).

In the SMAP model, the latent heat flux is calculated on the assumption that the snow surface is saturated (Niwano *et al.*, 2012), an assumption that is widely made by many physical snowpack models. However, as Box and Steffen (2001) have pointed out, this method can detect surface hoar deposition only in cases of extreme temperature inversion, and this limitation leads to underestimation of surface hoar. Because this result suggests that reconsideration of the method of calculating the latent heat flux in the SMAP model is necessary to obtain an accurate SEB, we discuss this topic further in Sect. 5.6.2.

#### **5.4.4. Shortwave albedo**

Now we focus on the shortwave albedo, which is another important parameter for estimating snow–atmosphere interactions as well as snow surface temperature. Figure 5.9 compares observed shortwave albedos with albedos simulated with the SMAP model during the IOP. The comparison shows that the SMAP model successfully reproduced the observed diurnal variations. The RMSE and ME in Table 5.1 support this assessment. Furthermore, the SMAP model simulated observed spikes when snow albedo rapidly increased, especially around 4 July and after 10 July. The cause of these spikes is the fact that the snow albedo is generally higher under cloudy-sky than under clear-sky conditions (Liljequist, 1956; Yamanouchi, 1983; Aoki *et al.*, 1999). These results imply that the component of the PBSAM driven by the observed near-infrared and UV–visible fractions of the downward shortwave radiant flux, as well as the diffuse fractions calculated by the procedure described in Sect. 5.3.1, played an important role in improving the precision of the SMAP model simulations. Therefore, once the SMAP model or the PBSAM are coupled with atmospheric models,

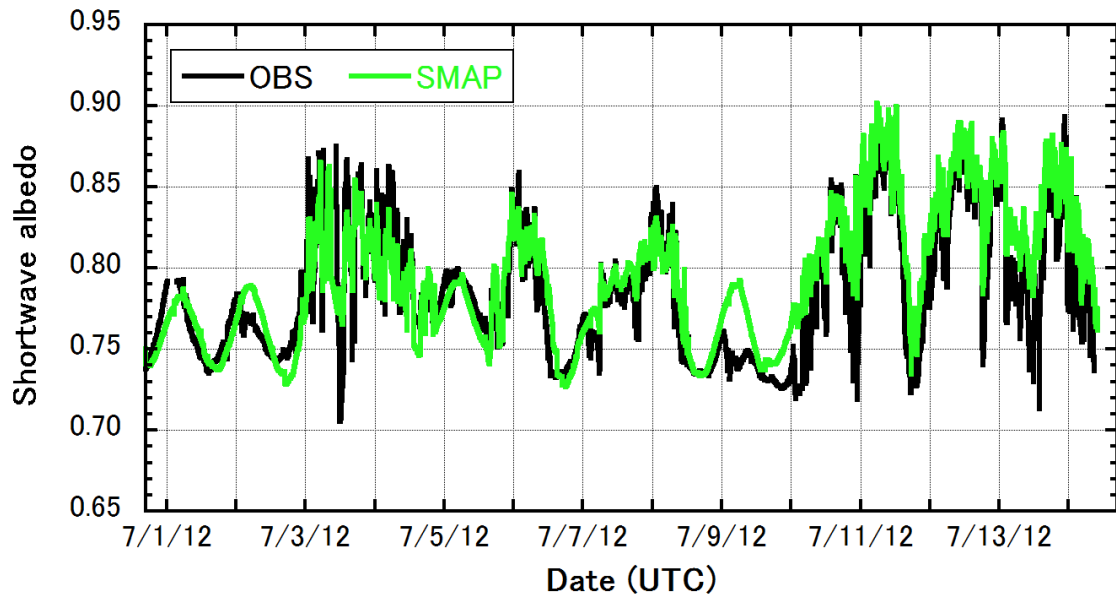


**Figure 5.9.** Shortwave albedos at the SIGMA-A site during the IOP observed with AWS and simulated by the SMAP model.

it is necessary for such host atmospheric models to simulate the presence or absence of cloud realistically. *King et al. (2015)* also argued that efforts to improve model simulations of surface energy balance and melt in the polar region should concentrate initially on reducing biases in modeled shortwave and long-wave radiant fluxes which are caused by deficiencies in the representation of cloud properties.

In Sect. 4.3, however, we found clear discrepancies between observed and simulated surface snow grain size, especially during 3–5 July, when simulated shortwave albedo agreed well with observations. This paradox can be explained as follows: as demonstrated by *Yamanouchi (1983)*, the difference between the downward near-infrared radiant fluxes under clear-sky and cloudy-sky conditions is larger than the analogous difference in the downward visible radiant fluxes. The explanation is that most of the absorption of solar radiation by clouds occurs in the near-infrared region, and the difference in multiple reflection effects due to the spectral differences of surface albedo magnifies the impact of this preferential near-infrared absorption. Figure 5.2c depicts the

observed near-infrared fraction of the downward shortwave radiant flux. Actually, the near-infrared fraction was depleted during the cloudy-sky conditions observed on 3, 4, 6, 7, and 8 July and after 10 July (Sect. 5.2.1). In the PBSAM, the shortwave albedo is calculated from a weighted summation of visible albedo and near-infrared albedo. The weights for these albedos are the visible and near-infrared fractions of the downward shortwave radiant flux (*Aoki et al.*, 2011). A decrease of the near-infrared fraction therefore increases the influence of the visible albedo on the calculated shortwave albedo, and the influence of the near-infrared albedo, which is mainly affected by snow grain size (*Wiscombe and Warren*, 1980), decreases. The simulated shortwave albedo therefore agreed with observations, even during 3–5 July, when the SMAP model could not reproduce surface hoar and the associated small near-surface snow grain size.

### 5.5. SEB during the IOP at SIGMA-A

Now we look into the SEB during the IOP at the SIGMA-A site to elucidate the physical conditions of both the snowpack and the atmosphere that led to the remarkable melting around 12 July, when the record near-surface melt occurred over more than 95 % of the entire surface of the GrIS (*Nghiem et al.*, 2012). The SEB equation (*Armstrong and Brun*, 2008) can be written as follows:

$$S_{net} + L_{net} + H_S + H_L + H_R + H_G = Q_{net} , \quad (5.4)$$

where  $S_{net}$  is the net shortwave radiant flux,  $L_{net}$  is the net long-wave radiant flux,  $H_S$  is the sensible heat flux,  $H_L$  is the latent heat flux,  $H_R$  is the heat flux associated with rainfall calculated as a function of rainfall rate and a difference in rain temperature (wet bulb temperature is assumed) and surface temperature (*Niwano et al.*, 2012),  $H_G$  is the subsurface conductive heat flux, and  $Q_{net}$  is the net energy flux at the snow surface. As already mentioned, these fluxes are defined to be positive when they are directed into the snow surface. The snow surface is heated when the flux is positive

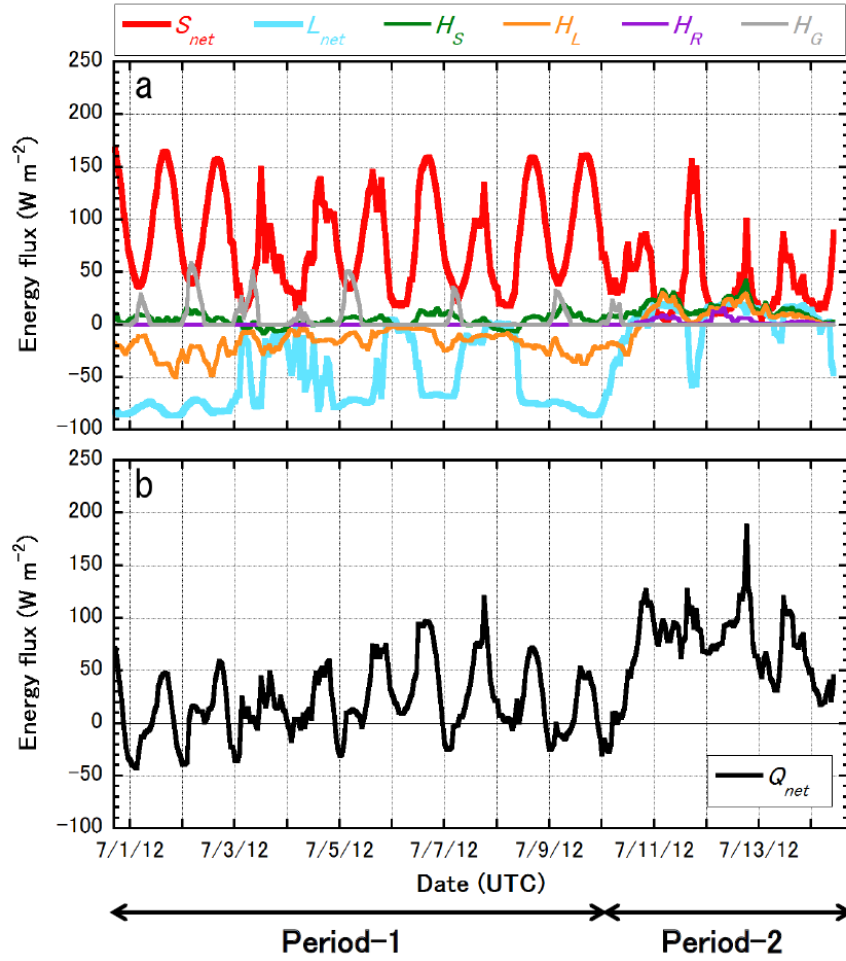


**Figure 5.10.** One-hour averaged surface energy balance at the SIGMA-A site during the IOP. The upper panel (a) shows net shortwave radiant flux ( $S_{net}$ ), net long-wave radiant flux ( $L_{net}$ ), sensible heat flux ( $H_s$ ), latent heat flux ( $H_L$ ), heat supply by rainfall ( $H_R$ ), and subsurface conductive heat flux ( $H_G$ ). These fluxes are defined to be positive when they are directed into the snow surface. The lower panel (b) denotes net energy flux ( $Q_{net}$ ). The snow surface is heated when  $Q_{net}$  is positive, whereas it is cooled if  $Q_{net}$  is negative.

and surface melt occurs if the surface temperature is 0 °C, whereas it is cooled if the flux is negative.

In this study,  $S_{net}$  and  $L_{net}$  were calculated from in situ measurements. Other fluxes on the left-hand side of Eq. 5.4 were estimated as a function of measured snow surface temperature by using the

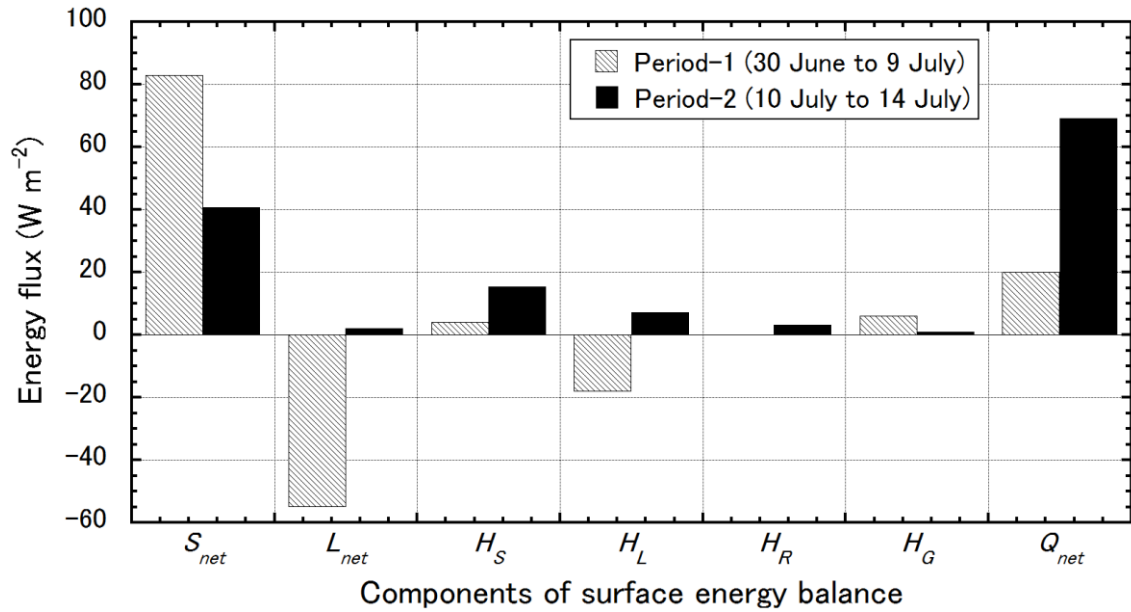


**Figure 5.11.** Comparison of average surface energy balance components ( $S_{net}$  is net shortwave radiant flux,  $L_{net}$  is net long-wave radiant flux,  $H_S$  is sensible heat flux,  $H_L$  is latent heat flux,  $H_R$  is heat supply by rainfall,  $H_G$  is subsurface conductive heat flux, and  $Q_{net}$  is net energy flux) between Period-1 and Period-2 at the SIGMA-A site.

SMAP model. Figure 5.10 shows the temporal changes of the 1 h averaged simulated SEB during the IOP.  $S_{net}$  remained positive throughout the IOP.  $L_{net}$  was negative for much of the time prior to 9 July but was positive most of the time after 10 July.  $H_S$  was close to 0 W m<sup>-2</sup> until 9 July, but it gradually increased after 10 July and sometimes reached about 50 W m<sup>-2</sup>. The other turbulent heat flux,  $H_L$ , was negative most of the time during the first half of the IOP, but it became generally positive after 10 July as well. After 10 July there was heavy rainfall frequently, but its impact on the SEB was quite small ( $H_R$  was less than 10 W m<sup>-2</sup> most of the time, although it sometimes reached more than 15 W m<sup>-2</sup>). Finally,  $H_G$  showed clear diurnal variation: it heated the surface especially during the night time, while it was almost 0 W m<sup>-2</sup> in the daytime as a result of isothermal profile in the near-surface snowpack caused by meltwater percolation. As a result, until 9 July the total surface

energy flux,  $Q_{net}$ , clearly varied diurnally, being negative during the night and positive during the day. However, after 10 July it remained positive at all times.

Because there was a clear contrast in the calculated SEB characteristics during the period from 30 June to 9 July (“Period-1”) and the time interval 10–14 July (“Period-2”), we compared the average SEB components between Period-1 and Period-2 (Fig. 5.11) to characterize the SEB at the SIGMA-A site around 12 July, when continuous melting was observed. Figure 5.11 reveals dramatic modulations of both  $S_{net}$  and  $L_{net}$ , and changes in  $H_S$  and  $H_L$  were also remarkable. Quantitatively, there were significant positive increments in  $H_S$  (4.0 to 15.3 W m<sup>-2</sup>; +11.3 W m<sup>-2</sup>),  $H_L$  (–18.0 to 7.2 W m<sup>-2</sup>; +25.2 W m<sup>-2</sup>), and  $L_{net}$  (–54.9 to 2.1 W m<sup>-2</sup>; +57.1 W m<sup>-2</sup>), the total positive increment being 96.7 W m<sup>-2</sup>. There was a remarkable decrease only in  $S_{net}$  (83.0 to 40.7 W m<sup>-2</sup>; –42.3 W m<sup>-2</sup>). As a result,  $Q_{net}$  increased by 49.1 W m<sup>-2</sup> (20.1 to 69.2 W m<sup>-2</sup>). These values, calculated during Period-1, are almost equal to the surface fluxes from June to August averaged during the summers of 2000–2011 over the GrIS accumulation area based on the MAR regional climate model (*Fettweis et al.*, 2011) and MODIS data presented by *Box et al.* (2012). However, the SEB characteristics during Period-2 (signs and orders) resemble those obtained at Langfjordjøkelen, Norway (*Giesen et al.*, 2014).

The decrease of  $S_{net}$  was due to both a reduction of downward shortwave radiant flux (352.7 to 203.9 W m<sup>-2</sup>) and a slight increase in shortwave albedo from 0.775 to 0.810. The latter value is as high as the 2000–2011 summer (June to August) average albedo over the GrIS accumulation area (0.809) reported by *Box et al.* (2012) and the cause of increase was mainly the appearance of clouds (discussed in Sect. 5.4.4). Modulation of  $H_S$  was caused mainly by an increase of temperature, which is clearly apparent in Fig. 5.2a. The cause of the increase in  $H_L$  was basically the same: increases in relative humidity and air temperature. The latter reached more than 0 °C. The abrupt transition of radiative properties is understandable from the perspective of cloud radiative forcing (defined as the

difference in net surface radiant fluxes under cloudy-sky and clear-sky conditions) in the polar region: at the snow surface shortwave cloud radiative forcing is negative and long-wave cloud radiative forcing is positive (*Aoki and Yamanouchi, 1992*). We thus conclude that the appearance of low-level clouds (Sect. 5.2.1) accompanied by a remarkable increase of temperature (Fig. 5.2a) played an important role and induced surface heating during Period-2. The heating occurred via a large increase in  $L_{net}$  which was able to substantially compensate for the reduction of  $S_{net}$ . *Bennartz et al.* (2013) have investigated the effect of clouds on the temporal development of surface temperature by performing numerical sensitivity tests with a prognostic surface energy balance model and by parameterizing downward radiant fluxes at the surface. They have argued that low-level liquid clouds played a critical role in the enhancement of surface melting at Summit, Greenland, by increasing near-surface temperature through their radiative effects. The present results, which highlight the importance of low-level clouds, are consistent with their conclusion.

## **5.6. Discussion**

In this section, we investigate uncertainties in the calculated SEB that can be induced by model settings and calculation methods of the SMAP model. The purpose of this work is to confirm the validity of SEB characteristics presented in Sect. 5.5. Because  $S_{net}$  and  $L_{net}$  are directly given from in-situ measurements (mentioned in Sect. 5.5), only uncertainties related to turbulent heat fluxes are discussed here.

### **5.6.1. Effects of model settings on the calculated SEB**

As mentioned in Sect. 3.2, we assumed constant values for  $z_0$  (0.12 and 1.3 mm for snow before and after melting, respectively) following *Greuell and Konzelmann (1994)* in this study. However, as *Braithwaite (1995)* pointed out, the uncertainty in  $z_0$  causes significant error in turbulent heat flux calculations. Therefore, firstly we performed numerical sensitivity tests based on the SEB calculation performed in Sect. 5.5, where the value of  $z_0$  was perturbed between the possible

maximum and minimum values. These values were determined as follows: from the compilation by *Brock et al.* (2006) the maximum value for  $z_0$  of the GrIS snow surface was found to be around 10 mm, while we assumed the minimum value for  $z_0$  of the GrIS snow surface to be around 0.01 mm based on the results by *Smeets and van den Broeke* (2008). Compared to the original run ( $H_S$  and  $H_L$  during IOP were estimated to be 7.6 and  $-10.0 \text{ W m}^{-2}$ , respectively), results from sensitivity studies revealed that absolute values of the turbulent heat fluxes were increased with the condition that  $z_0$  was set to be 10mm (mean differences against the original SEB calculation were  $0.8 \text{ W m}^{-2}$  and  $-1.4 \text{ W m}^{-2}$  for  $H_S$  and  $H_L$ , respectively; the same tendency was also reported by *van As*, 2011), while they were reduced if  $z_0$  was set to be 0.01mm (mean differences against the original SEB calculation were  $-2.9$  and  $3.8 \text{ W m}^{-2}$  for  $H_S$  and  $H_L$ , respectively). However, these uncertainties still do not affect characteristics of temporal changes in SEB during IOP at the SIGMA-A site discussed in Sect. 5.5 so much.

Secondly, we investigated effects of  $\varepsilon_s$  introduced in Sect. 5.3.3 on SEB calculations. In this sensitivity test,  $\varepsilon_s$  was set to be 1.0 and surface temperature (to be input to the SMAP model) was calculated only from observed  $L^\uparrow$ . The result indicated that mean differences of turbulent heat fluxes against the original SEB calculation were 1.1 and  $0.9 \text{ W m}^{-2}$  for  $H_S$  and  $H_L$ , respectively. This result implies that the sensitivity of SEB calculation to the choice of  $\varepsilon_s$  is small, and SEB characteristics during IOP at the SIGMA-A site presented in Sect. 5.5 is still valid. *van As* (2011) also performed this type of sensitivity test and demonstrated  $\varepsilon_s$ 's small impact on the SEB calculation.

### **5.6.2. Uncertainties caused by the latent heat flux calculation method**

As discussed in Sect. 5.4.3, calculation of the latent heat flux  $H_L$  based on the assumption that air at the surface is saturated with respect to ice at the snow surface temperature might lead to underestimation of surface hoar deposition, which implies that internally diagnosed  $H_L$  in the SMAP model simulation presented in Sect. 5.4 can be underestimated. Here we refer to this method as



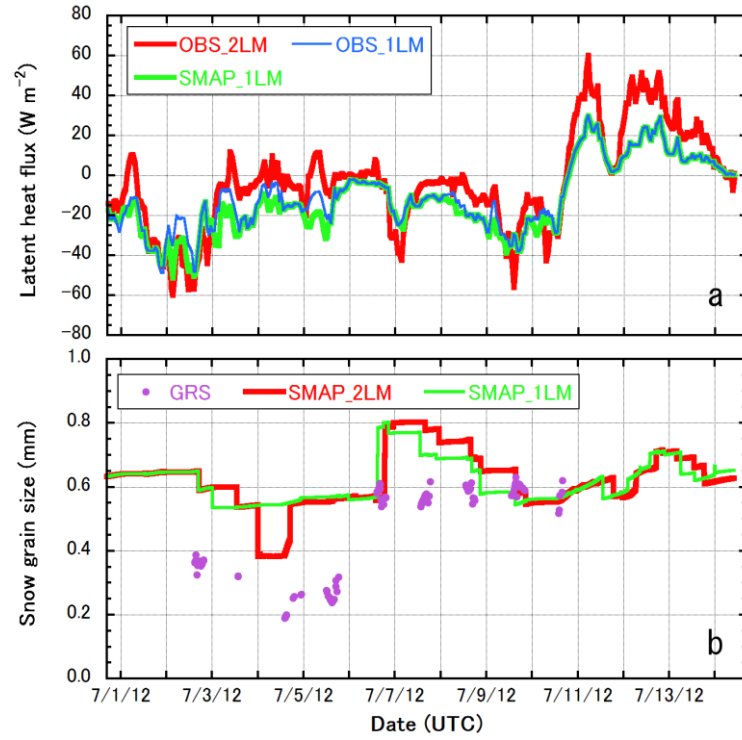


**Figure 5.12.** (a) Temporal evolution of 1 h averaged latent heat fluxes calculated from atmospheric measurements at 6 and 3 m above the surface (OBS\_2LM) and measurements at 3 m above the surface (OBS\_1LM), as well as the SMAP simulation forced by one-level (3 m above the surface) atmospheric measurements (SMAP\_1LM). (b) Comparison of surface snow grain size at the SIGMA-A site during the IOP with surface snow grain size from ground-based remote sensing (GRS) using spectral albedo data measured with a spectrometer and those from the SMAP simulations driven by two-level (6 and 3 m above the surface) atmospheric measurements (SMAP\_2LM) or one-level (3m above the surface) atmospheric measurements (SMAP\_1LM).

1LM, in accordance with *Box and Steffen* (2001). According to *Box and Steffen* (2001), employing two-level atmospheric data to calculate  $H_L$  can solve this problem, an approach we designate as the 2LM method. As noted in Sect. 5.2.1, the SIGMA-A AWS measured temperature, relative humidity, and wind speed at heights of 3 and 6 m above the surface. In this section we calculate the latent heat

flux using the AWS data at these two heights, and we investigate whether the SMAP model can simulate surface hoar formation with small snow grain sizes by using the 2LM method.

The original formulation of  $H_L$  employed by the SMAP model (1LM) is based on the bulk method and is expressed as follows (Niwano *et al.*, 2012):

$$H_L = \frac{\rho_a L_v \kappa^2 u_1 (q_1 - q_{s0})}{\left[ \ln\left(\frac{z_1}{z_0}\right) - \Psi_M\left(\frac{z_1}{L}\right) \right] \left[ \ln\left(\frac{z_1}{z_Q}\right) - \Psi_H\left(\frac{z_1}{L}\right) \right]}, \quad (5.5)$$

where  $\rho_a$  is the density of air,  $L_v$  is the latent heat of sublimation or evaporation,  $\kappa$  is the von Kármán constant,  $u_1$  is the wind speed at a measurement height  $z_1$  (in this study,  $z_1$  is 3 m),  $q_1$  and  $q_{s0}$  are the specific humidity at  $z_1$  and the snow surface, respectively,  $\Psi_M$  and  $\Psi_H$  are profile functions for momentum and heat, respectively,  $z_0$ , and  $z_Q$  are roughness lengths for momentum and moisture, respectively, and  $L$  is the Obukhov length. When we now use atmospheric data at two heights ( $z_1$  and  $z_2$ ;  $z_2$  is 6 m in this study), the formulation of the bulk method with the 2LM model can be rewritten as follows:

$$H_L = \frac{\rho_a L_v \kappa^2 (u_2 - u_1) (q_2 - q_1)}{\left[ \ln\left(\frac{z_2}{z_1}\right) - \Psi_M\left(\frac{z_2}{L}\right) + \Psi_M\left(\frac{z_1}{L}\right) \right] \left[ \ln\left(\frac{z_2}{z_1}\right) - \Psi_H\left(\frac{z_2}{L}\right) + \Psi_H\left(\frac{z_1}{L}\right) \right]}, \quad (5.6)$$

where  $u_2$  and  $q_2$  are the wind speed and specific humidity at  $z_2$ , respectively. Other parameters are calculated by the same method used by Niwano *et al.* (2012). The choice of  $\Psi_M$  and  $\Psi_H$  depends on stability conditions in the atmospheric boundary layer. When the atmosphere is stable, the SMAP model assumes that  $\Psi_M = \Psi_H$  and calculates the profile functions according to *Holtzlag and De Bruin* (1988), whereas the SMAP model carries out the calculations with functions determined by *Paulson* (1970) under unstable conditions.

Figure 5.12a shows the temporal changes of the 1 h averaged latent heat fluxes calculated from two-level atmospheric measurements using the 2LM (OBS\_2LM) compared to the result presented in Sect. 5.5 (OBS\_1LM) as well as original SMAP simulation result (SMAP\_1LM) presented in Sect. 5.4. Obviously, the result indicated that the latent heat flux from OBS\_1LM was almost compatible with the heat flux from SMAP\_1LM, implying that the OBS\_1LM is also likely to underestimate the latent heat flux. Comparison between OBS\_2LM and OBS\_1LM shows that the former obviously tends to be higher than the latter, and sometimes the signs of the fluxes are different. According to previous studies (*Box and Steffen, 2001; Cullen et al., 2014*), the sign and magnitude of the latent heat fluxes from the 1LM and 2LM methods agree reasonably at low elevations on the GrIS, whereas they often differ from each other at the higher elevations. Measurements conducted previously in the northwest GrIS (the Humboldt and GITS sites) showed that the net annual sublimation from the 1LM and 2LM methods did not agree sufficiently at both sites (*Box and Steffen, 2001*). In the former site, the sign was contrasting, while the magnitude was remarkably different at the latter site.

We next performed another numerical simulation with the SMAP model (SMAP\_2LM), where shortwave albedo and snow surface temperature were simulated with the same manner as performed in Sect. 5.4. In this case, the latent heat flux determined directly from the 2LM method was used only for the assessment of surface hoar formation, while that from the 1LM method was employed for a boundary condition of the governing one-dimensional diffusion equation in the SMAP model (*Niwano et al., 2012*). Figure 5.12b compares the surface snow grain size from the SMAP\_2LM case with the surface snow grain size from the SMAP\_1LM case and GRS. A difference between results of the SMAP\_2LM and SMAP\_1LM cases is apparent on 4 July (Fig. 5.12b), when snow grain size is lower for the SMAP\_2LM case than for the SMAP\_1LM case. The low grain size estimated with SMAP\_2LM ( $< 0.4$  mm) can be attributed to modeled surface hoar formation.

Actually, the latent heat flux simulated with OBS\_2LM on 4 July was positive (Fig. 5.12a), and the winds at 3 m above the surface around 4 July were calm (Fig. 5.2b). These conditions are suitable for modeled surface hoar formation, as explained in Sect. 5.4.3. Although SMAP\_2LM succeeded in reproducing the surface hoar detected at the SIGMA-A site during the IOP, which implies that the 2LM method calculated latent heat flux might be more probable than that from the 1LM method, there were still obvious discrepancies with GRS results around 2–5 July (Fig. 5.12b). To resolve this problem, it might be necessary to consider the possibility of a new snow grain size for surface hoar, which is now calculated as a function of air temperature in the same manner as new snowfall (Niwano *et al.*, 2012).

According to Box and Steffen (2001), the uncertainty of the 2LM method increases as the temperature, humidity, and wind speed differences between two measurement heights decrease. This motivated us to investigate the significance of the latent heat flux calculated by the 2LM method during IOP. In this inquiry, gradients (positive downward) of wind speed, temperature, and vapor pressure between the surface and the lower measurement height and between the lower and upper measurement height were investigated at first. Averaged gradients between the surface and the lower measurement height during the IOP were  $1.6 \text{ s}^{-1}$ ,  $0.3 \text{ }^{\circ}\text{C m}^{-1}$ , and  $-0.15 \text{ hPa m}^{-1}$ , respectively. The value for vapor pressure is very close to that obtained at Summit during 2000–2002 as reported by Cullen *et al.* (2014). However, averaged gradients between the lower and upper measurement heights were nearly 0, except for the case of wind speed, for which it was  $0.2 \text{ s}^{-1}$ . Focusing on the period from 00:10 to 00:20 UTC on 4 July when SMAP\_2LM detected the surface hoar, vapor pressure gradients showed opposite signs:  $-0.13 \text{ hPa m}^{-1}$  for the 1LM method and  $0.01 \text{ hPa m}^{-1}$  for the 2LM method. Although this result explains the reason why only the 2LM method succeeded in the surface hoar detection, the latter value is still very small. These make it difficult to assess uncertainties of the 2LM method caused by each sensor as expected. In fact, numerical sensitivity

studies with perturbed input parameters considering absolute accuracy of temperature, relative humidity, and wind speed sensors ( $\pm 0.2$  °C,  $\pm 2$  %, and  $\pm 0.3$  m s<sup>-1</sup>, respectively) in the 2LM calculation modified the picture of calculated turbulent heat fluxes drastically in any calculations. Even when relative differences in the accuracy of two sensors at the lower and upper measurement heights were considered (according to our relative calibration of the instruments performed in advance, air temperature and wind speed sensors at two levels showed no significant difference; however, as for relative humidity, the upper sensor tended to be lower by 1.2 % compared to the lower sensor), differences in calculated latent heat flux with perturbed input parameters were quite large as well. Therefore, we should conclude that underestimation of the latent heat flux calculated with the 1LM method is plausible, although the exact order of underestimation was quite hard to detect during this study period.

## **5.7. Conclusions**

In this study, we investigated the record near-surface melt event that occurred over the GrIS during the IOP (30 June to 14 July 2012) from the standpoint of the SEB. We used data measured in situ at the SIGMA-A site, where significant increases of air temperature, relative humidity, and downward long-wave radiant flux, as well as heavy rainfall and abrupt near-surface snowmelt, were observed beginning on 10 July. Although radiation-related components of the SEB could be determined from AWS data, other fluxes were not measured directly. We therefore employed the physical snowpack model SMAP to calculate the  $H_S$ ,  $H_L$ , and  $H_R$ . Because this was the first attempt to adapt the SMAP model to a polar region, we carried out a preliminary analysis of various aspects of the performance of the SMAP model. We calculated the snow temperature profile in the NSL, snow surface temperature, surface snow grain size, and shortwave albedo; we compared these calculated values with in situ measurements. In the numerical simulation, the initial conditions of the snow were specified from the snow pit measurements conducted on 30 June 2012, 16:45 UTC. The SMAP

model was subsequently driven by 5 min averaged meteorological data, including air pressure, air temperature, relative humidity, wind speed, and downward shortwave, near-infrared, and long-wave radiant fluxes. The SMAP model was also driven by the daily temperature at the bottom of the thick ice layer in the NSL, the mass concentrations of snow impurities obtained every other day, and 5 min averaged accumulated precipitation based on 3-hourly ERA-Interim reanalysis data corrected by in situ bucket measurements.

Validation results revealed that the RMSE for the snow temperature profile and snow surface temperature were reasonable. Regarding surface snow grain size, simulation results were compared against GRS data obtained from spectral albedo measurements post-processed with a GSAF algorithm. Although the RMSE and ME that we obtained were comparable in magnitude to those reported from previous model validation studies performed at Sapporo, Japan, the small snow grain size associated with the surface hoar observed during 3–5 July could not be simulated by the SMAP model. In the SMAP model, surface hoar is created when  $H_L$  is positive and the wind speed is less than  $3 \text{ m s}^{-1}$ . However, the simulated  $H_L$  from the night of 2 July to the morning of 5 July was continuously negative. Despite these discrepancies, the simulated shortwave albedo was in reasonable agreement with observations throughout the IOP (RMSE = 0.023 and ME = 0.008). The cause of the agreement between the simulated shortwave albedo and observations, even during the 3–5 July period when the SMAP model could not reproduce surface hoar and associated small near-surface snow grain size, was a decrease of the near-infrared fraction of the downward shortwave radiant flux caused by the appearance of low-level clouds during the IOP. This change in the shortwave radiant flux increased the influence of visible albedo and in turn decreased the effect of near-infrared albedo on the shortwave albedo. These physical processes are explicitly taken into account by the PBSAM, an important component of the SMAP model, which is an advantage of PBSAM.

Using the SMAP model, we investigated the SEB at the SIGMA-A site during the IOP. Radiation-related components of the SEB were directly given from the AWS measurements, whereas other components were calculated by the SMAP model as a function of measured snow surface temperature. The calculated SEB was clearly different between Period-1 (30 June to 9 July) and Period-2 (10 to 14 July):  $L_{net}$  increased dramatically by  $+57.1 \text{ W m}^{-2}$  ( $H_S$  and  $H_L$  also increased by  $+11.3$  and  $+25.2 \text{ W m}^{-2}$ , respectively) after 10 July, whereas  $S_{net}$  decreased significantly by  $-42.3 \text{ W m}^{-2}$ . Consequently,  $Q_{net}$  clearly varied diurnally (negative during the night and positive during the day) until 9 July. However, the fact that it remained continuously positive after 10 July explains the continuous melt event observed at the SIGMA-A site. We discussed the reason for this remarkable transition of radiative properties, and we concluded that it was caused by the appearance of low-level clouds accompanied by a significant temperature increase. The result was surface heating during Period-2 via the process of cloud radiative forcing in the polar region.

In order to confirm the validity of SEB characteristics during IOP, additional error analyses were conducted. During this process, it turned out that the sign of latent heat fluxes from the 1LM and 2LM methods differed especially when the surface hoar was observed (around 4 July). The former showed negative, while the latter turned positive and designated the surface hoar formation. Therefore, the latent heat flux calculated by the 2LM method seemed to be plausible; however, uncertainty involved in the 2LM method was so large that we could not confirm its significance.

## **Acknowledgements**

We sincerely thank Tetsuhide Yamasaki for logistical and field support of our expedition and Sakiko Daorana for her help during our stay at Qaanaaq, Greenland. We thank Climatec Inc. (Japan) for manufacturing the AWS installed at the SIGMA-A site and Masae Igosaki for supporting the laboratory measurements of snow impurities. We would like to thank two reviewers, John King and an anonymous referee, and the scientific editor of this paper, Michiel van den Broeke, for their

helpful comments and suggestions. This study was supported in part by (1) the Japan Society for the Promotion of Science (JSPS) grant-in-aid for scientific research (S) number 23221004, (2) the Global Change Observation Mission – Climate (GCOM-C)/the Second-generation GLobal Imager (SGLI) Mission, the Japan Aerospace Exploration Agency (JAXA), (3) the Experimental Research Fund for Global Environment Conservation, Ministry of the Environment of Japan, and (4) the Grant for Joint Research Program, Institute of Low Temperature Science, Hokkaido University. The map showing the location of site SIGMA-A (Fig. 5.1) was created by NunaGIS (<http://en.nunagis.gl/>) operated by Asiaq, Greenland Survey.



## 6. Summary and future outlook

In this work, we developed a multi-layered physical snowpack model called SMAP. The most notable feature of this model is that it incorporates a state-of-the-art physically based snow albedo model (PBSAM), which accurately calculates snow albedo and the solar heating profile in the snowpack by explicitly considering the effects of optically equivalent snow grain size and mass concentrations of snow impurities (Chapter 2). The SMAP model was equipped with an option that calculates vertical water transport in the snowpack with the Richards equation, which is one of most cutting-edge developments in the field of snow modeling (Chapter 3). The validity of the SMAP model was demonstrated by using data obtained at Sapporo, Nagaoka, and from the GrIS (Chapters 2, 3, 4, and 5).

Using the SMAP model together with in-situ atmospheric and snow measurements, we investigated snow-atmosphere interactions from various aspects. The key scientific findings highlighted in this thesis are as follows:

- Snowpack durations at Sapporo were shortened by 19 days during the winter of 2007–2008 and by 16 days during the winter of 2008–2009 due to radiative forcings caused by snow impurities including BC and dust. The estimated radiative forcings due to these snow impurities during the accumulation periods were  $3.7 \text{ W m}^{-2}$  (corresponding to an albedo reduction of 0.05) and  $3.2 \text{ W m}^{-2}$  (corresponding to an albedo reduction of 0.05) for the winters of 2007–2008 and 2008–2009, respectively. During the ablation periods, the radiative forcings were enhanced significantly for each winter:  $25.9 \text{ W m}^{-2}$  (albedo reduction of 0.18) and  $21.0 \text{ W m}^{-2}$  (albedo reduction of 0.17), respectively (Chapter 2).
- The ideal condition for enhanced ablation during the winters of 2005–2015 at Sapporo was found to be sunny weather in the daytime, which can induce surface heating and a resulting albedo reduction through snow grain growth via wet snow metamorphism (Chapter 4).

- Examination of the SEB components calculated by the SMAP model forced by in-situ measurements demonstrated that the main cause of the melt event observed at SIGMA-A on the northwest GrIS during the 2012 record surface melt event was attributed to low-level clouds accompanied by a significant temperature increase. These conditions induced a remarkable surface heating via cloud radiative forcing in the polar region (Chapter 5).

Finally, we briefly describe the future outlook for studies using the SMAP model. Above all, it is necessary to replace simple empirical parameterizations incorporated in the SMAP model (e.g., those for new snow density, new snow grain size, and effective thermal conductivity of snow; Chapter 2) by physical-based schemes, which could be developed through innovative in-situ measurements or laboratory experiments. In addition, improving the accuracy of model simulations by employing the data assimilation technique for the Crocus model, as in *Dumont et al. (2012)*, would be a plausible study in the era of “big data.” After every new model development, the model should be applied to as many different climate conditions as possible in order to increase the reliability of the model. At the same time, coupling the SMAP model with an atmospheric model would also extend the potential usefulness of the model. This would allow us to investigate the feedback mechanisms between the snowpack and the atmosphere in a closed system. Such an attempt to couple a detailed physical snowpack model with a regional or global model is still limited (e.g., Fettweis, 2007; Dumont et al., 2014). The ultimate goal of this work is to provide reliable future long-term (climatic) as well as short-term predictions on the physical state of snow and ice using the SMAP model.

## References

- Andersen, M., Stenseng, L., Skourup, H., Colgan, W., Khan, S., Kristensen, S., Andersen, S., Box, J., Ahlstrøm, A., Fettweis, X., Forsberg, R.: Basin-scale partitioning of Greenland ice sheet mass balance components (2007–2011). *Earth Planet Sci. Lett.*, **409**, 89–95, doi:10.1016/j.epsl.2014.10.015, 2015.
- Anderson, P. S.: A method for rescaling humidity sensors at temperatures well below freezing, *J. Atmos. Ocean. Tech.*, **11**, 1388–1391, doi:10.1175/1520-0426(1994)011<1388:AMFRHS>2.0.CO;2, 1994.
- Anderson, E. A.: A point energy and mass balance model of a snow cover, NOAA Tech. Rep. NWS19, Office of Hydrology, National Weather Service, Silver Spring, Maryland, USA, 1976.
- Andreas, E. L.: A theory for the scalar roughness and the scalar transfer coefficients over snow and ice, *Bound.-Lay. Meteorol.*, **38**, 159–184, doi:10.1007/BF00121562, 1987.
- Andreas, E. L.: Parameterizing scalar transfer over snow and ice: A review, *J. Hydrometeorol.*, **3**, 417–432, doi:10.1175/1525-7541(2002)003<0417:PSTOSA>2.0.CO;2, 2002.
- Aoki, T. and Yamanouchi, T.: Cloud radiative forcing around Asuka Station, Antarctica, *Proc. NIPR Symp. Polar Meteorol. Glaciol.*, 12–13 July 1990, Tokyo, 76–89, 1992.
- Aoki, T., Aoki, T., Fukabori, M., and Uchiyama, A.: Numerical simulation of the atmospheric effects on snow albedo with multiple scattering radiative transfer model for the atmosphere-snow system, *J. Meteorol. Soc. Jpn.*, **77**, 595–614, 1999.
- Aoki, T., Aoki, T., Fukabori, M., Hachikubo, A., Tachibana, Y., and Nishio, F.: Effects of snow physical parameters on spectral albedo and bidirectional reflectance of snow surface, *J. Geophys. Res.*, **105**, 10219–10236, doi:10.1029/1999JD901122, 2000.
- Aoki, T., Hachikubo, A., and Hori, M.: Effects of snow physical parameters on shortwave broadband albedos, *J. Geophys. Res.*, **108(D19)**, 4616, doi:10.1029/2003JD003506, 2003.

- Aoki, T., Motoyoshi, H., Kodama, Y., Yasunari, T. J., Sugiura, K., and Kobayashi, H.: Atmospheric aerosol deposition on snow surfaces and its effect on albedo, *SOLA*, **2**, 013–016, doi:10.2151/sola.2006-004, 2006.
- Aoki, T., Motoyoshi, H., Kodama, Y., Yasunari, T. J., and Sugiura, K.: Variations of the snow physical parameters and their effects on albedo in Sapporo, Japan, *Ann. Glaciol.*, **46**, 375–381, doi:10.3189/172756407782871747, 2007a.
- Aoki, T., Hori, M., Motoyoshi, H., Tanikawa, T., Hachikubo, A., Sugiura, K., Yasunari, T. J., Stordvold, R., Eide, H. A., Stamnes, K., Li, W., Nieke, J., Nakajima, Y., and Takahashi, F.: ADEOS-II/GLI snow/ice products – Part II: Validation results using GLI and MODIS data, *Remote Sens. Environ.*, **111**, 274–290, doi:10.1016/j.rse.2007.02.035, 2007b.
- Aoki, T., Kuchiki, K., Niwano, M., Kodama, Y., Hosaka, M., and Tanaka, T.: Physically based snow albedo model for calculating broadband albedos and the solar heating profile in snowpack for general circulation models, *J. Geophys. Res.*, **116**, D11114, doi:10.1029/2010JD015507, 2011.
- Aoki, T., Matoba, S., Uetake, J., Takeuchi, N., and Motoyama, H.: Field activities of the “Snow Impurity and Glacial Microbe effects on abrupt warming in the Arctic” (SIGMA) Project in Greenland in 2011–2013, *Bull. Glaciol. Res.*, **32**, 3–20, doi:10.5331/bgr.32.3, 2014a.
- Aoki, T., Matoba, S., Yamaguchi, S., Tanikawa, T., Niwano, M., Kuchiki, K., Adachi, K., Uetake, J., Motoyama, H., and Hori, M.: Light-absorbing snow impurity concentrations measured on Northwest Greenland ice sheet in 2011 and 2012, *Bull. Glaciol. Res.*, **32**, 21–31, doi:10.5331/bgr.32.21, 2014b.
- Armstrong, R. L. and Brun, E. (Eds.): *Snow and Climate: Physical Processes, Surface Energy Exchange and Modeling*. Cambridge Univ. Press, Cambridge, U. K., 2008.
- Bader, H.-P., and Weilenmann, P.: Modeling temperature distribution, energy and mass flow in a (phase-changing) snowpack. I. Model and case studies, *Cold Reg. Sci. Technol.*, **20**, 157–181,

- doi:10.1016/0165-232X(92)90015-M, 1992.
- Bartelt, P. and Lehning, M.: A physical SNOWPACK model for the Swiss avalanche warning, Part I: numerical model, *Cold Reg. Sci. Technol.*, **35**, 123–145, doi:10.1016/S0165-232X(02)00074-5, 2002.
- Beljaars, A. C. M., and Holtslag, A. A. M.: Flux parameterization over land surfaces for atmospheric models, *J. Appl. Meteorol.*, **30**, 327–341, doi:10.1175/1520-0450(1991)030<0327:FPOLSF>2.0.CO;2, 1991.
- Bennartz, R., Shupe, M. D., Turner, D. D., Walden, V. P., Steffen, K., Cox, C. J., Kulie, M. S., Miller, N. B., and Pettersen, C.: July 2012 Greenland melt extent enhanced by low-level liquid clouds, *Nature*, **496**, 83–86, doi:10.1038/nature12002, 2013.
- Bonne, J.-L., Steen-Larsen, H. C., Risi, C., Werner, M., Sodemann, H., Lacour, J.-L., Fettweis, X., Cesana, G., Delmotte, M., Cattani, O., Vallelonga, P., Kjær, H. A., Clerbaux, C., Sveinbjörnsdóttir, Á. E., and Masson-Delmotte, V.: The summer 2012 Greenland heat wave: In situ and remote sensing observations of water vapor isotopic composition during an atmospheric river event, *J. Geophys. Res.-Atmos.*, **120**, 2970–2989, doi:10.1002/2014JD022602, 2015.
- Boone, A. and Etchevers, P.: An Intercomparison of Three Snow Schemes of Varying Complexity Coupled to the Same Land Surface Model: Local-Scale Evaluation at an Alpine Site, *J. Hydrometeor.*, **2**, 374–394, doi:10.1175/1525-7541(2001)002<0374:AIOTSS>2.0.CO;2, 2001.
- Box, J. E. and Steffen, K.: Sublimation on the Greenland ice sheet from automated weather station observations, *J. Geophys. Res.*, **106**, 33965–33981, doi:10.1029/2001JD900219, 2001.
- Box, J. E., Fettweis, X., Stroeve, J. C., Tedesco, M., Hall, D. K., and Steffen, K.: Greenland ice sheet albedo feedback: thermodynamics and atmospheric drivers, *The Cryosphere*, **6**, 821–839, doi:10.5194/tc-6-821-2012, 2012.
- Braithwaite, R. J.: Aerodynamic stability and turbulent sensible-heat flux over a melting ice surface,

- the Greenland ice sheet, *J. Glaciol.*, **41**, 562–571, 1995.
- Brandt, R. E., Warren, S. G., and Clarke, A. D.: A controlled snowmaking experiment testing the relation between black carbon content and reduction of snow albedo, *J. Geophys. Res.*, **116**, D08109, doi:10.1029/2010JD015330, 2011.
- Brock, B. W., Willis, I. C., and Sharp, M. J.: Measurement and parameterization of aerodynamic roughness length variations at Haut Glacier d’Arolla, Switzerland, *J. Glaciol.*, **52**, 281–297, 2006.
- Brown, R. D. and Mote, P. W.: The response of Northern Hemisphere snow cover to a changing climate, *J. Climate*, **22**, 2124–2145. doi:10.1175/2008JCLI2665.1, 2009.
- Brown, R. D. and Robinson, D. A.: Northern Hemisphere spring snow cover variability and change over 1922–2010 including an assessment of uncertainty, *The Cryosphere*, **5**, 219–229, doi:10.5194/tc-5-219-2011, 2011.
- Brun, E., Martin, E., Simon, V., Gendre, C., and Coléou, C.: An energy and mass model of snow cover suitable for operational avalanche forecasting, *J. Glaciol.*, **35**, 333–342, 1989.
- Brun, E., David, P., Sudul, M., and Brunot, G.: A numerical model to simulate snow-cover stratigraphy for operational avalanche forecasting, *J. Glaciol.*, **38**, 13–22., 1992.
- Brun, E., Six, D., Picard, G., Vionnet, V., Arnaud, L., Bazile, E., Boone, A., Bouchard, A., Genthon, C., Guidard, V., Le Moigne, P., Rabier, F. and Seity, Y.: Snow/atmosphere coupled simulation at Dome C, Antarctica, *J. Glaciol.*, **57**, 721–736, doi:10.3189/002214311797409794, 2011.
- Budyko, M. I.: The effect of solar radiation variations on the climate of the Earth, *Tellus*, **21**, 611–619, doi:10.1111/j.2153-3490.1969.tb00466.x, 1969.
- Carmagnola, C. M., Morin, S., Lafaysse, M., Domine, F., Lesaffre, B., Lejeune, Y., Picard, G., and Arnaud, L.: Implementation and evaluation of prognostic representations of the optical diameter of snow in the SURFEX/ISBA-Crocus detailed snowpack model, *The Cryosphere*, **8**, 417–437, doi:10.5194/tc-8-417-2014, 2014.

- Chen, L., Johannessen, O. M., Huijum, W., and Ohmura, A.: Accumulation over the Greenland Ice Sheet as represented in reanalysis data, *Adv. Atmos. Sci.*, **28**, 1–9, doi:10.1007/s00376-010-0150-9, 2011.
- Cheng, Y., Parlange, M. B., and Brutsaert, W.: Pathology of Monin-Obukhov similarity in the stable boundary layer, *J. Geophys. Res.*, **110**, D06101, doi:10.1029/2004JD004923, 2005.
- Colbeck, S. C.: Grain and bond growth in wet snow, *IAHS Publ.*, **114**, 51–56, 1975.
- Cullen, N. J. and Steffen, K.: Unstable near-surface boundary conditions in summer on top of the Greenland Ice Sheet, *Geophys. Res. Lett.*, **28**, 4491–4493, doi:10.1029/2001GL013417, 2001.
- Cullen, N. J., Mölg, T., Conway, J., and Steffen, K.: Assessing the role of sublimation in the dry snow zone of the Greenland ice sheet in a warming world, *J. Geophys. Res.-Atmos.*, **119**, 6563–6577, doi:10.1002/2014JD021557, 2014.
- Cullen, N. J., and Conway, J. P.: A 22 month record of surface meteorology and energy balance from the ablation zone of Brewster Glacier, New Zealand. *J. Glaciol.*, **61**, 931–946. doi:10.3189/2015JoG15J004, 2015.
- Dadic, R., Schneebeli, M., Lehning, M., Hutterli, M. A., and Ohmura, A.: Impact of the microstructure of snow on its temperature: a model validation with measurements from Summit, Greenland, *J. Geophys. Res.*, **113**, D14303, doi:10.1029/2007JD009562, 2008.
- Dee, D. P., Uppala, S. M., Simmons, A. J., Berrisford, P., Poli, P., Kobayashi, S., Andrae, U., Balmaseda, M. A., Balsamo, G., Bauer, P., Bechtold, P., Beljaars, A. C. M., van de Berg, L., Bidlot, J., Bormann, N., Delsol, C., Dragani, R., Fuentes, M., Geer, A. J., Haimberger, L., Healy, S. B., Hersbach, H., Hólm, E. V., Isaksen, L., Kållberg, P., Köhler, M., Matricardi, M., McNally, A. P., Monge-Sanz, B. M., Morcrette, J.-J., Park, B.-K., Peubey, C., de Rosnay, P., Tavolato, C., Thépaut, J.-N., and Vitart, F.: The ERA-Interim reanalysis: configuration and performance of the data assimilation system, *Q. J. Roy. Meteorol. Soc.*, **137**, 553–597, doi:10.1002/qj.828, 2011.

- Denoth, A.: An electronic device for long-term snow wetness recording, *Ann. Glaciol.*, **19**, 104–106, doi:10.3189/172756404781815121, 1994.
- Derksen, C., and Brown, R.: Spring snow cover extent reductions in the 2008–2012 period exceeding climate model projections, *Geophys. Res. Lett.*, **39**, L19504, doi:10.1029/2012GL053387, 2012.
- Devaux, J.: L'économie radio-thermique des champs de neige et des glaciers, *Ann. Phys.*, **20**, 5–67, 1933.
- Dobbins, R. A., and Jizmagian, G. S.: Optical scattering cross sections for polydispersions of dielectric spheres, *J. Opt. Soc. Am.*, **56**, 1345–1349, doi:10.1364/JOSA.56.001345, 1966.
- Dumont, M., Durand, Y., Arnaud, Y., and Six, D.: Variational assimilation of albedo in a snowpack model and reconstruction of the spatial mass-balance distribution of an alpine glacier, *J. Glaciol.*, **58**, 151–164, doi:10.3189/2012JoG11J163, 2012.
- Dumont, M., Brun, E., Picard, G., Michou, M., Libois, Q., Petit, J., Geyer, M., Morin, S., Josse, B.: Contribution of light-absorbing impurities in snow to Greenland's darkening since 2009, *Nat. Geosci.*, **7**, 509–512, doi:10.1038/ngeo2180, 2014.
- Enderlin, E. M., Howat, I. M., Jeong, S., Noh, M.-J., van Angelen, J. H., and van den Broeke, M. R.: An improved mass budget for the Greenland ice sheet, *Geophys. Res. Lett.*, **41**, 866–872, doi:10.1002/2013GL059010, 2014.
- Essery, R., Martin, E., Douville, H., Fernández, A., and Brun, E.: A comparison of four snow models using observations from an alpine site, *Clim. Dyn.*, **15**, 583–593, doi:10.1007/s003820050302, 1999.
- Etchevers, P., Martin, E., Brown, R., et al.: Validation of the energy budget of an alpine snowpack simulated by several snow models (SnowMIP project), *Ann. Glaciol.* **38**, 150–158, 2004.
- Ettema, J., van den Broeke, M. R., van Meijgaard, E., van de Berg, W. J., Box, J. E., and Steffen, K.: Climate of the Greenland ice sheet using a high-resolution climate model – Part 1: Evaluation,



- The Cryosphere*, **4**, 511–527, doi:10.5194/tc-4-511-2010, 2010a.
- Ettema, J., van den Broeke, M. R., van Meijgaard, E., and van de Berg, W. J.: Climate of the Greenland ice sheet using a high-resolution climate model – Part 2: Near-surface climate and energy balance, *The Cryosphere*, **4**, 529–544, doi:10.5194/tc-4-529-2010, 2010b.
- Fettweis, X.: Reconstruction of the 1979–2006 Greenland ice sheet surface mass balance using the regional climate model MAR, *The Cryosphere*, **1**, 21–40, doi:10.5194/tc-1-21-2007, 2007.
- Fettweis, X., Tedesco, M., van den Broeke, M., and Ettema, J.: Melting trends over the Greenland ice sheet (1958–2009) from spaceborne microwave data and regional climate models, *The Cryosphere*, **5**, 359–375, doi:10.5194/tc-5-359-2011, 2011.
- Fettweis, X., Hanna, E., Lang, C., Belleflamme, A., Erpicum, M., and Gallée, H.: Brief communication "Important role of the mid-tropospheric atmospheric circulation in the recent surface melt increase over the Greenland ice sheet", *The Cryosphere*, **7**, 241–248, doi:10.5194/tc-7-241-2013, 2013.
- Fierz, C. and Lehning, M.: Assessment of the microstructure-based snow-cover model SNOWPACK: thermal and mechanical properties, *Cold Reg. Sci. Technol.*, **33**, 123–131, doi:10.1016/S0165-232X(01)00033-7, 2001.
- Fierz, C., Armstrong, R. L., Durand, Y., Etchevers, P., Greene, E., McClung, D. M., Nishimura, K., Satyawali, P. K., and Sokratov, S. A.: The International Classification for Seasonal Snow on the Ground, IHP-VII Technical Documents in Hydrology N\_83, IACS Contribution N\_1, UNESCO-IHP, Paris, viii, 80 pp., 2009.
- Flanner, M. G., and Zender, C. S.: Snowpack radiative heating: Influence on Tibetan plateau climate, *Geophys. Res. Lett.*, **32**, L06501, doi:10.1029/2004GL022076, 2005.
- Flanner, M. G., and Zender, C. S.: Linking snowpack microphysics and albedo evolution, *J. Geophys. Res.*, **111**, D12208, doi:10.1029/2005JD006834, 2006.

- Flanner, M. G., Zender, C. S., Randerson, J. T., and Rasch, P. J.: Present-day climate forcing and response from black carbon in snow, *J. Geophys. Res.*, **112**, D11202, doi:10.1029/2006JD008003, 2007.
- Föhn, P. M. B.: Simulation of surface-hoar layers for snow-cover models, *Ann. Glaciol.*, **32**, 19–26, doi:10.3189/172756401781819490, 2001.
- Forland, E., Allerup, P., Dahlström, B., Elomaa, E. T., Perälä, J., Rissanen, P., Vedin, H., and Vejen, F.: Manual for operational correction of Nordic precipitation data, Tech. rep., Det Norske Meteorologiske Institutt., 1996.
- Galperin, B., Sukoriansky, S., and Anderson, P. S.: On the critical Richardson number in stably stratified turbulence, *Atmos. Sci. Lett.*, **8**, 65–69, doi:10.1002/asl.153, 2007.
- Gardner, A. S., and Sharp, M. J.: A review of snow and ice albedo and the development of a new physically based broadband albedo parameterization, *J. Geophys. Res.*, **115**, F01009, doi:10.1029/2009JF001444, 2010.
- Garratt, J. R.: The Atmospheric Boundary Layer, Cambridge Univ. Press, Cambridge, U. K, 1992.
- Giddings, J. C., and LaChapelle, E.: Diffusion theory applied to radiant energy distribution and albedo of snow, *J. Geophys. Res.*, **66**, 181–189, doi:10.1029/JZ066i001p00181, 1961.
- Giesen, R. H., Andreassen, L. M., van den Broeke, M. R., and Oerlemans, J.: Comparison of the meteorology and surface energy balance at Storbreen and Midtdalsbreen, two glaciers in southern Norway, *The Cryosphere*, **3**, 57–74, doi:10.5194/tc-3-57-2009, 2009.
- Giesen R. H., Andreassen, L. M., Oerlemans, J., and van den Broeke, M. R.: Surface energy balance in the ablation zone of Langfjordjøkelen, an arctic, maritime glacier in northern Norway, *J. Glaciol.*, **60**, 57–70, doi:10.3189/2014JoG13J063, 2014.
- Goudriaan, J.: Crop Micrometeorology: A Simulation Study, Pudoc, Wageningen, Netherlands, 1977.
- Grachev, A. A., Andreas, E. L., Fairall, C. W., Guest, P. S., and Persson, P. O. G.: SHEBA flux-profile

- relationships in the stable atmospheric boundary layer, *Boundary Layer Meteorol.*, **124**, 315–333, doi:10.1007/s10546-007-9177-6, 2007.
- Grenfell, T. C., and Warren, S. G.: Representation of a nonspherical ice particle by a collection of independent spheres for scattering and absorption of radiation, *J. Geophys. Res.*, **104(D24)**, 31,697–31,709, doi:10.1029/1999JD900496, 1999.
- Grenfell, T. C., Neshyba, S. P., and Warren, S. G.: Representation of a nonspherical ice particle by a collection of independent spheres for scattering and absorption of radiation: 3. Hollow columns and plates, *J. Geophys. Res.*, **110**, D17203, doi:10.1029/2005JD005811, 2005.
- Greuell, W. and Konzelmann, T.: Numerical modelling of the energy balance and the englacial temperature of the Greenland Ice Sheet. Calculations for the ETH-Camp location (West Greenland, 1155ma.s.l.), *Global Planet. Change*, **9**, 91–114, doi:10.1016/0921-8181(94)90010-8, 1994.
- Groot Zwaafink, C. D., Cagnati, A., Crepaz, A., Fierz, C., Macelloni, G., Valt, M. and Lehning, M.: Event-driven deposition of snow on the Antarctic Plateau: analyzing field measurements with SNOWPACK, *The Cryosphere*, **7**, 333–347, doi:10.5194/tc-7-333-2013, 2013.
- Hachikubo, A.: Numerical modelling of sublimation on snow and comparison with field measurements, *Ann. Glaciol.*, **32**, 27–32, doi:10.3189/172756401781819265, 2001.
- Hall, A.: The role of surface albedo feedback in climate, *J. Clim.*, **17**, 1550–1568, doi:10.1175/1520-0442(2004)017<1550:TROSAF>2.0.CO;2, 2004.
- Hall, D. K., Comiso, J. C., DiGirolamo, N. E., Shuman, C. A., Box, J. E., and Koenig, L. S.: Variability in the surface temperature and melt extent of the Greenland ice sheet from MODIS, *Geophys. Res. Lett.*, **40**, 2114–2120, doi:10.1002/grl.50240, 2013.
- Hanna, E., Fettweis, X., Mernild, S. H., Cappelen, J., Ribergaard, M. H., Shuman, C. A., Steffen, K., Wood, L., and Mote, T. L.: Atmospheric and oceanic climate forcing of the exceptional

- Greenland ice sheet surface melt in summer 2012, *Int. J. Climatol.*, **34**, 1022–1037, doi:10.1002/joc.3743, 2014.
- Hansen, J., and Nazarenko, L.: Soot climate forcing via snow and ice albedos, *Proc. Natl. Acad. Sci. U. S. A.*, **101**, 423–428, doi:10.1073/pnas.2237157100, 2004.
- Helgason, W. and Pomeroy, J.: Problems closing the energy balance over a homogeneous snow cover during midwinter, *J. Hydrometeorol.*, **13**, 557–572, doi:10.1175/JHM-D-11-0135.1, 2012.
- Hirashima, H., Nishimura, K., Baba, E., Hachikubo, A. and Lehning, M.: SNOWPACK model simulation for snow in Hokkaido, Japan, *Ann. Glaciol.*, **38**, 123–129, doi:10.3189/172756404781815121, 2004.
- Hirashima, H., Nishimura, K., Yamaguchi, S., Sato, A., Lehning, M.: Avalanche forecasting in a heavy snowfall area using the snowpack model, *Cold. Reg. Sci. Technol.*, **51**, 191–203, doi:10.1016/j.coldregions.2007.05.013, 2008.
- Hirashima, H., Yamaguchi, S., Sato, A. and Lehning, M.: Numerical modeling of liquid water movement through layered snow based on new measurements of the water retention curve, *Cold. Reg. Sci. Technol.*, **64**, 94–103, doi:10.1016/j.coldregions.2010.09.003, 2010.
- Holland, M. M., Bitz, C. M.: Polar amplification of climate change in coupled models, *Clim. Dyn.*, **21**, 221–232, doi:10.1007/s00382-003-0332-6, 2003.
- Holtzlag, A. A. M., and De Bruin, H. A. R.: Applied modeling of the nighttime surface energy balance over land, *J. Appl. Meteorol.*, **27**, 689–704, doi:10.1175/1520-0450(1988)027<0689:AMOTNS>2.0.CO;2, 1988.
- Ishimoto, H., Masuda, K., Mano, Y., Orikasa, N., and Uchiyama, A.: Irregularly shaped ice aggregates in optical modeling of convectively generated ice clouds, *J. Quant. Spectrosc. Ra.*, **113**, 632–643, doi:10.1016/j.jqsrt.2012.01.017, 2012.
- Iwata, Y., Hayashi, M., Suzuki, S., Hirota, T., and Hasegawa, S.: Effects of snow cover on soil freezing,

- water movement, and snowmelt infiltration: A paired plot experiment, *Water Resour. Res.*, **46**, W09504, doi:10.1029/2009WR008070, 2010a.
- Iwata, Y., Hirota, T., Hayashi, M., Suzuki, S. and Hasegawa, S.: Effects of frozen soil and snow cover on cold-season soil water dynamics in Tokachi, Japan, *Hydrol. Process.*, **24**, 1755–1765. doi:10.1002/hyp.7621, 2010b.
- Jacobi, H.-W., Domine, F., Simpson, W. R., Douglas, T. A. and Sturm, M.: Simulation of the specific surface area of snow using a one-dimensional physical snowpack model: Implementation and evaluation for subarctic snow in Alaska, *The Cryosphere*, **4**, 35–51, doi:10.5194/tc-4-35-2010, 2010.
- Jacobi, H.-W., Lim, S., Ménégoz, M., Ginot, P., Laj, P., Bonasoni, P., Stocchi, P., Marinoni, A., and Arnaud, Y.: Black carbon in snow in the upper Himalayan Khumbu Valley, Nepal: observations and modeling of the impact on snow albedo, melting, and radiative forcing, *The Cryosphere*, **9**, 1685–1699, doi:10.5194/tc-9-1685-2015, 2015.
- Jansson, P.-E. and Karlberg, L.: Coupled Heat and Mass Transfer Model for Soil-Plant-Atmosphere Systems. Department of Civil and Environmental Engineering, Royal Institute of Technology, Engineering, Stockholm, Sweden, 2001.
- Jones, P. D., New, M., Parker, D. E., Martin, S. and Rigor, I. G.: Surface air temperature and its changes over the past 150 years, *Rev. Geophys.*, **37(2)**, 173–199, doi:10.1029/1999RG900002, 1999.
- Jordan, R.: A one-dimensional temperature model for a snow cover: Technical documentation for SNTHERM.89, Spec.Rep. 91–16, U.S. Army Cold Reg. Res. and Eng. Lab., Hanover, N. H, 1991.
- Jordan, R., Andreas, E. L., and Makshtas, A. P.: Heat budget of snowcovered sea ice at North Pole 4, *J. Geophys. Res.*, **104(C4)**, 7785–7806. doi:10.1029/1999JC900011, 1999.
- Kaempfer, T. U., Schneebeli, M., and Sokratov, S. A.: A microstructural approach to model heat

- transfer in snow, *Geophys. Res. Lett.*, **32**, L21503, doi:10.1029/2005GL023873, 2005.
- Kajikawa, M.: Relationship between new snow density and shape of snow crystals (in Japanese with English abstract), *Seppyo*, **51**, 178–183, 1989.
- Khan, S. A., Wahr, J., Bevis, M., Velicogna, I., and Kendrick, E.: Spread of ice mass loss into northwest Greenland observed by GRACE and GPS, *Geophys. Res. Lett.*, **37**, L06501, doi:10.1029/2010GL042460, 2010.
- King, J. C., Gadian, A., Kirchgaessner, A., Kuipers Munneke, P., Lachlan-Cope, T. A., Orr, A., Reijmer, C., van den Broeke, M. R., van Wessem, J. M., and Weeks, M.: Validation of the summertime surface energy budget of Larsen C Ice Shelf (Antarctica) as represented in three high-resolution atmospheric models, *J. Geophys. Res.-Atmos.*, **120**, 1335–1347, doi:10.1002/2014JD022604, 2015.
- Kondo, J.: Meteorology of the Water Environment–Water and Heat Balance of the Earth’s Surface [in Japanese], Asakura Shoten, Tokyo, 1994.
- Kondo, J., and Yamazawa, H.: Bulk transfer coefficient over a snow surface, *Boundary Layer Meteorol.*, **34**, 123–135, doi:10.1007/BF00120912, 1986.
- Kondo, J., Kanechika, O., and Yasuda, N.: Heat and momentum transfers under strong stability in the atmospheric surface layer, *J. Atmos. Sci.*, **35**, 1012–1021, doi:10.1175/1520-0469(1978)035<1012:HAMTUS>2.0.CO;2, 1978.
- Kuchiki, K., Aoki, T., Tanikawa, T., and Kodama, Y.: Retrieval of snow physical parameters using a ground-based spectral radiometer, *Appl. Opt.*, **48**, 5567–5582, doi:10.1364/AO.48.005567, 2009.
- Kuchiki, K., Aoki, T., Niwano, M., Matoba, S., Kodama, Y., and Adachi, K.: Elemental carbon, organic carbon, and dust concentrations in snow measured with thermal optical and gravimetric methods: Variations during the 2007–2013 winters at Sapporo, Japan, *J. Geophys. Res. Atmos.*, **120**, 868–882, doi:10.1002/2014JD022144, 2015.

- Kudo, R., Uchiyama, A., Ijima, O., Ohkawara, N., and Ohta, S.: Aerosol impact on the brightening in Japan, *J. Geophys. Res.*, **117**, D07208, doi:10.1029/2011JD017158, 2012.
- Kuipers Munneke, P., van den Broeke, M. R., Reijmer, C. H., Helsen, M. M., Boot, W., Schneebeli, M., and Steffen, K.: The role of radiation penetration in the energy budget of the snowpack at Summit, Greenland, *The Cryosphere*, **3**, 155–165, doi:10.5194/tc-3-155-2009, 2009.
- Kuipers Munneke, P., van den Broeke, M. R., Lenaerts, J. T. M., Flanner, M. G., Gardner, A. S., and van de Berg, W. J.: A new albedo parameterizaion for use in climate models over the Antarctic ice sheet, *J. Geophys. Res.*, **116**, D05114, doi:10.1029/2010JD015113, 2011.
- Kuipers Munneke, P., van den Broeke, M. R., King, J. C., Gray, T., and Reijmer, C. H.: Near-surface climate and surface energy budget of Larsen C ice shelf, Antarctic Peninsula, *The Cryosphere*, **6**, 353–363, doi:10.5194/tc-6-353-2012, 2012.
- Langlois, A., Brucker, L., Kohn, J., Royer, A., Derksen, C., Cliche, P., Picard, G., Willemet, J. M., and Fily, M.: Simulation of snow water equivalent (SWE) using thermodynamic snow models in Québec, Canada, *J. Hydrometeorol.*, **10**, 1447–1463, doi:10.1175/2009JHM1154.1, 2009.
- Lehning, M., Bartelt, P., Brown, B., Fierz, C., and Satyawali, P.: A physical SNOWPACK model for the Swiss avalanche warning Part II: Snow microstructure, *Cold Reg. Sci. Technol.*, **35**, 147–167, doi:10.1016/S0165-232X(02)00073-3, 2002a.
- Lehning, M., Bartelt, P., Brown, B., and Fierz, C.: A physical SNOWPACK model for the Swiss avalanche warning Part III: Meteorological forcing, thin layer formation and evaluation, *Cold Reg. Sci. Technol.*, **35**, 169–184, doi:10.1016/S0165-232X(02)00072-1, 2002b.
- Liljequist, G. H.: Energy Exchanges of an Antarctic Snow-Field: Short-Wave Radiation, Norwegian-British-Swedish Antarctic Expedition (Maudheim, 71°30'S, 10°56'W), 1949–52, Scientific Results, Vol. 2, Part 1A, Norsk Polarinstitut, Oslo, 107 pp., 1956.
- Loth, B., and Graf, H.-F.: Modeling the snow cover in climate studies. Part II: The sensitivity to

- internal snow parameters and interface processes, *J. Geophys. Res.*, **103(D10)**, 11,329–11,340, doi:10.1029/97JD01412, 1998.
- Loth, B., Graf, H.-F., and Oberhuber, J. M.: Snow cover model for global climate simulations, *J. Geophys. Res.*, **98(D6)**, 10,451–10,464, doi:10.1029/93JD00324, 1993.
- Lundy, C. C., Brown, R. L., Adams, E. E., Birkeland, K. W. and Lehning, M.: A statistical validation of the snowpack model in a Montana climate, *Cold Reg. Sci. Technol.*, **33**, 237–246, doi:10.1016/S0165-232X(01)00038-6, 2001.
- Mahrt, L.: Stratified atmospheric boundary layers, *Boundary Layer Meteorol.*, **90**, 375–396, doi:10.1023/A:1001765727956, 1999.
- Mahrt, L.: Bulk formulation of surface fluxes extended to weakwind stable conditions, *Q. J. R. Meteorol. Soc.*, **134**, 1–10, doi:10.1002/qj.197, 2008.
- Marks, D., Kimball, J., Tingey, D., and Link, T.: The sensitivity of snowmelt processes to climate conditions and forest cover during rain-on-snow: A case study of the 1996 Pacific Northwest flood, *Hydrol. Processes*, **12**, 1569–1587, doi:10.1002/(SICI)1099-1085(199808/09)12:10/11<1569::AID-HYP682>3.0.CO;2-L, 1998.
- Martin, E. and Lejeune, Y.: Turbulent fluxes above the snow surface, *Ann. Glaciol.*, **26**, 179–183, 1998.
- Morin, S., Lejeune, Y., Lesaffre, B., Panel, J.-M., Poncet, D., David, P., and Sudul, M.: An 18-yr long (1993–2011) snow and meteorological dataset from a mid-altitude mountain site (Col de Porte, France, 1325 m alt.) for driving and evaluating snowpack models, *Earth Syst. Sci. Data*, **4**, 13–21, doi:10.5194/essd-4-13-2012, 2012.
- Morin, S., Domine, F., Dufour, A., Lejeune, Y., Lesaffre, B., Willemet, J.-M., Carmagnola, C. M., Jacobi, H.-W.: Measurements and modeling of the vertical profile of specific surface area of an alpine snowpack, *Adv. Water. Resour.*, **55**, 111–120, doi:10.1016/j.advwatres.2012.01.010, 2013.
- Morris, E. M., Bader, H.-P. and Weilenmann, P.: Modelling temperature variations in polar snow using



- DAISY, *J. Glaciol.*, **43**, 180–191. 1997.
- Motoyoshi, H., Aoki, T., Hori, M., Abe, O., and Mochizuki, S.: Possible effect of anthropogenic aerosol deposition on snow albedo reduction at Shinjo, Japan, *J. Meteorol. Soc. Jpn.*, **83A**, 137–148, doi:10.2151/jmsj.83A.137, 2005.
- National Research Institute for Earth Science and Disaster Prevention, Japan.: Data on Snow Cover in Nagaoka (34) (2011/12 Winter Season), Tech Note of NIED., 372, 31pp, 2012.
- Neff, W., Compo, G. P., Ralph, F. M., and Shupe, M. D.: Continental heat anomalies and the extreme melting of the Greenland ice surface in 2012 and 1889, *J. Geophys. Res.-Atmos.*, **119**, 6520–6536, doi:10.1002/2014JD021470, 2014.
- Neshyba, S. P., Grenfell, T. C., and Warren, S. G.: Representation of a nonspherical ice particle by a collection of independent spheres for scattering and absorption of radiation: 2. Hexagonal columns and plates, *J. Geophys. Res.*, **108(D15)**, 4448, doi:10.1029/2002JD003302, 2003.
- Nghiem, S. V., Hall, D. K., Mote, T. L., Tedesco, M., Albert, M. R., Keegan, K., Shuman, C. A., DiGirolamo, N. E., and Neumann, G.: The extreme melt across the Greenland ice sheet in 2012, *Geophys. Res. Lett.*, **39**, L20502, doi:10.1029/2012GL053611, 2012.
- Nishimura, K., Baba, E., Hirashima, H., and Lehning, M.: Application of the snow cover model SNOWPACK to snow avalanche warning in Niseko, Japan, *Cold. Reg. Sci. Technol.*, **43**, 62–70, doi:10.1016/j.coldregions.2005.05.007, 2005.
- Niwano, M., Aoki, T., Kuchiki, K., Hosaka, M., and Kodama, Y.: Snow Metamorphism and Albedo Process (SMAP) model for climate studies: Model validation using meteorological and snow impurity data measured at Sapporo, Japan, *J. Geophys. Res.*, **117**, F03008, doi:10.1029/2011JF002239, 2012.
- Niwano, M., Aoki, T., Kuchiki, K., Hosaka, M., Kodama, Y., Yamaguchi, S., Motoyoshi, H., and Iwata, Y.: Evaluation of updated physical snowpack model SMAP, *Bull. Glaciol. Res.*, **32**, 65–78,

- doi:10.5331/bgr.32.65, 2014.
- Ohmura, A. and Reeh, N.: New precipitation and accumulation maps for Greenland, *J. Glaciol.*, **37**, 140–148, 1991.
- Ohmura, A., Konzelmann, T., Rotach, M., Forrer, J., Wild, M., Abe-Ouchi, A., and Toritani, H.: Energy balance for the Greenland ice sheet by observation and model computation, in: *Snow and Ice Covers; Interaction With the Atmosphere and Ecosystems*, edited by: Jones, H. G., Davies, T. D., Ohmura, A., and Morris, E. M., IAHS, Gentbrugge, Belgium, 85–94, 1994.
- Ohmura, A.: Observed decadal variations in surface solar radiation and their causes, *J. Geophys. Res.*, **114**, D00D05, doi:10.1029/2008JD011290, 2009.
- Painter, T. H., Barrett, A. P., Landry, C. C., Neff, J. C., Cassidy, M. P., Lawrence, C. R., McBride, K. E., and Farmer, G. L.: Impact of disturbed desert soils on duration of mountain snow cover, *Geophys. Res. Lett.*, **34**, L12502, doi:10.1029/2007GL030284, 2007.
- Paulson, C. A.: The mathematical representation of wind speed and temperature profiles in the unstable atmospheric surface layer, *J. Appl. Meteorol.*, **9**, 857–861, doi:10.1175/1520-0450(1970)009<0857:TMROWS>2.0.CO;2, 1970.
- Pedersen, C. A., and Winther, J.-G.: Intercomparison and validation of snow albedo parameterization schemes in climate models, *Clim. Dyn.*, **25**, 351–362, doi:10.1007/s00382-005-0037-0, 2005.
- Peters-Lidard, C. D., Blackburn, E., Liang, X. and Wood, E. F.: The Effect of Soil Thermal Conductivity Parameterization on Surface Energy Fluxes and Temperatures, *J. Atmos. Sci.*, **55**, 1209–1224, doi:10.1175/1520-0469(1998)055<1209:TEOSTC>2.0.CO;2, 1998.
- Phillips, T., Rajaram, H., and Steffen, K.: Cryo-hydrologic warming: A potential mechanism for rapid thermal response of ice sheets, *Geophys. Res. Lett.*, **37**, L20503, doi:10.1029/2010GL044397, 2010.
- Pinzer, B. R. and Schneebeli, M.: Snow metamorphism under alternating temperature gradients:

- Morphology and recrystallization in surface snow, *Geophys. Res. Lett.*, **36**, L23503, doi:10.1029/2009GL039618, 2009.
- Pollack, J. B., and Cuzzi, J. N.: Scattering by nonspherical particles of size comparable to a wavelength: A new semi-empirical theory and its application to tropospheric aerosols, *J. Atmos. Sci.*, **37**, 868–881, doi:10.1175/1520-0469(1980)037<0868:SBNPOS>2.0.CO;2, 1980.
- Qu, X., and Hall, A.: What controls the strength of snow-albedo feedback?, *J. Clim.*, **20**, 3971–3981, doi:10.1175/JCLI4186.1, 2007.
- Rasmus, S., Räisänen, J. and Lehning, M.: Estimating snow conditions in Finland in the late 21st century using the SNOWPACK model with regional climate scenario data as input, *Ann. Glaciol.*, **38**, 238–244, doi:10.3189/172756404781814843, 2004.
- Richards, L. A.: Capillary conduction of liquids through porous mediums. *J. Appl. Phys.*, **1**, 318–333, doi:10.1063/1.1745010, 1931.
- Rousselot, M., Durand, Y., Giraud, G., Merindol, L. and Daniel, L.: Analysis and forecast of extreme new-snow avalanches: a numerical study of the avalanche cycles of February 1999 in France, *J. Glaciol.*, **56**, 758–770, doi:10.3189/002214310794457308, 2010.
- Saito, K., Yamaguchi, S., Iwata, H., Harazono, Y., Kosugi, K., Lehning, M. and Shulski, M.: Climatic physical snowpack properties for large-scale modeling examined by observations and a physical model, *Polar Science*, **6**, 79–95, doi:10.1016/j.polar.2012.02.003, 2012.
- Schneebeli, M., and Sokratov, S. A.: Tomography of temperature gradient metamorphism of snow and associated changes in heat conductivity, *Hydrol. Processes*, **18**, 3655–3665, doi:10.1002/hyp.5800, 2004.
- Screen, J., and Simmonds, I.: The central role of diminishing sea ice in recent Arctic temperature amplification, *Nature*, **464**, 1334–1337, doi:10.1038/nature09051, 2010.
- Sellers, W. D.: A global climatic model based on the energy balance of the earth-atmosphere system,

- J. Appl. Meteorol.*, **8**, 392–400, doi:10.1175/1520-0450(1969)008<0392:AGCMBO>2.0.CO;2, 1969.
- Serreze, M. C., and Francis, J. A.: The arctic amplification debate, *Clim. Change*, **76**, 241 – 264, doi: 10.1007/s10584-005-9017-y, 2006.
- Shimizu, H.: Air permeability of deposited snow, Contributions from the Institute of Low Temperature Science, A22, 1–32, 1970.
- Smeets, C. J. P. P. and van den Broeke, M. R.: Temporal and spatial variations of the aerodynamic roughness length in the ablation zone of the Greenland ice sheet, *Bound.-Lay. Meteorol.*, **128**, 315–338, doi:10.1007/s10546-008-9291-0, 2008.
- Steffen, K., and Box, J.: Surface climatology of the Greenland Ice Sheet: Greenland Climate Network 1995–1999, *J. Geophys. Res.*, **106(D24)**, 33951–33964, doi:10.1029/2001JD900161, 2001.
- Sturm, M., Holmgren, J., König, M., and Morris, K.: The thermal conductivity of seasonal snow, *J. Glaciol.*, **43**, 26–41, 1997.
- Taillandier, A.-S., Domine, F., Simpson, W. R., Sturm, M., and Douglas, T. A.: Rate of decrease of the specific surface area of dry snow: Isothermal and temperature gradient conditions, *J. Geophys. Res.*, **112**, F03003, doi:10.1029/2006JF000514, 2007.
- Takeuchi, Y., Endo, Y., and Murakami, S.: High correlation between winter precipitation and air temperature in heavy snowfall areas in Japan, *Ann. Glaciol.*, **49**, 7–10, doi:10.3189/172756408787814898, 2008.
- Tanikawa, T., Li, W., Kuchiki, K., Aoki, T., Hori, M., and Stamnes, K.: Retrieval of snow physical parameters by neural networks and optimal estimation: case study for ground-based spectral radiometer system, *Optics Express*, **23**, A1442–A1462, doi:10.1364/OE.23.0A.1442, 2015.
- Tedesco, M., Brodzik, M., Armstrong, R., Savoie, M., and Ramage, J.: Pan arctic terrestrial snowmelt trends (1979–2008) from spaceborne passive microwave data and correlation with the Arctic

- Oscillation, *Geophys. Res. Lett.*, **36**, L21402, doi:10.1029/2009GL039672, 2009.
- Tedesco, M., Fettweis, X., Mote, T., Wahr, J., Alexander, P., Box, J. E., and Wouters, B.: Evidence and analysis of 2012 Greenland records from spaceborne observations, a regional climate model and reanalysis data, *The Cryosphere*, **7**, 615–630, doi:10.5194/tc-7-615-2013, 2013.
- The Japanese Society of Snow and Ice: Glaciological observation guidebook, Asakura Publishing, Tokyo, Japan, 2010.
- U.S. Army Corps of Engineers: Snow Hydrology; Summary Report of the Snow Investigations, North Pac. Div., Portland, Oreg, USA, 1956.
- van As, D.: Warming, glacier melt and surface energy budget from weather station observations in the Melville Bay region of northwest Greenland, *J. Glaciol.*, **57**, 208–220, doi:10.3189/002214311796405898, 2011.
- van Dam, J. C. and Feddes, R. A.: Numerical simulation of infiltration, evaporation and shallow groundwater levels with the Richards equation, *J. Hydrol.*, **233**, 72–85, doi:10.1016/S0022-1694(00)00227-4, 2000.
- van den Broeke, M., van As, D., Reijmer, C., and van de Wal, R.: Assessing and Improving the Quality of Unattended Radiation Observations in Antarctica, *J. Atmos. Oceanic Technol.*, **21**, 1417–1431, doi:10.1175/1520-0426(2004)021<1417:AAITQO>2.0.CO;2, 2004a.
- van den Broeke, M., Reijmer, C., and van de Wal, R.: Surface radiation balance in Antarctica as measured with automatic weather stations, *J. Geophys. Res.*, **109**, D09103, doi:10.1029/2003JD004394, 2004b.
- van den Broeke, M., Reijmer, C., van As, D., van de Wal, R., and Oerlemans, J.: Seasonal cycles of Antarctic surface energy balance from automatic weather stations, *Ann. Glaciol.*, **41**, 131–139, 2005.
- van den Broeke, M., Reijmer, C., van As, D., and Boot, W.: Daily cycle of the surface energy balance

- in Antarctica and the influence of clouds, *Int. J. Climatol.*, **26**, 1587–1605, doi:10.1002/joc.1323, 2006.
- van den Broeke, M. R., Smeets, C. J. P. P., and van de Wal, R. S. W.: The seasonal cycle and interannual variability of surface energy balance and melt in the ablation zone of the west Greenland ice sheet, *The Cryosphere*, **5**, 377–390, doi:10.5194/tc-5-377-2011, 2011.
- van Genuchten, M. T.: A closed-form equation for predicting the hydraulic conductivity of unsaturated soil, *Soil Sci. Soc. Am. J.*, **44**, 892–898, 1980.
- Van Tricht, K. Lhermitte, S., Lenaerts, J. T. M., Gorodetskaya, I.V., L'Ecuyer, T. S., Noël, B., van den Broeke, M. R., Turner, D. D., and van Lipzig, N. P. M.: Clouds enhance Greenland ice sheet meltwater runoff, *Nat. Commun.*, **7**, 10266 doi:10.1038/ncomms10266, 2016.
- Vaughan, D. G., Comiso, J. C., Allison, I., Carrasco, J., Kaser, G., Kwok, R., Mote, P., Murray, T., Paul, F., Ren, J., Rignot, E., Solomina, O., Steffen K., and Zhang, T.: Observations: Cryosphere, in: *Climate Change 2013: The Physical Science Basis. Contribution of Working Group I to the Fifth Assessment Report of the Intergovernmental Panel on Climate Change* (Stocker, T. F., Qin, D., Plattner, G.-K., Tignor, M., Allen, S. K., Boschung, J., Nauels, A., Xia, Y., Bex, V., and Midgley, P. M. (eds.)), Cambridge Univ. Press, Cambridge, UK, and New York, USA, 2013.
- Vionnet, V., Brun, E., Morin, S., Boone, A., Faroux, S., Le Moigne, P., Martin, E., and Willemet, J.-M.: The detailed snowpack scheme Crocus and its implementation in SURFEX v7.2, *Geosci. Model Dev.*, **5**, 773-791, doi:10.5194/gmd-5-773-2012, 2012.
- Wagon, P., Lafaysse, M., Lejeune, Y., Maisincho, L., Rojas, M. and Chazarin, J. P.: Understanding and modeling the physical processes that govern the melting of snow cover in a tropical mountain environment in Ecuador, *J. Geophys. Res.*, **114**, D19113, doi:10.1029/2009JD012292, 2009.
- Warren, S. G. and Wiscombe, W. J.: A model for the spectral albedo of snow. II: Snow containing

- atmospheric aerosols. *J. Atmos. Sci.*, **37**, 2734–2745, doi:10.1175/1520-0469(1980)037<2734:AMFTSA>2.0.CO;2, 1980.
- Webb, E. K.: Profile relationships: The log-linear range, and extension to strong stability, *Q. J. R. Meteorol. Soc.*, **96**, 67–90, doi:10.1002/qj.49709640708, 1970.
- Wever, N., Fierz, C., Mitterer, C., Hirashima, H., and Lehning, M.: Solving Richards Equation for snow improves snowpack meltwater runoff estimations in detailed multi-layer snowpack model, *The Cryosphere*, **8**, 257–274, doi:10.5194/tc-8-257-2014, 2014.
- Wever, N., Schmid, L., Heilig, A., Eisen, O., Fierz, C., and Lehning, M.: Verification of the multi-layer SNOWPACK model with different water transport schemes, *The Cryosphere*, **9**, 2271–2293, doi:10.5194/tc-9-2271-2015, 2015.
- Wiscombe, W. J. and Warren, S. G.: A model for the spectral albedo of snow. I: Pure snow, *J. Atmos. Sci.*, **37**, 2712–2733, doi:10.1175/1520-0469(1980)037<2712:AMFTSA>2.0.CO;2, 1980.
- Yamaguchi, S., Sato, A. and Lehning, M.: Application of the numerical snowpack model (SNOWPACK) to the wet-snow region in Japan, *Ann. Glaciol.*, **38**, 266–272, doi:10.3189/172756404781815239, 2004.
- Yamaguchi, S., Nakai, S., Iwamoto, K., and Sato, A.: Influence of anomalous warmer winter on statistics of measured winter precipitation data, *J. Appl. Meteor. Climatol.*, **48**, 2403–2409, doi:10.1175/2009JAMC2008.1, 2009.
- Yamaguchi, S., Katsushima, T., Sato, A. and Kumakura, T.: Water retention curve of snow with different grain sizes, *Cold. Reg. Sci. Technol.*, **64**, 87–93, doi:10.1016/j.coldregions.2010.05.008, 2010.
- Yamaguchi, S., Watanabe, K., Katsushima, T., Sato, A. and Kumakura, T.: Dependence of the water retention curve of snow on snow characteristics, *Ann. Glaciol.*, **53**, 6–12, doi:10.3189/2012AoG61A001, 2012.

- Yamaguchi, S., Matoba, S., Yamazaki, T., Tsushima, A., Niwano, M., Tanikawa, T., and Aoki, T.: Glaciological observations in 2012 and 2013 at SIGMA-A site, Northwest Greenland, *Bull. Glaciol. Res.*, **32**, 95–105, doi:10.5331/bgr.32.95, 2014.
- Yamanouchi, T.: Variations of incident solar flux and snow albedo on the solar zenith angle and cloud cover, at Mizuho station, Antarctica, *J. Meteorol. Soc. Jpn.*, **61**, 879–893, 1983.
- Yamazaki, T.: A multi-layer heat balance model of snow cover adaptable to intensely cold regions (in Japanese with English abstract), *Seppyo*, **60**, 131–141, 1998.
- Yamazaki, T.: A one-dimensional land surface model adaptable to intensely cold regions and its applications in eastern Siberia, *J. Meteorol. Soc. Jpn.*, **79**, 1107–1118, doi:10.2151/jmsj.79.1107, 2001.
- Yasunari, T. J., Koster, R. D., Lau, K.-M., Aoki, T., Sud, Y. C., Yamazaki, T., Motoyoshi, H., and Kodama, Y.: Influence of dust and black carbon on the snow albedo in the NASA Goddard Earth Observing System version 5 land surface model, *J. Geophys. Res.*, **116**, D02210, doi:10.1029/2010JD014861, 2011.
- Yasunari, T. J., Lau, K.-M., Mahanama, S. P. P., Colarco, P. R., da Silva, A. M., Aoki, T., Aoki, K., Murao, N., Yamagata, S., Kodama, Y.: The GODdard SnoW Impurity Module (GOSWIM) for the NASA GEOS-5 Earth System Model: Preliminary comparisons with observations in Sapporo, Japan, *SOLA*, **10**, 50-56, doi:10.2151/sola.2014-011, 2014.
- Yokoyama, K., Ohno, H., Kominami, Y., Inoue, S., and Kawakata, T.: Performance of Japanese precipitation gauges in winter, *Seppyo*, **65**, 303–316, (in Japanese with English summary), 2003.
- Yukimoto, S., Yoshimura, H., Hosaka, M., Sakami, T., Tsujino, H., Hirabara, M., Tanaka, T. Y., Deushi, M., Obata, A., Nakano, H., Adachi, Y., Shindo, E., Yabu, S., Ose, T., and Kitoh, A.: Meteorological Research Institute Earth System Model Version 1 (MRIESM1) – Model Description, Tech. Rep. of MRI 64, 83 pp., available at: <http://www.mri->



[jma.go.jp/Publish/Technical/index\\_en.html](http://jma.go.jp/Publish/Technical/index_en.html) (last access: 15 April 2015), 2011.

Zhang, T.: Influence of the seasonal snow cover on the ground thermal regime: An overview, *Rev. Geophys.*, **43**, RG4002, doi:10.1029/2004RG000157, 2005.

## Curriculum Vitae

Name: Masashi Niwano

Date of birth: 30 April, 1980

2000–2004: Meteorological College (B.Sc.)

2004–2006: Observer at Toyama Local Meteorological Observatory, Japan Meteorological Agency

2006–2008: Government official at Tokyo District Meteorological Observatory, Japan Meteorological Agency

2008– : Climate scientist at Meteorological Research Institute, Japan Meteorological Agency

## Publications

16. Miyazaki, S., Saito, K., Mori, J., Yamazaki, T., Ise, T., Arakida, H., Hajima, T., Iijima, Y., Machiya, H., Sueyoshi, T., Yabuki, H., Burke, E. J., Hosaka, M., Ichii, K., Ikawa, H., Ito, A., Kotani, A., Matsuura, Y., Niwano, M., Nitta, T., O'ishi, R., Ohta, T., Park, H., Sasai, T., Sato, A., Sato, H., Sugimoto, A., Suzuki, R., Tanaka, K., Yamaguchi, S., and Yoshimura, K.: The GRENE-TEA model intercomparison project (GTMIP): overview and experiment protocol for Stage 1, *Geosci. Model Dev.*, **8**, 2841–2856, doi:10.5194/gmd-8-2841-2015, 2015.
15. Niwano, M., Aoki, T., Matoba, S., Yamaguchi, S., Tanikawa, T., Kuchiki, K., and Motoyama, H.: Numerical simulation of extreme snowmelt observed at the SIGMA-A site, northwest Greenland, during summer 2012, *The Cryosphere*, **9**, 971–988, doi:10.5194/tc-9-971-2015, 2015.
14. Kuchiki, K., Aoki, T., Niwano, M., Matoba, S., Kodama, Y., and Adachi, K.: Elemental carbon, organic carbon, and dust concentrations in snow measured with thermal optical method and filter weighing: variations during 2007–2013 winters in Sapporo, Japan. *J. Geophys. Res. Atmos.*, **120**, 868–882, doi:10.1002/2014JD022144, 2015.

13. Tanikawa, T., Hori, M., Aoki, T., Hachikubo, A., Kuchiki, K., Niwano, M., Matoba, S., Yamaguchi, S., and Stamnes, K.: In-situ measurement of polarization properties of snow surface under the Brewster geometry in Hokkaido, Japan and northwest Greenland ice sheet. *J. Geophys. Res. Atmos.*, **119**, 13946–13964, doi:10.1002/2014JD022325, 2014.
12. Aoki, T., Matoba, S., Yamaguchi, S., Tanikawa, T., Niwano, M., Kuchiki, K., Adachi, K., Uetake, J., Motoyama, H., and Hori, M.: Light-absorbing snow impurity concentrations measured on Northwest Greenland ice sheet in 2011 and 2012. *Bull. Glaciol. Res.*, **32**, 21-31, doi:10.5331/bgr.32.21, 2014.
11. Hori, M., Aoki, T., Tanikawa, T., Kuchiki, K., Niwano, M., Yamaguchi, S., and Matoba, S.: Dependence of thermal infrared emissive behaviors of snow cover on the surface snow type. *Bull. Glaciol. Res.*, **32**, 33-45, doi:10.5331/bgr.32.33, 2014.
10. Hachikubo, A., Yamaguchi, S., Arakawa, H., Tanikawa, T., Hori, M., Sugiura, K., Matoba, S., Niwano, M., Kuchiki, K., and Aoki, T.: Effects of temperature and grain type on time variation of snow specific surface area. *Bull. Glaciol. Res.*, **32**, 47-53, doi:10.5331/bgr.32.47, 2014.
09. Yamaguchi, S., Motoyoshi, H., Tanikawa, T., Aoki, T., Niwano, M., Takeuchi, Y., and Endo, Y.: Application of snow specific surface area measurement using an optical method based on near-infrared reflectance around 900-nm wavelength to wet snow zones in Japan. *Bull. Glaciol. Res.*, **32**, 55-64, doi:10.5331/bgr.32.55, 2014.
08. Niwano, M., Aoki, T., Kuchiki, K., Hosaka, M., Kodama, Y., Yamaguchi, S., Motoyoshi, H., and Iwata, H.: Evaluation of updated physical snowpack model SMAP. *Bull. Glaciol. Res.*, **32**, 65-78, doi:10.5331/bgr.32.65, 2014.
07. Yamaguchi, S., Matoba, S., Yamazaki, T., Tsushima, A., Niwano, M., Tanikawa, T., and Aoki, T.: Glaciological observations in 2012 and 2013 at SIGMA-A site, Northwest Greenland, *Bull. Glaciol. Res.*, **32**, 95-105, doi:10.5331/bgr.32.95, 2014.

06. Hori, M., Tanikawa, T., Aoki, T., Hachikubo, A., Sugiura, K., Kuchiki, K., and Niwano, M.: Possibility to Discriminate Snow Types Using Brightness Temperatures in the Thermal Infrared Wavelength Region, *RADIATION PROCESSES IN THE ATMOSPHERE AND OCEAN (IRS2012)*, Robert Cahalan and Jurgen Fischer (Eds), AIP Conf. Proc., **1531**, 316, doi: 10.1063/1.4804770, 2013.
05. Aoki, T., Kuchiki, K., Niwano, M., Matoba, S., Uetake, J., Masuda, K., and Ishimoto, H.: Numerical Simulation of Spectral Albedos of Glacier Surfaces Covered with Glacial Microbes in Northwestern Greenland, *RADIATION PROCESSES IN THE ATMOSPHERE AND OCEAN (IRS2012)*, Robert Cahalan and Jurgen Fischer (Eds), AIP Conf. Proc., **1531**, 176, doi: 10.1063/1.4804735, 2013.
04. Hori, M., Aoki, T., Tanikawa, T., Hachikubo, A., Sugiura, K., Kuchiki, K., and Niwano, M.: Modeling angular dependent spectral emissivity of snow and ice in the thermal infrared atmospheric window, *Appl. Opt.*, **52**, 7243-7255, doi:10.1364/AO.52.007243, 2013.
03. Niwano, M., Aoki, T., Kuchiki, K., Hosaka, M., and Kodama, Y.: Snow Metamorphism and Albedo Process (SMAP) model for climate studies: Model validation using meteorological and snow impurity data measured at Sapporo, Japan, *J. Geophys. Res.*, **117**, F03008, doi:10.1029/2011JF002239, 2012.
02. Kuchiki, K., Aoki, T., Niwano, M., Motoyoshi, H., and Iwabuchi, H.: Effect of sastrugi on snow bidirectional reflectance and its application to MODIS data, *J. Geophys. Res.*, **116**, D18110, doi:10.1029/2011JD016070, 2011.
01. Aoki, T., Kuchiki, K., Niwano, M., Kodama, Y., Hosaka, M., and Tanaka, T.: Physically based snow albedo model for calculating broadband albedos and the solar heating profile in snowpack for general circulation models, *J. Geophys. Res.*, **116**, D11114, doi:10.1029/2010JD015507, 2011.